DISSERTATION

Acceleration of Magnetic Resonance Spectroscopic Imaging Sequences via Parallel Imaging and Spatio-Spectral Encoding

Ausgeführt zum Zwecke der Erlangung des akademischen Grades eines Doktors der technischen Wissenschaften unter der Leitung von

Em. Univ.-Prof. Dr.techn. Dipl.-Ing. Gerald Badurek

Atominstitut

TU Wien

und

Assoc.-Prof. Priv.-Doz. Dr.techn. Dipl.-Ing. Wolfgang Bogner

Radiologie und Nuklearmedizin

Medizinische Universität Wien

Eingereicht an der Technischen Universität Wien

Fakultät für Physik

von

Mag. rer. nat. Bernhard Strasser

Matrikelnummer: 0601711

Schulgasse 12/10, 1180 Wien

Wien, am 13.02.2017

Deutsche Kurzfassung

Wie von Bogner et al. gezeigt wurde, bietet das Messen des “free induction decays” (FID) statt eines Echos, gemeinsam mit der hohen Feldstärke von 7T, genug Signal zu Rauschverhältnis (SNR), um hohe Auflösungen von $3.4 \times 3.4\,\mathrm{mm}^2$ in der Magnetresonanzspektroskopie (MRSI) zu ermöglichen. Gleichzeitig ist die Punktverteilungsfunktion gut genug lokalisiert, um das Verschmieren von extrakranialem Lipidsignal über das Gehirnbild zu verhindern. Mit kleineren Auflösungen wäre das nicht gegeben, da es wegen dem Messen des FIDs nicht möglich ist, das Signal durch Methoden wie “point resolved spectroscopy” räumlich einzuschränken, und weil die kurzen Echozeiten stärkere Lipidsignale verursachen. Leider ist die Messzeit bei solch hohen Auflösungen 30 Minuten pro Schicht. Daher war das erste Ziel meiner Arbeit eine Spulenkombinationsmethode für MRSI Daten zu entwickeln, um das SNR noch weiter zu erhöhen, welches dann für eine Verkürzung der Messdauer benutzt werden kann. Eine Spulenkombinationsmethode, “MUSICAL”, wurde entwickelt, welche konventionelle MR-Bilddaten als Kombinationsgewichte benutzt. Im Vergleich zu zwei Standardmethoden benötigt MUSICAL einerseits keine zusätzliche Referenzspule, und erhöht andererseits das SNR um 30 %. Um die MRSI-Akquisition zu beschleunigen, wurden zwei konzeptionell verschiedene Methoden getestet: Parallelbildgebung (PI), und Raum-Zeit-Kodierung (SSE). Eine neue PI Methode, (2+1)D-CAIPIRINHA, wurde entwickelt, welche in alle drei Raumrichtungen beschleunigt. Die Ergebnisse waren besser im Vergleich zu zwei Standard-Methoden, 2D-GRAPPA, und 2D-CAIPIRINHA. SSE bietet höhere Beschleunigungsfaktoren als PI, und kann deshalb sogar für 3D-MRSI benutzt werden. SSE wurde in Form von konzentrischen Kreisen in eine MRSI Sequenz implementiert. Eine Rekonstruktionspipeline wurde in BASH und MATLAB programmiert, um die MRSI Daten all dieser Methoden rekonstruieren zu können. Die Pipeline ist open-source und vollautomatisch, sodass der Benutzer keinerlei Eingaben nach dem Starten des Programms tätigen muss. Letztlich wurden die entwickelten Methoden dafür verwendet, Multiple Sklerose Patienten in einer klinischen Studie zu messen. Metabolische Änderungen waren in den Läsionen im Vergleich zu normal aussehender weißer Hirnsubstanz erkennbar, in Übereinstimmung zur Literatur, allerdings viel detailreicher.

Abstract

As was shown by Bogner et al., measuring the free induction decay (FID) instead of an echo, together with the high field strength of 7T provides enough signal to noise ratio (SNR) for measuring magnetic resonance spectroscopic imaging (MRSI) at high resolutions of $3.4 \times 3.4\,\mathrm{mm}^2$. At the same time, the point spread function (PSF) is localized well enough to prevent extra-cranial lipid signals from spreading over the brain image. With lower resolutions, these lipids would be problematic, as measuring the FID prevents the possibility to spatially restrict the signal via methods like point resolved spectroscopy, and because the short echo times result in stronger lipid signals. Unfortunately, such high resolutions also require long measurement times of about 30 minutes for one slice. Thus, the first aim of my work was to implement a robust coil combination for MRSI data from array coils to further increase the SNR. This increased SNR can then be used to accelerate the measurement. A coil combination method termed "MUSICAL" was developed, which uses magnetic resonance imaging data as coil combination weights. MUSICAL does not need an additional reference coil, and the SNR was increased by 30 % in comparison to two state of the art coil combination methods. To accelerate the MRSI acquisition, two conceptually different approaches were tested: Parallel imaging (PI), and spatio-spectral encoding (SSE). A new PI method, (2+1)D-CAIPIRINHA, for accelerating in all three spatial dimensions was developed. This method yielded improved results in comparison to two standard PI methods, 2D-GRAPPA, and 2D-CAIPIRINHA. SSE offers potentially higher acceleration factors than PI, and can therefore be used to even measure 3D-MRSI. SSE was implemented into an MRSI sequence by measuring concentric circle trajectories. In order to reconstruct the MRSI data with all these methods, a reconstruction pipeline was programmed in BASH and MATLAB. This pipeline is open source and fully automatic, and does therefore not need any additional user input during runtime. Finally, the methods developed in the course of this thesis were applied by measuring multiple sclerosis patients in a clinical study. Metabolic changes were observed in the lesions in comparison to normal appearing white matter, mostly in accordance with literature, but with much higher spatial detail.

Table of Contents

List of Abbreviations

AC	Array Coil.
ACS	Auto-Calibration Signal.
AP	Artifact Power.
BASH	Bourne Again Shell.
BET2	Brain Extraction Tool v2.
CAIPIRINHA	Controlled Aliasing In Parallel Imaging Results In Higher Acceleration.
Cho	Choline.
CONCEPT	Concentrically Circular Echo-Planar Trajectories.
Cr	Creatine.
CRLB	Cramér-Rao lower bound.
DICOM	Digital Imaging and Communications in Medicine.
EPI	Echo Planar Imaging.
EPSI	Echo Planar Spectroscopic Imaging.
FAST	FMRIB's Automated Segmentation Tool.
FID	Free Induction Decay.
FLAIR	Fluid-Attenuated Inversion Recovery.
FLASH	Fast Low Angle Shot.
FoV	Field of View.
FSL	FMRIB Software Library.

GABA	*Gamma*-Aminobutyric Acid.
Glu	Glutamate.
Glx	Glutamine and Glutamate.
GM	Gradient Moment.
GRAPPA	Generalized Autocalibrating Partially Parallel Acquisitions.
GRE	Gradient Echo.
GSH	Glutathione.
GUI	Graphical User Interface.
ICE	Image Calculation Environment.
Ins	*Myo*-Inositol.
ISMRM	International Society for Magnetic Resonance in Medicine.
MATLAB	Matrix Laboratory.
MIDAS	Metabolite Imaging and Data Analysis System.
MINC	Medical Image NetCDF.
MP2RAGE	Magnetization-Prepared Two Rapid Acquisition Gradient Echoes.
MPRAGE	Magnetization-Prepared Rapid Gradient-Echo.
MR	Magnetic Resonance.
MRI	Magnetic Resonance Imaging.
MRS	Magnetic Resonance Spectroscopy.
MRSI	Magnetic Resonance Spectroscopic Imaging.
MS	Multiple Sclerosis.
MUSICAL	Multichannel Spectroscopic Data Combined by Matching Image Calibration Data.
NAA	N-Acetyl Aspartate.
NAWM	Normal Appearing White Matter.
PI	Parallel Imaging.

PINS	Power Independent of Number of Slices.
PREP	Projection Reconstruction Echo-Planar.
PRESS	Point-Resolved Spectroscopy.
PSF	Point Spread Function.
RF	Radio Frequency.
RMSE	Root Mean Square Error.
RoI	Region of Interest.
SENSE	Sensitivity Encoding.
SNR	Signal to Noise Ratio.
SNR/t	SNR per Unit Time.
SSE	Spatio-Spectral Encoding.
SSH	Secure Shell.
STEAM	Stimulated Echo Acquisition Mode.
TARQUIN	Totally Automatic Robust Quantitation in NMR.
tCho	total Choline.
tCr	total Creatine.
TE	Echo Time.
tNAA	total N-Acetyl Aspartate.
TR	Repetition Time.
VC	Volume Coil.
VD	Variable Density.
VoI	Volume of Interest.
WET	Water Suppression Enhanced Through T1-Effects.
WM	White Matter.

Acknowledgements

I want to thank my supervisors Gerald Badurek and Wolfgang Bogner for making the work behind this thesis possible, financing me (again and again...), and the help with their immense MR knowledge; my boss Siegfried Trattnig; and my colleagues Lukas Hingerl, Michal Považan, Gilbert Hangel, Eva Hečková, Philipp Moser, Benedikt Hager, Martin Gajdošík, Pedro Cardoso, Olgica Zarić, Marjeta Tušek Jelenc, Barbara Dymerska, and all other colleagues from the MRCE (or however it is called currently).

I also want to thank my parents and my sister, Helga, Roman and Ursula; my grandparents; my aunts and uncles; and cousins. Thank you all for your steady support.
My gratitude also to all my friends, Pia and Clemens, Samuel and Christina, Benedikt, Lukas, David, Günter, Marius, Marcus, and many more! Thank you for all the distraction.

With all my heart I want to thank my girlfriend Simona Karolus for all her love and support; for not being my future girlfriend anymore; and especially for her resolution to read this entire thesis. I hope you fall asleep easily, at least.

Finally, I want to acknowledge all people who want to be acknowledged; and those who don't. May the acknowledgment be with you!

And now, prepare for a heavy reading. If you want justice, you've come to the wrong place.

1 Introduction

The following chapter should provide a basic overview about the thesis and the theory necessary to understand it. The theory is, however, by far not exhaustive, as only those concepts relevant for this thesis are described. For a more extensive theoretical treatment, I suggest the excellent books "Magnetic Resonance Imaging: Physical Principles and Sequence Design" by Brown et al. (1), and "In Vivo NMR Spectroscopy" by de Graaf (2).

1.1 Outline of the Thesis

This thesis is subdivided in six main chapters. In the first chapter, some theoretical background to understand the remaining thesis is provided. In the second, different coil combination methods for combining Magnetic Resonance Spectroscopic Imaging (MRSI) data of different channels of an Array Coil (AC) are compared, including Multichannel Spectroscopic Data Combined by Matching Image Calibration Data (MUSICAL), as proposed by our group (3). Together with the ultra-high field strength, and the very short acquisition delay, the usage of an AC and an optimal coil combination can provide a very high Signal to Noise Ratio (SNR), even for high-resolution MRSI data. However, the measurement times of such high-resolution MRSI sequences are too long for being clinically feasible. Chapter 3 deals with one possibility to accelerate such high resolution MRSI sequences from e.g. 30 min to 6 min using Parallel Imaging (PI). Another acceleration method, Spatio-Spectral Encoding (SSE), is presented in chapter 4. In order to perform all the sophisticated reconstructions necessary for these methods, and to present the data in a user-friendly way, a reconstruction pipeline was programmed in Bourne Again Shell (BASH) and Matrix Laboratory (MATLAB). This pipeline is described in chapter 5. Finally, the thesis is concluded by chapter 6, in which an application of the developed methods is presented. Multiple Sclerosis (MS) patients were measured with an PI-accelerated sequence, and the resulting data were reconstructed as described in chapter 2 and 5. Several interesting findings were made based on the acquired data.

All work described in this thesis was done by me, except if explicitly stated otherwise. Two parts were done in close collaboration with two colleagues: The implementation of the Gradient Echo (GRE) pre-scan into our Cartesian MRSI sequence was done together with Gilbert Hangel, and the Concentrically Circular Echo-Planar Trajectories (CONCEPT) sequence together with Lukas Hingerl. For the latter, the reconstruction was completely done by him, while most parts of the sequence were written by me. Concerning the GRE pre-scan, the work was divided approximately equally.

1.2 MR Basics

If exposed to a static magnetic field $\vec{B}_0$, nuclei act like magnetic dipoles that spin around the direction of $\vec{B}_0$ with the Larmor frequency

$$\omega_0 = \gamma B_0 \tag{1.1}$$

where γ is the gyro-magnetic ratio, and $B_0 \cdot \vec{e}_z := \vec{B}_0$, by which the z-axis is defined parallel to the main magnetic field $\vec{B}_0$. The individual dipoles have a higher probability to align along the external magnetic field $\vec{B}_0$, an effect that scales with the strength of B_0. This causes a non-zero net magnetization of the tissue.
If an additional time-depending magnetic field in the Radio Frequency (RF) range, B_1, is applied to the tissue, the tissue magnetization is flipped towards the x-y-plane (orthogonal to $\vec{B}_0$), if the frequency of B_1 is ω_0. In this case, B_1 is said to be "on-resonant". After the additional field is turned off again, the magnetization of the tissue precesses around $\vec{B}_0$, again with the frequency ω_0. During this precession, the magnetization relaxes back to its equilibrium state, which is parallel to $\vec{B}_0$. Two mechanisms cause the relaxation: The spin-lattice relaxation, an interaction between the spins and their surroundings, and the spin-spin relaxation describing the coherence loss between the spins. The time constants T_1 and T_2 are used to describe how fast these processes happen. Different materials and tissues have different relaxation constants, by virtue of which the main contrast in Magnetic Resonance Imaging (MRI) is generated. This whole process, precession and relaxation, causes a time-depending magnetic field itself, which can be detected by a coil close to the tissue.

1.3 MR Spectroscopy

The basis of Magnetic Resonance (MR) spectroscopy is the fact that protons have different resonance frequencies ω_0 depending on their chemical environment. Thus, the

protons of different molecules and the different protons within one molecule can have different resonance frequencies, and can therefore be differentiated.
We can measure a Free Induction Decay (FID) by acquiring the signal repetitively at different time points. By performing a Fourier transform, we analyze which frequencies the FID contains. This results in a spectrum, where we get one single peak for each chemical compound (e.g. metabolite or part of metabolite). The peak heights correlate with the abundance of the chemical compound. These two facts together enable Magnetic Resonance Spectroscopy (MRS) to measure the concentrations (=peak height) of different chemical compounds (=different frequencies). A sample MR spectrum of a rat brain at 11.75T is given in fig. 1.1. The time distance between two consecutively measured time points is called spectral dwelltime, $dT_{spectral}$, and defines the spectral range in Hz within which we can differentiate chemical compounds. The total duration of the acquisition defines the distance between two neighboring frequencies which can be still resolved (spectral resolution).

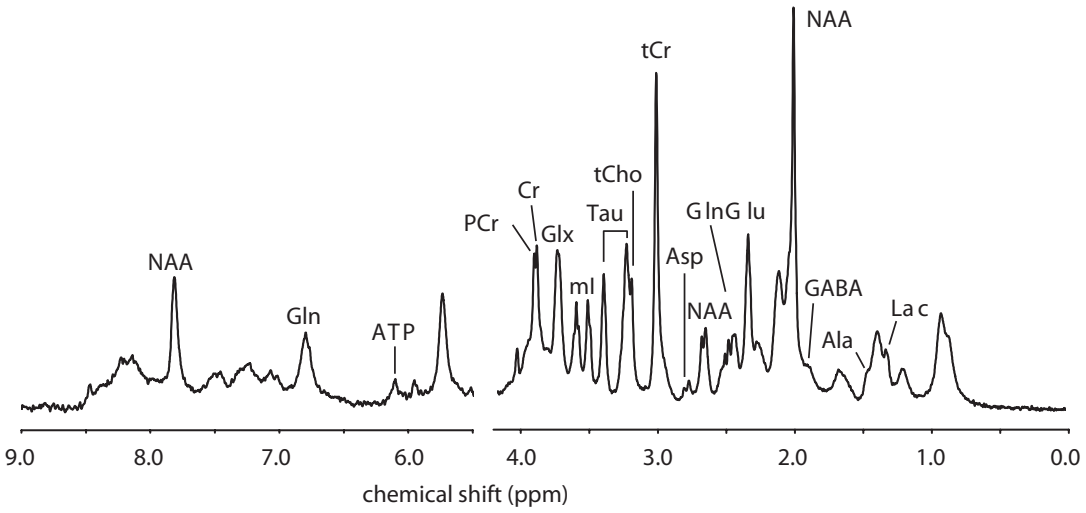

Figure 1.1: Example spectrum of an *in-vivo* rat brain at 11.75 T. Different metabolites (or parts of these) resonate at different frequencies, and therefore produce individual peaks in the spectrum. The area of a peak is proportional to the abundance of the corresponding metabolite. Reprinted with kind permission from: (2).

Instead of providing the frequencies of the different resonances in Hz, a "normalized frequency" called chemical shift is usually used, since the chemical shift does not change with the main magnetic field B_0:

$$\delta := \frac{w - w_{ref}}{w_{ref}} 10^6 \tag{1.2}$$

where w_{ref} is usually defined as the frequency of the chemical compound tetramethyl silane or dimethyl silapentane sulfonic acid. The typical range of metabolites in ^1H-MRS is between 0 and 10 ppm.

1.4 Signal Localization in MR

Without signal localization, *in-vivo* MRI and MRS would be quite useless. There are several signal localization methods in MR. Here, we will restrict ourselves to frequency encoding, phase encoding, and slice encoding.

1.4.1 Gradient Fields and k-Space

All conventional methods for localizing signal in MR require additional linear magnetic fields, often called gradients. They can be described by

$$\vec{B}_G = G_x x \vec{e}_z \tag{1.3}$$

where G_x is the constant gradient along the x-axis.

The MR signal at the location $\vec{r}$ and time t can be described by

$$S(x,t) = S_0(x,t) \cdot \mathrm{e}^{i\omega t} \tag{1.4}$$

where S_0 describes the proton density, signal relaxation and other effects, and the exponential describes the precession of the signal with frequency ω. If we measure the signal unlocalized, however, we cannot distinguish between the different positions, and will thus measure instead

$$S(t) = \int_V S_0(x,t) \cdot \mathrm{e}^{i\omega t}\, dx \tag{1.5}$$

where V is the whole volume from which we can get signal.

Due to the gradients, we can make the frequency ω dependent on the spatial position:

$$\omega(x) = \gamma(B_0 + G_x x). \tag{1.6}$$

Combining both equations, eq. (1.5) and eq. (1.6), yields

$$S(t) = \int_V S_0(x,t) \cdot \mathrm{e}^{i\gamma(B_0+G_x x)t}\, dx \tag{1.7}$$

With the definition for time-constant gradients, $k_x := \gamma G_x t$, we finally arrive at

$$S(t) = \int_V S_0(x,t) \cdot \mathrm{e}^{i\gamma B_0 t} \cdot \mathrm{e}^{ik_x x}\, dx \tag{1.8}$$

which is the inverse Fourier transform of the signal of interest, $S_0(x,t) \cdot \mathrm{e}^{i\gamma B_0 t}$. By measuring the signal for different k_x-values, we can fill the so called "k-space", the discrete and finite equivalent to the infinite and continuous k-space-values of eq. (1.8). We can sample this k-space in a variety of different manners, two of which will be described in the following two sections.

A more general definition of k-space values is given by

$$\vec{k}(t) = \gamma \cdot \int_0^t \vec{G}(\tau)\, d\tau \tag{1.9}$$

where t=0 is defined as the time directly after the signal excitation with an RF pulse (pulsed B_1-field). This definition also leads to a very similar equation like eq. (1.8). From equation eq. (1.9) we can see that the k-space values are simply the time-integral of the gradient function, i.e. the area under the gradient function.

1.4.2 Frequency Encoding

Frequency encoding is a method where gradients are applied during data acquisition, thus traversing through k-space while sampling the data. If we apply a gradient right after the excitation and acquire the signal meanwhile, however, we will only acquire one half of the k-space line. Therefore, usually a so-called "pre-winder" gradient is applied before signal acquisition. This pre-winder has the opposite sign of G_x and half its area. By that, we first traverse to the one side of k-space with the pre-winder, and then acquire the whole k-space line with the frequency encoding gradient.
Although this is the simplest and most common way of frequency encoding, many other ways exist to traverse through k-space with a gradient during data acquisition. Examples are spiral sequences (4), where k-space is covered in two dimensions simultaneously by

spiral trajectories, or CONCEPT (5), where in each Repetition Time (TR) one circle is acquired.

1.4.3 Phase Encoding

Phase encoding is similar to frequency encoding. However, the k-space is not traversed **during** the read-out, but the k-space point which should be measured is reached **before** the read-out, very like the pre-winder in frequency encoding. Therefore, phase encoding gradients have to be applied between the excitation pulse and the acquisition. After we traversed to the intended k-space point, we can do several things: We can measure this single point, like in single-point imaging; the whole k-space can then be filled, by traversing to different k-space points in different excitation periods. Another option is to stay at this k-space location and measure several time points of the same k-space point, thus acquiring an FID. If we do this for all k-space points, we get a spectrum for each spatial location. Thus, this option is a simple phase-encoding MRSI sequence. The third option is to acquire a whole k-space line (or any other suitable trajectory) by applying a frequency encoding gradient during the read-out. If we repeat this for several offsets in the phase encoding direction, we get a simple GRE sequence.

1.4.4 Slice Encoding

Often, we only want to get signal from a single slice, instead of the whole volume to which our reception coils are sensitive to. We can achieve this with slice encoding. In this method, we apply a gradient along one direction during signal excitation. This causes the frequency to depend on the spatial location, given by eq. (1.6). If we make our RF pulse frequency-selective, i.e. it excites only a certain range of frequencies, we can "cut" out a single slice. The slice profile, i.e. how well this slice is defined, depends on our capability to excite only the frequencies we intend to excite, and no others. A perfect slice would require an infinitely long excitation pulse. Therefore, the slice profiles in practice always have a certain transition band, ripples, and over- and undershoots in the pass- and stop-band.

1.5 Array Coils

As a prerequisite of PI, the signal has to be measured by receive array coils. Array coils are coils, which in fact consist of several decoupled coils, often called channels. The physical signal can be measured in parallel by all those channels independently. Each

channel usually has a distinctive sensitivity profile, describing how much the specific channel is sensitive to a given spatial position.

1.6 Acceleration Methods

Acceleration methods accelerate the measurement by omitting time-consuming phase encoding steps (PI, partial fourier, compressed sensing), measuring several k-space points within one spectral dwell time (SSE), or reducing the TR (steady-state free precession sequences). In this thesis I will focus on PI and SSE methods only.

Two important measures are the sensitivity Ψ and the quality factor Ω of a sequence in general, and an accelerated sequence in particular. The sensitivity is defined by the SNR and the total measurement time of the sequence T_{Tot} as

$$\Psi := \frac{SNR}{\sqrt{T_{Tot}}} \tag{1.10}$$

The reason for using the square root of the measurement time, instead of the measurement time itself, is that even for optimal efficiencies, the SNR increases only with the square root of the measurement time, see (6). As Pohmann et al. showed, Ψ depends on many measurement parameters, such as the repetition time TR, the relaxation time T_1 or the acquisition bandwidth (7). However, those are often not of interest, since we only compare different acceleration methods, where most of those parameters stay the same. Therefore it is convenient to relate this sensitivity to a gold-standard sensitivity resulting in the quality factor:

$$\Omega^{Total} := \Omega^{AcqEff} \cdot \Omega^{Density} \cdot \Omega^{Others} = \frac{\Psi_{Sequence}}{\Psi_{PE-MRSI}} \tag{1.11}$$

We can define the gold standard $\Psi_{PE-MRSI}$ as we want, but a wise choice is to always use a very similar sequence as the one we investigate, where all parameters such as TR remain the same, except of those specific to the investigated sequence. The subscript "PE-MRSI" means, that the sequence is a conventional phase encoded MRSI sequence, which was shown to have the highest possible sensitivity, if the parameters such as TR, k-space density, Echo Time (TE), etc. are chosen optimally (7). We can further differentiate the quality factor by examining the reason of the decreased sensitivity compared to PE-MRSI: $\Omega^{Density}$ which describes the decreased sensitivity due to k-space densities

different from the intended (final) one, Ω^{AcqEff} due to acquiring only partly useful data during the read-out, and Ω^{Others} for summarizing all other effects as the g-factor of PI.

2 Coil Combination for MR Spectroscopy: MUSICAL

This thesis starts exactly where my diploma thesis ended, i.e. the coil combination of phase-encoded MRSI data. Although the coil combination was shown to work robustly and well in my diploma thesis, the coil combination was still improved after my graduation, i.e. the data were no longer weighted with the volume coil pre-scan, the channels were noise decorrelated to improve the SNR even further, and the pre-scans were implemented into the phase-encoded MRSI sequence. The proposed coil combination method was called MUSICAL, and was published in the peer-reviewed journal "NMR in Biomedicine" (3).

Following is a short summary how the coil combination was improved during my PhD-studies.

2.1 Motivation

In-vivo ^1H-MRS can provide valuable metabolic information in clinical routine and neuroscience without being invasive, nor including any radioactive substances or ionizing radiation. Yet, several challenges impede the usage of MRS in human brains, most notably the low SNR per Unit Time (SNR/t) due to the low concentration of MR detectable metabolites. The SNR can be improved by using long measurement times, low resolutions, or very high field strengths, such as 7T or above. The measurement times cannot be increased above certain limits due to patient discomfort. Using high field strengths increases the SNR/t, but the signal also decays faster via T_2-relaxation than at lower fields. In order not to loose too much SNR/t, short echo times are required. The shortest possible "echo time" is achieved by directly acquiring the FID, which increases the SNR/t even further. Yet, if no echo is acquired, the signal cannot be spatially restricted to brain-only tissue, e.g. by methods like Point-Resolved Spectroscopy (PRESS). Therefore, if the FID is directly measured with low resolutions, the signal strongly leaks to neighbouring voxels by virtue of the broad Point Spread Function

(PSF). Thus, lipids from the subcutaneous fat layers can spread over the whole brain image, rendering the main brain resonance, N-Acetyl Aspartate (NAA), impossible or hard to quantify. Luckily, however, the very high magnetic field, and the very short "echo times" provide enough SNR to measure high resolutions of about $3.4 \times 3.4\,\mathrm{mm}^2$. By that, signal leakage is largely prevented, as was shown by Bogner et al. Unfortunately, such large resolutions also require long measurement times of about 30 minutes for one slice. Thus, the first aim of my work was to implement a robust coil combination for MRSI data from array coils to further increase the SNR/t. This increased SNR can then be used to accelerate the measurement.

To enable the improved SNR/t, a good coil combination has to be performed. The first question that arises is, why we cannot use the same coil combination as in conventional MRI. The standard coil combination method proposed by Roemer et al. in 1990 (8) is the so called "sum of squares" method. This method does not preserve the phase information of the acquired data, but only their magnitude. Therefore, this method results in absolute-valued spectra, which are known to have much higher line widths than complex-valued spectra (2, p. 18).

Several alternatives were therefore presented, such as using the first FID point as coil weights (9), minimizing the difference between the real and absolute part of the spectra (10), a combination based on the fitting program LCModel (11), measuring sensitivity maps (12), or measuring an additional MRSI scan without water suppression (13). The standard method, using the first FID point as suggested by Brown et al., was shown in my diploma thesis to result in inferior data quality in comparison to MUSICAL for our settings.

A very promising technique is to acquire a so-called "sensitivity map", i.e. a map of how sensitive each coil is to different imaging regions, and what phase each channel imprints into the signal of these regions. If the noise magnitude and correlation between channels is also taken into account, this method was evaluated by Roemer et al. to be the best possible coil combination method (8). However, a reference coil with ideally a homogeneous sensitivity (in magnitude and phase) to the whole imaging region is necessary. We have shown that a modified method without using such a reference coil provides a similar data quality after coil combination (3).

2.2 Methods

2.2.1 Basic MUSICAL

Coil combination can be described in general by

$$S_{Comb}(\vec{r},t) = \lambda(\vec{r}) \cdot \sum_{i}^{N} w_i(\vec{r})\, S_i(\vec{r},t) \tag{2.1}$$

where S_{Comb} is the coil-combined MRSI signal, S_i the uncombined MRSI signal of channel i, w_i the coil combination weight of channel i, N the total number of channels, and λ a scaling function, e.g. for eliminating any coil sensitivities in the final image.
This equation can be rewritten in matrix notation:

$$S_{Comb}(\vec{r},t) = \lambda(\vec{r}) \cdot \mathbf{w}^T(\vec{r})\, \mathbf{S}(\vec{r},t) \tag{2.2}$$

where bold variables represent matrices, in this case of size $N \times 1$; T represents the transposition operator. The method of Brown et al. is defined as

$$S_{Comb}^{Brown}(\vec{r},t) := \frac{1}{\mathbf{S}^H(\vec{r},0)\mathbf{S}(\vec{r},0)} \cdot \mathbf{S}^H(\vec{r},0)\, \mathbf{S}(\vec{r},t) \tag{2.3}$$

with H being the Hermitian operator. This method weights the spectroscopic signal of channel i, $S_i(\vec{r},t)$, with the complex conjugated first FID point at time $t = 0$, $S_i(\vec{r},0)$. It therefore has similarities with the sum of squares method of MRI, where the data are weighted with the complex conjugated of the same data. The method used in my diploma thesis, i.e. the sensitivity map method is defined as

$$S_{Comb}^{Sensmap}(\vec{r},t) := \frac{I_{VC}(\vec{r})}{\mathbf{I}^H(\vec{r})\mathbf{I}(\vec{r})} \cdot \mathbf{I}^H(\vec{r})\, \mathbf{S}(\vec{r},t) \tag{2.4}$$

$\mathbf{I}$ is the imaging signal of size $N \times 1$, e.g. from a pre-scan without water suppression, I_{VC} is the same but acquired with the volume coil. It is important to stress that this method has a different scaling as it introduces the scaling of the volume coil by multiplying with I_{VC}. After the diploma thesis, I omitted the pre-scan signal of the volume coil resulting in

$$S_{Comb}^{MUSICAL}(\vec{r},t) := \frac{1}{\mathbf{I}^H(\vec{r})\mathbf{I}(\vec{r})} \cdot \mathbf{I}^H(\vec{r})\, \mathbf{S}(\vec{r},t) \tag{2.5}$$

This has five advantages. First: One imaging set can be omitted. Second: The volume coil data can add some additional variability and noise, which is avoided. Third: The spectra are already phased, thus the spectral fitting routine has fewer degrees of freedom, which usually improves the fitting. Fourth: The method can be used if no reference coil is available. Fifth: With all the sensitivity information of the coils removed, the first step towards water referencing (sometimes called “absolute quantification”) is already

done.

Six volunteers were measured on a Siemens 7 T scanner (Magnetom, Siemens Healthcare, Erlangen, Germany) with a head coil with 32 receive channels and a volume coil for receiving and transmitting RF signals (Nova Medical, Wilmington, USA). One volunteer had to be excluded due to motion artifacts.

A three-dimensional Magnetization-Prepared Rapid Gradient-Echo (MPRAGE) sequence was measured for creating a brain mask and as an anatomical reference. The inversion time was 1.7 s, the TR 3 s, the TE 3.41 ms. A matrix size of $256 \times 246 \times 160$, Generalized Autocalibrating Partially Parallel Acquisitions (GRAPPA) factor of 3, and a Field of View (FoV) of $230 \times 230 \times 160\text{mm}^3$ was used.

The MRSI sequence was run with an FoV of $220 \times 220\text{mm}^2$, one slice with a slice thickness of 12 mm, a matrix size of 64×64. The TR was 600 ms, the acquisition delay 1.3 ms, the spectral bandwidth was 6 kHz, and 2048 FID points were acquired. Water Suppression Enhanced Through T1-Effects (WET) was used for a weak water suppression (14).
A GRE sequence was acquired with the 32-channel AC as well as with the single channel Volume Coil (VC) with the same parameters as the MRSI sequence, except of a matrix size of 128×128, a TR of 4 ms and a lower flip angle of 8°. This data were used for the Sensmap and the MUSICAL coil combination method.

A brain mask was created using Brain Extraction Tool v2 (BET2) from the MPRAGE data. The AC MRSI data were coil-combined using the three methods described by eqs. (2.3) to (2.5), after which they were Hamming filtered in k-space. The voxels within the brain mask were fitted with LCModel for all three coil-combined data sets, as well as the VC data set. Since the data were acquired with a pulse-acquire (FID-based) sequence, the acquisition delay caused a first-order phase error in the spectrum, as illustrated by fig. 2.1a. The same error was introduced into the basis set spectra as proposed by Henning et al. (15) to correct for the acquisition delay. The basis set spectra are used for fitting the measured spectra by LCModel. The SNR was calculated with an own MATLAB script, which takes the amplitude of the total N-Acetyl Aspartate (tNAA) signal divided by twice the standard deviation of the signal in regions where no metabolites resonate, see chapter 5. However, the spectra sometimes contained artifacts in those regions as well as resonances if the spectra were shifted severely due to B_0-

inhomogeneities. In such cases, the script automatically detects and excludes these peaks.

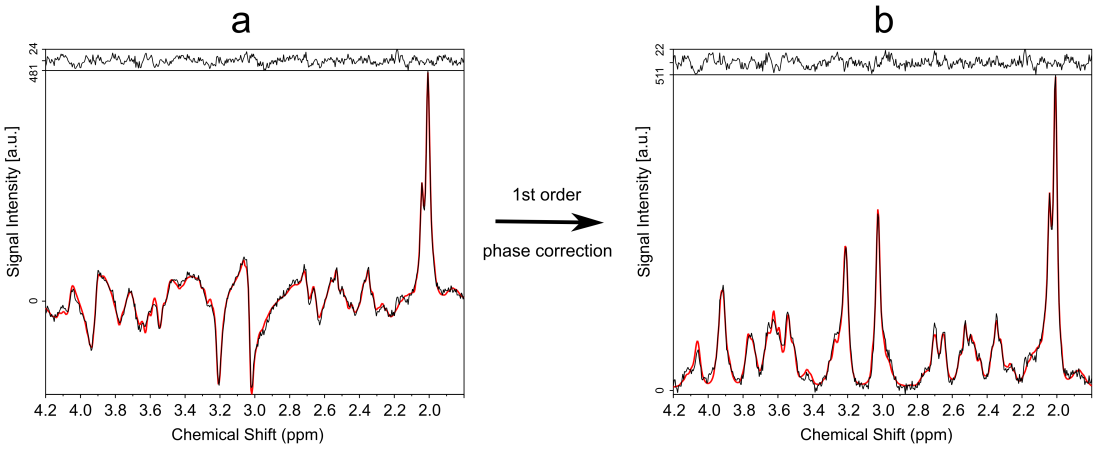

Figure 2.1: In a, a spectrum (black curve) without correcting the first order phase error was fitted by LCModel with a basis set (red curve) to which the same first order phase error was introduced. This method was used in this work. In b, the same spectrum was first order phase corrected and fitted by LCModel with a basis set without phase error. Reprinted from: (3).

A comparison between the standard coil combination method of Brown et al., the original MUSICAL method of my diploma thesis (i.e. sensitivity map method), and the new method is given, including metabolic maps, Cramér-Rao lower bound (CRLB) maps, and spectra. The SNRs and CRLBs of the different methods are compared statistically.

2.2.2 Noise-Decorrelated MUSICAL

When measuring with an array coil, the signals detected by the individual channels are not independent, but influence each other. This influence can be measured by acquiring noise-only data, $\mathbf{X}$ of size $M \times N$, and then calculating the correlation between different channels via

$$\Psi_{ij} = \frac{\mathbf{X}_i^H \mathbf{X}_j}{2k} \tag{2.6}$$

where Ψ_{ij} describes the noise correlation matrix between channel i and j. This noise correlation can be undone by "pre-whitening" the data, i.e. making the noise Gaussian and of unity variance for each channel. By that the SNR of the final signal is increased for two reasons: Firstly, the noise decorrelation between the channels improves the SNR by itself. Secondly, by making the noise of all channels of variance one, channels with

high noise powers are weighted less than those with low noise. Thus, the individual channels are effectively not weighted by their coil sensitivity, but by the coil SNR, which was shown to result in highest SNR (16). (This is not in contrast to Roemer et al. (8), as Roemer et al. assumed idealized, noise-free sensitivity maps.)

Thus, the MUSICAL coil combination equation (2.5) was further modified to

$$S_{Comb}^{MUSICAL2}(\vec{r},t) = \frac{1}{\mathbf{I}^H(\vec{r})\mathbf{\Psi}^{-1}\mathbf{I}(\vec{r})} \cdot \mathbf{I}^H(\vec{r})\mathbf{\Psi}^{-1}\mathbf{S}(\vec{r},t) \tag{2.7}$$

Since $\mathbf{\Psi}$ is a positive definite, Hermitian matrix, a Cholesky decomposition can be performed on $\mathbf{\Psi}$, resulting in $\mathbf{\Psi} = \mathbf{L}\mathbf{L}^H$, with $\mathbf{L}$ being a lower triangular matrix (17). Therefore, eq. (2.7) can be rewritten as:

$$\begin{aligned} S_{Comb}^{MUSICAL2}(\vec{r},t) &= \frac{1}{(\mathbf{I}^H(\vec{r})(\mathbf{L}^H)^{-1})(\mathbf{L}^{-1}\mathbf{I}(\vec{r}))} \cdot (\mathbf{I}^H(\vec{r})(\mathbf{L}^H)^{-1}))(\mathbf{L}^{-1}\mathbf{S}(\vec{r},t)) = \\ &= \frac{1}{(\mathbf{L}^{-1}\mathbf{I})^H(\vec{r})(\mathbf{L}^{-1}\mathbf{I}(\vec{r}))} \cdot (\mathbf{L}^{-1}\mathbf{I})^H(\vec{r})(\mathbf{L}^{-1}\mathbf{S}(\vec{r},t)) = \\ &=: \frac{1}{\mathbf{I}_{Prew}^H(\vec{r})\mathbf{I}_{Prew}(\vec{r})} \cdot \mathbf{I}_{Prew}^H(\vec{r})\mathbf{S}_{Prew}(\vec{r},t) \end{aligned} \tag{2.8}$$

The last equality of eq. (2.8) has the same form as the basic coil combination, eq. (2.5), with the only difference that the "pre-whitened" signals $\mathbf{I}_{Prew}$ and $\mathbf{S}_{Prew}$ are used. Thus, the noise decorrelation can be performed very conveniently by only applying $\mathbf{L}^{-1}$ to the input data, and then ignoring the noise correlation altogether, since the pre-whitened data have a noise correlation equal to the identity matrix.

The noise decorrelation was tested on the same volunteers as the basic coil combination. The same processing was used, except for the coil combination which was performed according to eq. (2.8) instead of eq. (2.5). The noise for the noise decorrelation was gathered by using the end of the FIDs at spatial locations outside of the head. The SNR was statistically compared between using noise decorrelation and not using it.

2.2.3 Pre-Scan Implementation into MRSI Sequence

During my diploma thesis, the pre-scan for coil combination, $\mathbf{I}$, was measured with a standard GRE imaging sequence. When the noise decorrelation was later performed, an unlocalized pulse-acquire FID sequence with a flip angle of 0° was added to acquire noise-only data $\mathbf{X}_i$. For convenience reasons, these pre-scans were implemented into the

MRSI sequence. For the noise pre-scan, the signal is acquired for about 1.4 s, measuring 132000 complex points. For the GRE pre-scan, a simple GRE imaging sequence of about 2.4 s duration was integrated into the MRSI sequence together with my colleague Gilbert Hangel, and run before the actual MRSI scan.

One volunteer was measured as described above, except that no VC measurement was performed. Instead, the volunteer was measured with the new MRSI sequence including the pre-scans, and the external pre-scans were additionally measured. These data were used for comparing the integrated GRE imaging sequence with the external one.

The GRE images of the integrated pre-scan were compared with the ones from the external GRE sequence.

2.3 Results

2.3.1 Basic MUSICAL

Example spectra for the three different coil combination methods and the VC are given in fig. 2.2. Metabolic ratio maps of total Creatine (tCr) / tNAA and total Choline (tCho) / tNAA are provided for volunteer 5 in fig. 2.3. Fig. 2.4 shows the CRLB maps of the metabolites *Gamma*-Aminobutyric Acid (GABA) and Taurine for volunteer 3.

The SNRs of the different coil combination methods are shown in table 2.1. The CRLB values of seven different metabolites, averaged over all five volunteers, are provided in table 2.2. The number of brain voxels with CRLB values > 20 % of the metabolites GABA, *Myo*-Inositol (Ins), Tau, tCho, tNAA, tCr, and Glutamine and Glutamate (Glx) were 9.2 %, 9.0 %, and 17.6% of all CRLB values for the MUSICAL, Sensmap, and Brown method, respectively. The MUSICAL CRLB values were similar to the Sensmap method with a p-value of $p > 0.6$ using a paired t-test, but 33 % lower than for the Brown method with $p < 0.05$. The mean CRLB values of the different volunteers were used as the statistical population. MUSICAL and Sensmap SNR values were also almost the same, with MUSICAL having on average 1.7 % higher SNRs with $p < 0.01$, but 29.4 % higher values than the Brown method with $p < 0.001$.

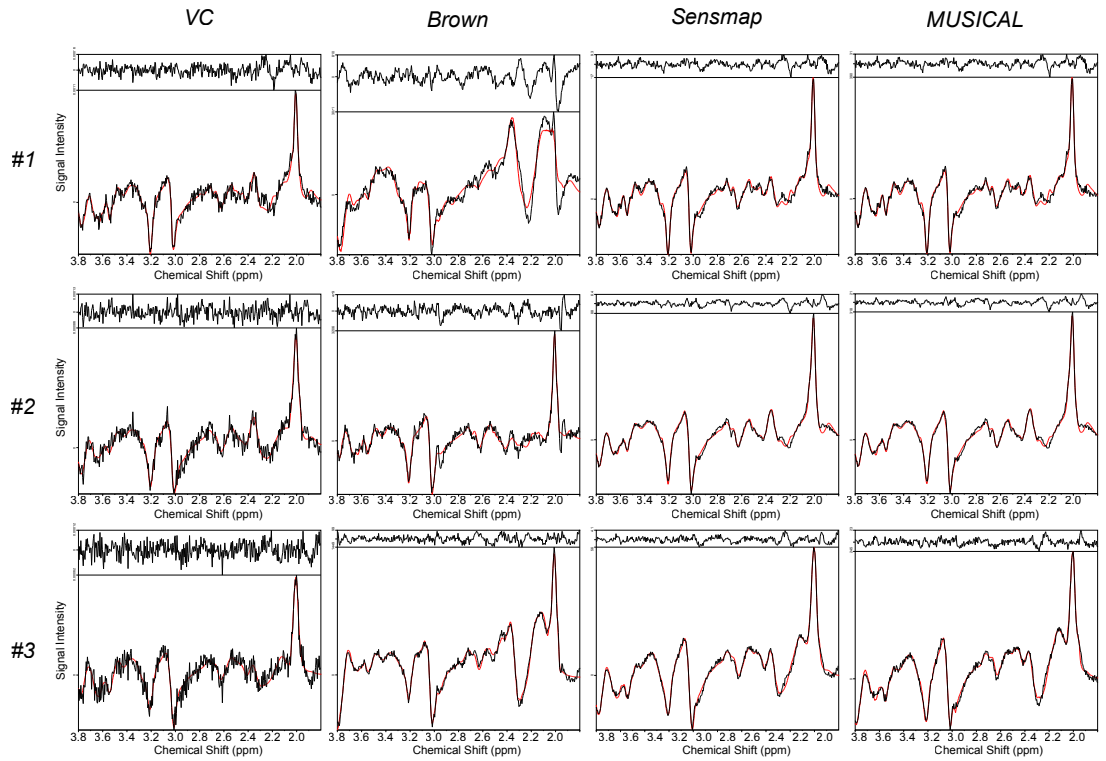

Figure 2.2: Comparison of example spectra resulting from the volume coil and the array coil with the three different coil combination methods. The VC spectra do not have any artifacts, but the SNR is quite low. The spectra resulting from the Brown method show more artifacts than the other spectra. Adapted from: (3).

Volunteer	Brown SNR [ ]	Sensmap SNR [ ]	MUSICAL SNR [ ]
1	50.8 ± 18.3	67.4 ± 19.2	68.5 ± 19.2
2	58.5 ± 16.2	74.7 ± 17.3	76.0 ± 18.5
3	65.6 ± 22.9	87.9 ± 25.1	88.6 ± 26.0
4	62.6 ± 23.1	73.9 ± 19.1	76.3 ± 19.7
5	64.9 ± 14.7	80.8 ± 14.4	82.3 ± 13.6

Table 2.1: SNR values of all volunteers and the three different coil combination methods. The SNRs of the Brown method are much lower in comparison to the other two methods, which have comparable SNRs. Adapted from: (3).

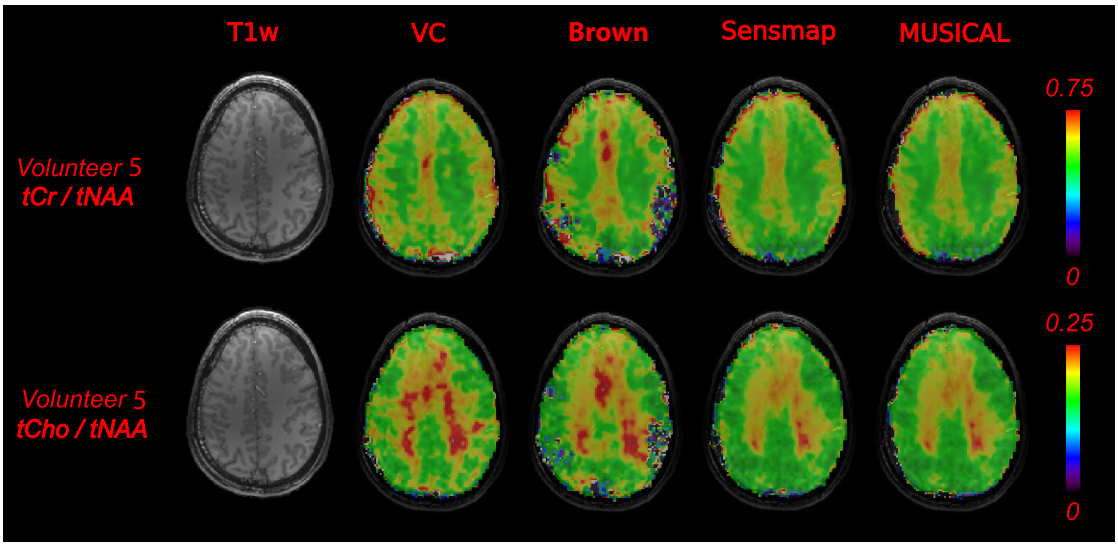

Figure 2.3: A T_1-weighted image (left) and the metabolic ratio maps tCr/tNAA and tCho/tNAA for the VC and the three different coil combination methods. The Brown method resulted in more artifacts than the other methods, especially at the border of the brain. Adapted from: (3).

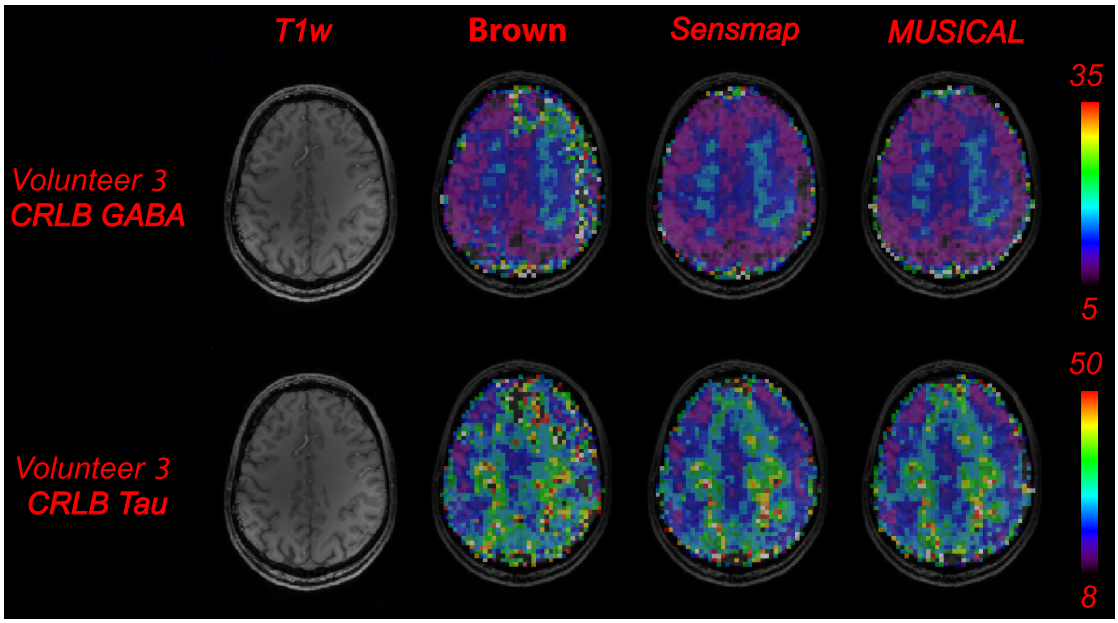

Figure 2.4: A T_1-weighted image of the same slice as the GABA and Taurine CRLB maps of volunteer 3. Both maps have higher values in case of the Brown method, especially at the frontal right brain regions. Adapted from: (3).

2.3.2 Noise-Decorrelated MUSICAL

The SNR values of MUSICAL without and with noise decorrelation are given in table 2.3. The SNR increased by 12.1 % on average ($p < 0.001$) when comparing the average values of the five different volunteers.

Metabolite	Brown CRLB [%]	Sensmap CRLB [%]	MUSICAL CRLB [%]
GABA	17.5 ± 16.5	14.8 ± 14.6	14.8 ± 14.9
Ins	10.0 ± 12.3	6.5 ± 8.0	6.7 ± 8.5
Tau	30.8 ± 16.6	22.4 ± 12.5	22.0 ± 12.2
tCho	8.9 ± 11.9	5.3 ± 7.0	5.4 ± 7.4
tNAA	6.1 ± 10.7	3.4 ± 5.6	3.5 ± 6.4
tCr	11.1 ± 16.0	6.3 ± 10.2	6.6 ± 10.9
Glx	7.8 ± 10.3	5.1 ± 4.7	5.1 ± 5.1

Table 2.2: CRLB values of all volunteers and the three different coil combination methods. The values of the Brown method are significantly higher than those of the two other methods. Adapted from: (3).

Volunteer	MUSICAL SNR [ ]	MUSICAL NoiseDecorr SNR [ ]
1	68.5 ± 19.2	79.7 ± 25.1
2	76.0 ± 18.5	86.3 ± 22.5
3	88.6 ± 26.0	99.2 ± 30.6
4	76.3 ± 19.7	85.3 ± 22.0
5	82.3 ± 13.6	91.9 ± 16.3

Table 2.3: Comparison of the SNR values of all five volunteers between the standard MUSICAL coil combination described by eq. (2.5) and the noise decorrelated version of eq. (2.8). All data sets have a higher SNR when noise decorrelation is performed. Adapted from: (3).

2.3.3 Pre-Scan Implementation into MRSI Sequence

An image comparing images of the external GRE imaging sequence and the one programmed into the MRSI sequence is shown in fig. 2.5.

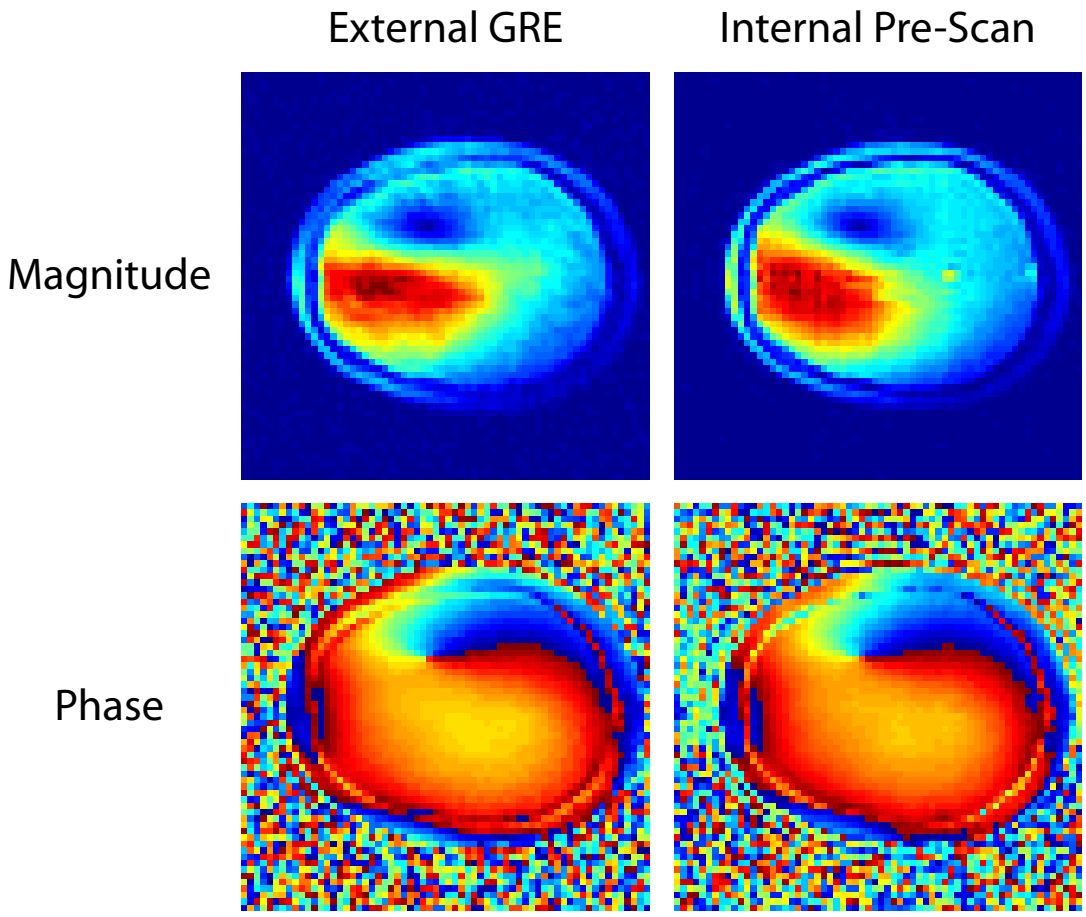

Figure 2.5: Comparison of the magnitude and phase of the external GRE imaging sequence (left) to the one programmed into the MRSI sequence (right). The external GRE image was phased with a constant phase because a different resonance frequency was used in comparison to the MRSI sequence. The magnitude, as well as the phase, of both sequences are very similar, showing that the implementation of the pre-scan into the MRSI sequence was successful.

2.4 Discussion

2.4.1 Basic MUSICAL

The MUSICAL and Sensmap coil combinations were shown to improve the results in comparison to the method proposed by Brown et al. MUSICAL and the Sensmap method provided comparable data quality, but MUSICAL needs less data to acquire, results in spectra which are already phased, and furthermore intrinsically provides metabolic ra-

tios maps to water, as shown in the outlook section.

2.4.2 Noise-Decorrelated MUSICAL

Noise decorrelation has already been shown previously to substantially improve the SNR when using array coils (18–20). This was confirmed in this work. It is important to note that noise decorrelation improves data quality without almost any cost, other than negligible extra processing time, and a very short noise scan, as implemented into the pre-scan of our MRSI sequence. In MRSI, this can be even omitted by using the noise at the end of the FID of voxels void of any signal, as it was done here.

2.4.3 Pre-Scan Implementation into MRSI Sequence

The GRE pre-scan implemented into our MRSI sequence provides a similar data quality as the external GRE sequence, but is less prone to user errors, as it performs all necessary adjustments automatically, such as using the same shim as in the MRSI sequence, or the same slice thickness, slice positions etc. Especially when several slices were measured, one measurement per slice at the correct position had to be performed with the external GRE sequence. This made the handling of the pre-scans very tedious and prone to errors.

2.4.4 Comparison to Literature

The method of Brown et al. is the standard method for combining the channels of MRSI data, and is implemented at different MR scanners. The resulting data quality was shown to be worse than that of the proposed method, MUSICAL. The reason why the standard method of Brown et al. performed worse might be due to high lipid signals in comparison to the water signal. This is supported by the fact that the Brown method performed badly especially at the border of the brain. The method of Brown takes the first FID points of each channel, and uses these magnitudes and phases for weighting and phasing the individual channels. The first FID point is dominated by the highest signals in the spectrum, which are normally either the remaining water signal after water suppression, or the lipids. Due to the broad PSF of MRSI data and the spatial sensitivity of the individual channels of the AC, the relative lipid signal can change from channel to channel, which therefore disturbs the weights calculated by the first FID point. Although this problem always occurs, it is especially problematic when using

such a short acquisition delay and no lipid suppression, because the lipids have short T_2-values and their signals are therefore much stronger at short echo times in comparison to longer echo times. In MUSICAL, on the other hand, the weights are calculated from non-water-suppressed data, and therefore the lipids have no influence on the weights.
Another reason for the low data quality resulting from the Brown method might be that the water suppression greatly reduces the signal of the first FID point, and thus increases the coil weights uncertainty, as shown by Dong and Peterson (21).

Therefore, Dong and Peterson proposed to measure the MRSI data without water suppression, which results in reliable weights derived from the first FID point (21). However, this method cannot be easily implemented if short echo times are used due to sideband artifacts caused by the unsuppressed water (22). Prock et al. suggested to minimize the difference between the real and magnitude part of the spectrum to estimate the phase of the weights (10). Maril and Lenkinski used LCModel to determine the complex coil combination weights. Both methods may fail for spectra with low SNR, as it often occurs at large distances to the channel (11). For the method using LCModel, the high phase variability at low SNRs was shown (3). Therefore, a non-optimal coil combination is expected.

The sensmap method provides robust coil combination weights, and the acquired sensitivity maps can be further used for the PI method Sensitivity Encoding (SENSE). Yet, the method needs an additional reference coil, and introduces the sensitivity of this coil, which may decrease the fit quality due to increased data variability.
Measuring another MRSI data set without water suppression in addition to the normal one can also provide robust coil combination weights, but at the cost of increased measurement times (13, 23).

In comparison, MUSICAL only takes about 3 s, provides reliable coil combination weights even for low SNR, can be used with water suppressed MRSI data, does not need any reference coil, and is easy to implement.

2.4.5 Outlook

MUSICAL provides intrinsic water scaling, i.e. the resulting metabolic maps are already ratios to water. Only the different T_1-weightings due to different TRs of the MUSICAL pre-scan and the normal MRSI scan, and the different T_1-values of water and the metabolites have to be taken into account. The intrinsic water scaling can be

explained as follows: When calculating $\frac{1}{\mathbf{I}^H(\vec{r})\mathbf{I}(\vec{r})} \cdot \mathbf{I}^H(\vec{r})\,\mathbf{S}(\vec{r},t)$ in the coil combination, eq. (2.5), the metabolic maps resulting from $\mathbf{S}(\vec{r},t)$ are proportional to the metabolite concentrations, and $\mathbf{I}(\vec{r})$ is proportional to the water content, since no water suppression is used. In the process of coil combination, the metabolic information is weighted with the water content, $\mathbf{I}^H(\vec{r})\,\mathbf{S}(\vec{r},t)$. To cancel this effect, we divide the data by $||\mathbf{I}(\vec{r})||$. However, we divide the result once more by $||\mathbf{I}(\vec{r})||$, since $\mathbf{I}^H(\vec{r})\mathbf{I}(\vec{r}) = ||\mathbf{I}(\vec{r})||^2$, which thus makes the final data proportional to the metabolite concentrations divided by the water content.

This fact is proven by fig. 2.6 which shows that MUSICAL intrinsically enables water scaling without any additional measurements, as the tNAA map from the MUSICAL method (left) looks almost the same as the gold standard (right), except for a constant scaling factor. The water map of the gold standard was created from an additional MRSI measurement without water suppression and a TR of 200 ms. In both cases, the T_1-weighting due to the different TRs of the target MRSI data set (600 ms), the GRE pre-scan (10 ms) and the additional water MRSI scan (200 ms) was considered, as well as the T_1-relaxation difference between tNAA and water.

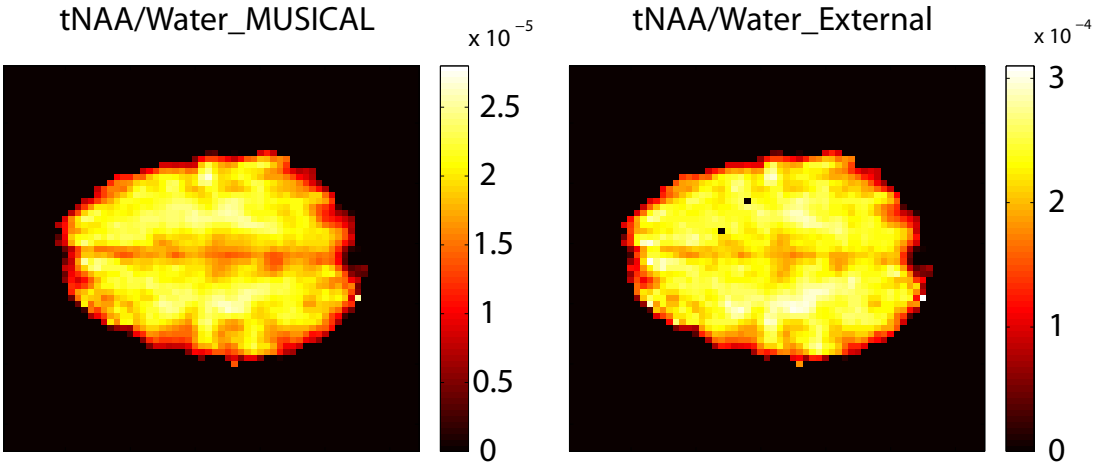

Figure 2.6: Image comparing the tNAA/water maps resulting from MUSICAL (left), and using additional MRSI data without water suppression (right). The images are very similar, except for an additional, constant scaling factor. In both cases, the T_1-weighting effects due to different TRs between the water scan and the MRSI scan, and due to different T_1s between water and tNAA were considered.

The work for the water scaling was done by my colleague Eva Heckova. It is only shown here to give the reader an outlook of the additional benefits of MUSICAL compared to the Sensmap method.

The additional SNR gained by using an array coil and by noise decorrelation can be traded to accelerate the measurement. This can be done with several methods, two of them are PI and SSE. PI was extensively tested for our MRSI data, which is described in chapter 3. SSE was tested in parts, as described in chapter 4, but is still under development.

3 Accelerated MRSI via Parallel Imaging

3.1 Motivation

In chapter 2, the reason for using ACs and and high resolutions was already motivated. Array coils result in higher SNR/t, and high resolutions lead to an improvement of the PSF, which is necessary to manage lipid artifacts, when no other means of reducing lipids is used (24). High resolutions of e.g. a 64×64 matrix, however, increase the measurement time to 30 minutes for one slice with a TR of 600 ms. This is too long for the usage in clinical routine, especially because the patient must not move during the whole time. Thus, the MRSI acquisition has to be accelerated. One possibility is presented in this chapter, another one in chapter 4.

Several PI methods have been used in MRSI, such as SENSE (25–35) or GRAPPA (36–41). However, these studies accelerated only along one or at most two spatial dimensions, although three spatial dimensions are available for PI acceleration in phase-encoded 3D- or multislice-MRSI. Therefore, a new PI method, (2+1)D-CAIPIRINHA, was proposed in the peer-reviewed journal "Magnetic Resonance in Medicine" (42). This method accelerates in-plane with 2D-Controlled Aliasing In Parallel Imaging Results In Higher Acceleration (CAIPIRINHA), while the slice-encoding is accelerated with 1D-CAIPIRINHA.

3.2 Theory

The principle of Parallel Imaging is to omit some of the phase encoding steps for signal localization in order to accelerate the measurement. As a result, spatial aliasing occurs. With the aid of the intrinsic signal localization of the different AC channels, and some training data, we can differentiate between the different aliased signal origins, and thus unalias the signal. This reconstruction can be done in k-space (GRAPPA-like algorithms (43)), or in the image domain (SENSE-like algorithms (44)).

3.2.1 2D-GRAPPA

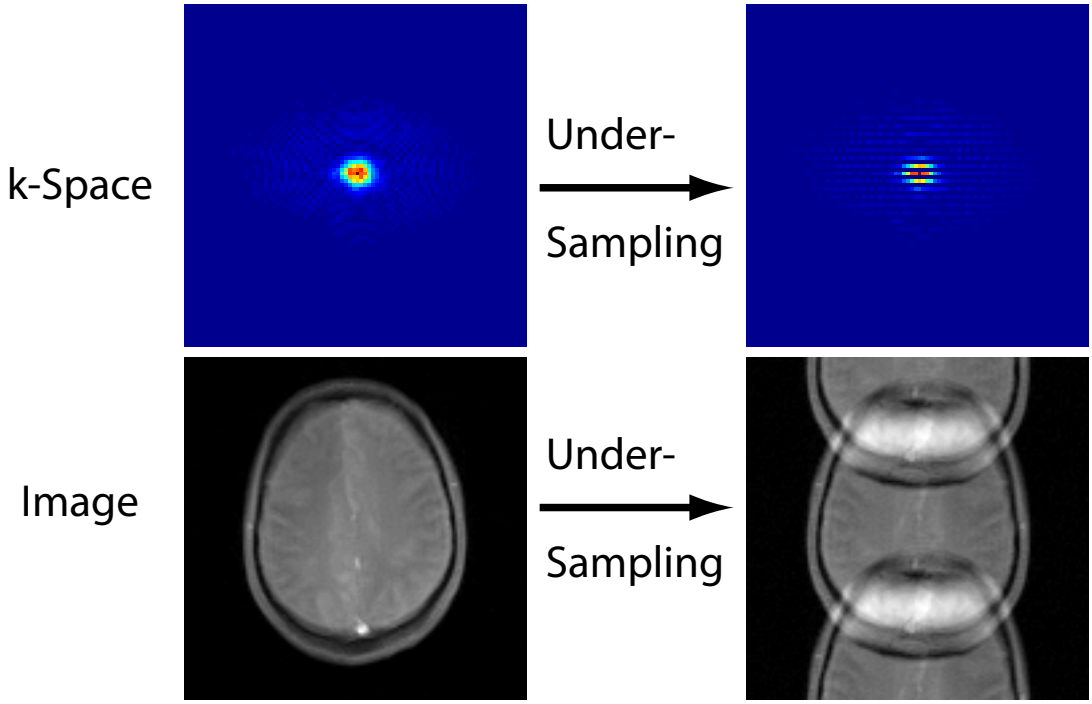

Figure 3.1: Sample k-space and image before and after under-sampling via PI. In k-space, every second line is omitted, resulting in aliasing in the image domain.

2D-GRAPPA is simply the consecutive application of 1D-GRAPPA as proposed in (43). In 2D-GRAPPA and all other in-plane PI methods, parts of the k-space points are omitted. This results in aliasing in the image-domain, as depicted in fig. 3.1. Therefore, instead of measuring the signal of a single spatial locations, the sum of multiple voxels is measured. In order to perform a GRAPPA-like reconstruction, we need two data sets: The under-sampled data set of the image which should be reconstructed, and the so called Auto-Calibration Signal (ACS) data set, as depicted in fig. 3.2b, and 3.2a, respectively. It is important to stress that the ACS data must contain also those k-space points which are missing in the actual under-sampled image. The contrast of the ACS image, however, can be different. Therefore we can measure the ACS data rapidly, with a contrast that is not optimal for the medical question. Yet, the SNR of the ACS image should be as high as possible. One such example is to measure a GRE image without water suppression for reconstructing phase-encoded MRSI data with water suppression. The contrast of the ACS data will be different, as no water suppression is used. At the same time, the SNR of the ACS data is much higher, because of the strong water signal.

Furthermore, the measurement time of the GRE image is negligible in comparison to the MRSI sequence. Therefore, PI is very efficient in MRSI.

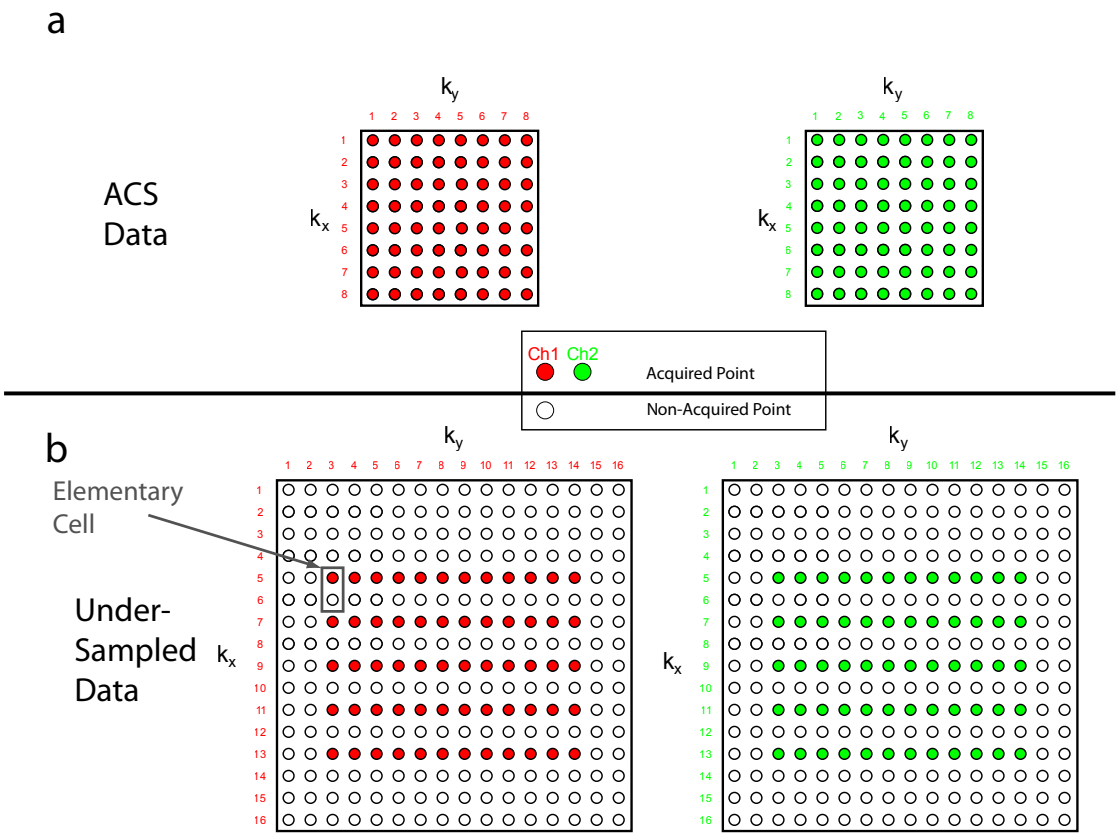

Figure 3.2: Sample representation of the data that is necessary for PI: ACS data and the actual under-sampled data which should be reconstructed, both of at least two channels of an AC. The ACS k-space is usually smaller, in this case 8×8, whereas the under-sampled data are of size 12×12, zero-filled to a size 16×16. In the under-sampled data, every second k-space line is missing. These lines have to be reconstructed using a PI method such as GRAPPA. The elementary cell is the smallest pattern which results in the under-sampled data when replicated. The elementary cell is indicated by a gray box.

One important fact is that PI influences the SNR of the data. Because fewer independent measurements are acquired, the SNR decreases with the square root of the acceleration factor R. Furthermore, because the reconstruction is not perfect, the SNR additionally drops with a factor called the g-factor, which can be described as follows:

$$SNR_{InPlanePI} = \frac{SNR_{Full}}{g \cdot \sqrt{R}} \tag{3.1}$$

Since the SNR of the fully sampled data also scales with the measurement time, which is equivalent to the acceleration factor R in eq. (3.1), the quality factor of in-plane PI is

$$\Omega_{InPlanePI}^{Total} = \Omega_{InPlanePI}^{Others} = \frac{1}{g} \tag{3.2}$$

The GRAPPA-like image reconstruction can be performed as described in the following two sub-chapters.

Calculating the Weights

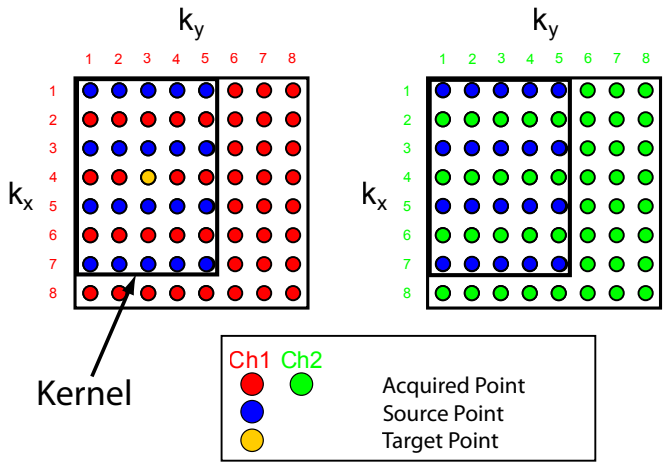

Figure 3.3: The process of calculating the GRAPPA-weights. Two 8×8 ACS data sets for two different channels are shown. The kernel is slided through the whole k-space to gather all P possible repetitions of the kernel in the ACS data (in this example it is 8: four repetitions in ky- and two in kx-direction). Since we know the target and the source points in the ACS data, we can calculate the pseudo-inverse to get the weights. This process is repeated for all channels and all target points in the elementary cell (in this case there is only one target point per channel).

Consider an elementary cell or under-sampling pattern which yields the under-sampled data when replicated, see fig. 3.2. The filled dots in this figure represent the measured points (source points), whereas the empty circles represent missing data (target points). If we focus now on one target point, we can draw a "kernel" around this target point, which includes L source points close to the target point. This is shown in fig. 3.3. We can then calculate the target point of channel i and at k-space position (j,k), T(i,j,k), by a weighted sum of the neighboring source points S(q,j+m,k+n) of channel q and k-space position (j+m,k+n) within the kernel as follows:

$$T(i,j,k) = \sum_{m,n \,|\, (j+m,k+n) \in Kernel} \sum_{p} W(i,j+m,k+n,q) S(q,j+m,k+n) \qquad (3.3)$$

where W are the weights that translate from the source points of all channels to one target point of all channels. For the motivation of this equation I recommend reading the original GRAPPA article (43). We can rewrite eq. (3.3) in matrix notation by merging the last two dimensions of S and T, and the last three of W:

$$T = W \cdot S \qquad (3.4)$$

with T, W and S being matrices of size $N \times 1$, $N \times L \cdot N$, and $L \cdot N \times 1$, respectively. So far this is simple algebra, and no magic at all. But here comes the trick: The weights defined above are shift invariant in k-space. That fact has two implications: First, we can calculate the weights more accurately if we average over all shifts of our kernel in the ACS data. Second, we can acquire for example a 32×32 ACS dataset, calculate the weights from it, and apply those weights to the 64×64 under-sampled data set, even at k-space locations we never calculated the weights in the ACS data for.
Therefore, we can loop over all P possibilities to fit our kernel into the ACS data, each time with different target and source points, and gather all those data in the matrices T and S, which have now sizes $N \times P$ and $L \cdot N \times P$. Then, we can calculate the weights W of size $N \times L \cdot N$ using the pseudo-inverse:

$$W = T \cdot pinv(S) \qquad (3.5)$$

The pseudo-inverse does the job of averaging over all our P repetitions of the kernel in the ACS data in the manner of a least-square error minimization.

In order to be able to reconstruct all target points, we have to calculate an own weighting set for each target point (missing point) in the elementary cell. In the example of fig. 3.3, there is only one missing point in the elementary cell, however.

Applying the Weights

In the second step of the PI reconstruction, we simply apply the calculated weights of the previous step, to calculate the missing target points from the measured source points. Therefore, we loop through all channels and all target points in the elementary cell and find all duplicates of the current target points in the measured k-space. Each

target point in the elementary cell occurs several times in the undersampled data, and is therefore called target point group. Then all these target points are calculated using eq. (3.4), one target point after another, each with its own set of source points. The weights between different target point groups may differ from one another. This process is depicted in fig. 3.4.

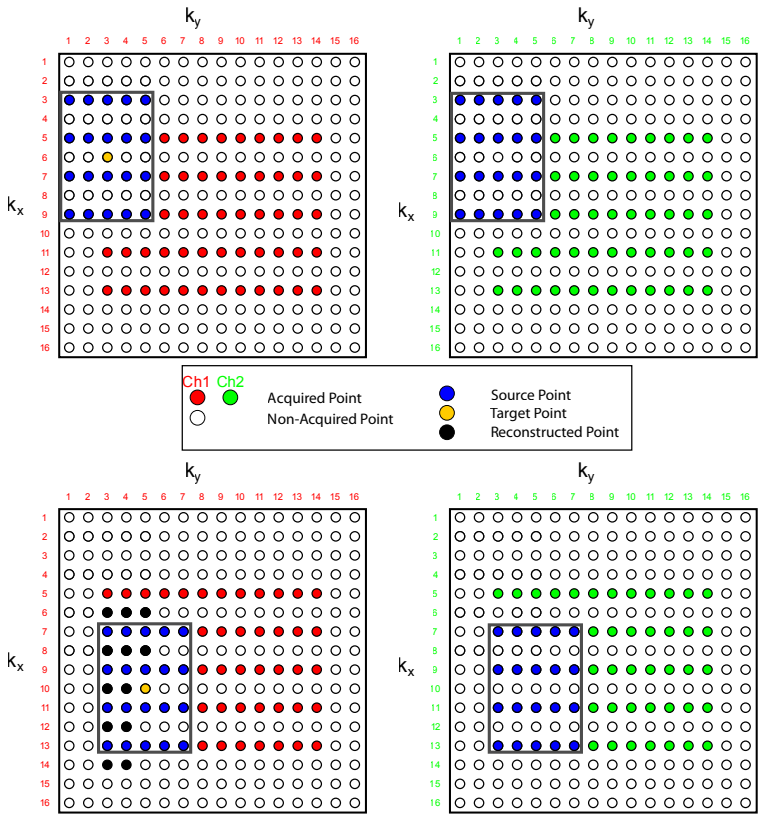

Figure 3.4: Applying the weights to reconstruct the missing points. In the upper subfigure, the first missing point is reconstructed with the aid of all source points of all channels. The lower figure shows how a different target point is reconstructed, while some missing points were already reconstructed (black dots).

3.2.2 2D-CAIPIRINHA

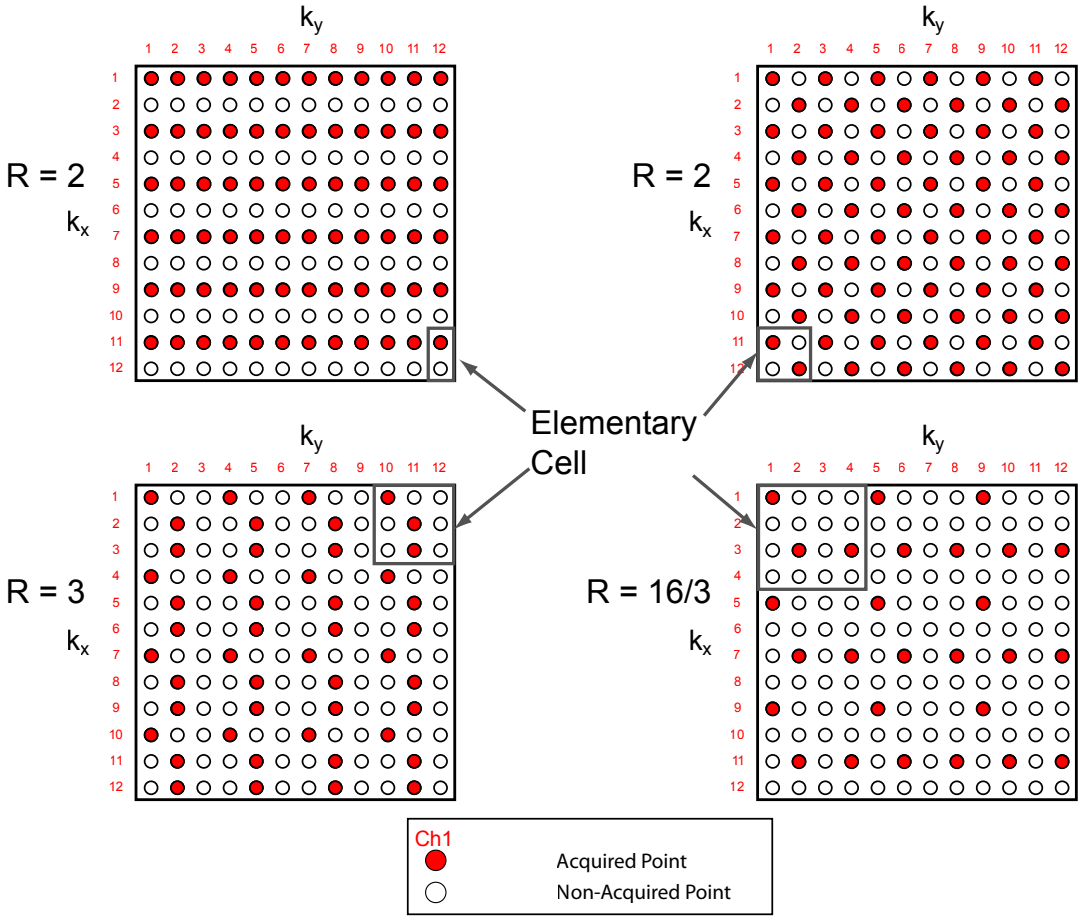

Figure 3.5: Four 2D-CAIPIRINHA example patterns. The upper left is a classical GRAPPA pattern with an acceleration factor of 2. The upper right pattern also results in an acceleration of 2, but shifts every second k-space point, resulting in a checkerboard-pattern. In the lower row, two further patterns with higher acceleration factors are shown.

So far, only GRAPPA under-sampling patterns were shown, where whole lines or columns are omitted. 2D-CAIPIRINHA patterns improve the reconstruction quality by generalizing the undersampling patterns (45). These patterns omit any points in the elementary cell, only restricted to achieve the intended acceleration factor $R = \frac{\text{Number Of Total Points}}{\text{Number Of Acquired Points}}$. Four such example patterns and their replication to a 12×12 matrix are shown in fig. 3.5. Otherwise, the reconstruction of 2D-CAIPIRINHA is very similar to 2D-GRAPPA, outlined as above. Using such generalized under-sampling patterns has the advantage that the distance between an omitted k-space point, and its measured nearest neighbors

can be smaller than in normal GRAPPA patterns. The closest k-space points usually contribute most to the PI reconstruction, which thus improves the reconstruction quality. In the image domain, we can explain the benefit of 2D-CAIPIRINHA over 2D-GRAPPA by the fact that 2D-CAIPIRINHA patterns can result in fewer aliased voxels.

3.2.3 1D-CAIPIRINHA

The reconstruction of slice PI, such as 1D-CAIPIRINHA, is very similar to in-plane PI. Yet, there are three key differences: Firstly, not a single target point is measured in slice PI, since we measure the sum of slices and want to reconstruct the individual slices. The second difference is that all k-space points within a reconstruction kernel are source points, because all k-space points in the k_x-k_y-plane are measured. Thirdly, we need as many different weighting sets as the number of aliased slices times the number of channels is: For each slice we want to reconstruct, we need an own weighting set. These differences are illustrated in fig. 3.6. In order to better distinguish between the aliased k-space points of the different slices, we can apply different phases to the k-space points of the different slices. The phase is usually chosen to be linear in the phase-encoding directions. This can be achieved by modifying the phases of the excitation pulses depending on the phase-encoding point. In the image domain, we can explain the benefit of this additional linear phase by a shift of the slices with respect to the others, which, exactly like in 2D-CAIPIRINHA, minimizes the number of aliased voxels. This trick was introduced by Breuer et al. (46).

Another difference to in-plane PI methods is that the SNR does not decrease with the square-root of the acceleration factor R_{slice}, but only with the g-factor, when using slice PI in comparison to acquiring the slices sequentially:

$$SNR_{Slice} = \frac{SNR_{Full}}{g} \tag{3.6}$$

The reason for this is that we excite and therefore measure a larger volume in slice PI, very much like in Hadamard-encoded measurements, and each measurement always contains signal from the whole volume (46). And indeed, in comparison to Hadamard-encoded measurements, the SNR of slice PI decreases with the square-root of R, as we would expect. With other words, the SNR efficiency of course depends on the reference to which we compare our method, and usually sequential slice measurements are used for that. With that said, we can define two quality factors, one defining the sequential slice-encoding as the gold standard, and one defining the Hadamard-encoding (or a similar

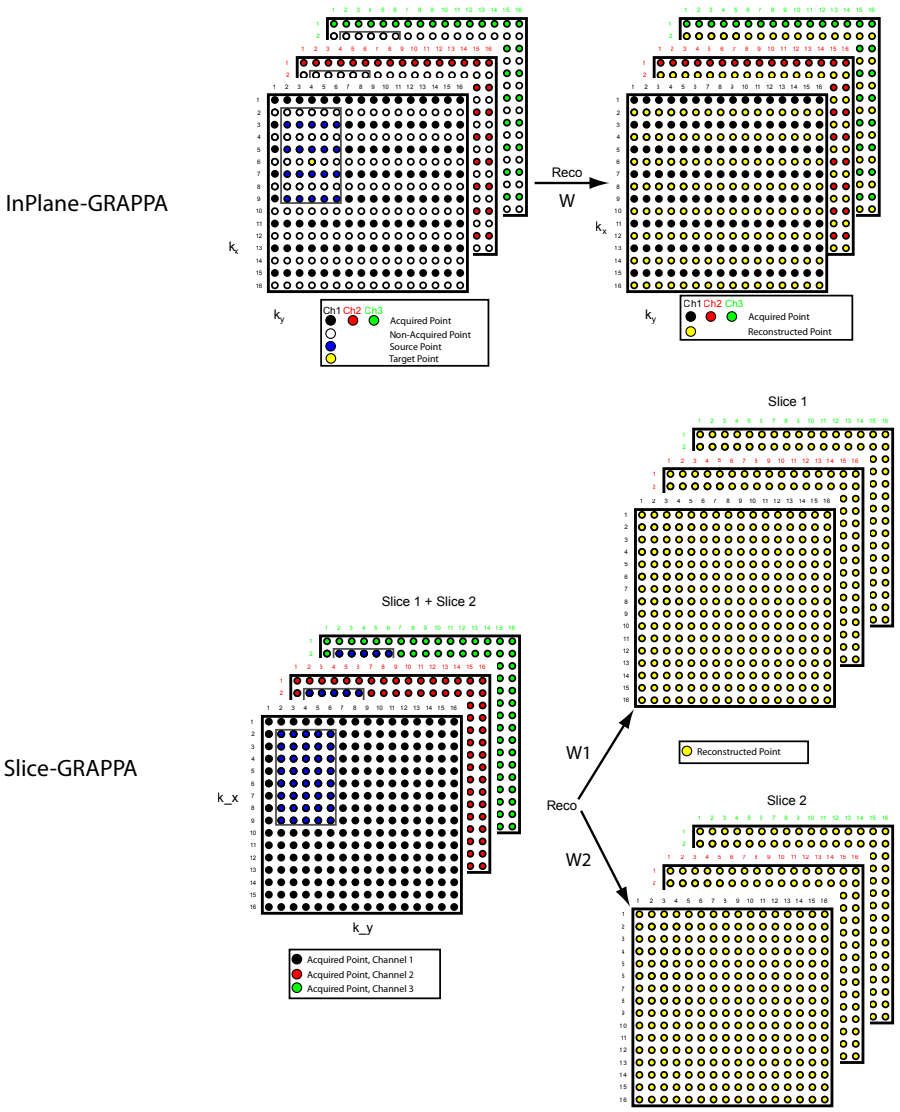

Figure 3.6: In in-plane PI, only some points were measured within the kernel and can thus be used for reconstruction. The unmodified, measured points are part of the final k-space. In slice PI the sum of the k-spaces of the individual slices are measured. All these points are used to reconstruct the missing points. In the final k-spaces, not a single originally measured point is present. Two different weighting sets (including all channels) are needed to reconstruct both slices, as indicated by "W1" and "W2".

SNR efficient encoding) as the gold standard. I decided for the latter, since Hadamard encoding can be performed easily in practice, and it appears more natural to me to define the gold standard as the most SNR efficient sequence which can be achieved practically. The quality factor of slice PI then results in

$$\Omega_{SlicePI}^{Total} = \Omega_{SlicePI}^{Others} = \frac{1}{g} \tag{3.7}$$

which is the same as for In-plane PI.

3.2.4 (2+1)D-CAIPIRINHA

(2+1)D-CAIPIRINHA is the combination of 2D-CAIPIRINHA and slice- or 1D-CAIPIRINHA. All three methods are illustrated in fig. 3.7. The reconstruction of 2D- and 1D-CAIPIRINHA can be performed independently, however the order of the two reconstructions influences the results.

Using (2+1)D-CAIPIRINHA instead of 2D-GRAPPA, 1D-CAIPIRINHA, or 2D-CAIPIRINHA alone has the advantage that the sensitivity differences between the AC channels are exploited in all three spatial dimensions, in contrast to only one (1D-CAIPIRINHA) or two (2D-GRAPPA, 2D-CAIPIRINHA). The magnitude of these variations significantly determines the quality of the PI reconstruction, and thus ultimately the total acceleration factor that can be used without severe artifacts. As an example, if all channels had the same spatial sensitivity, they would not contain any additional spatial information, and PI would not be possible. Therefore, (2+1)D-CAIPIRINHA should, in theory, provide better reconstruction results than the other three methods.

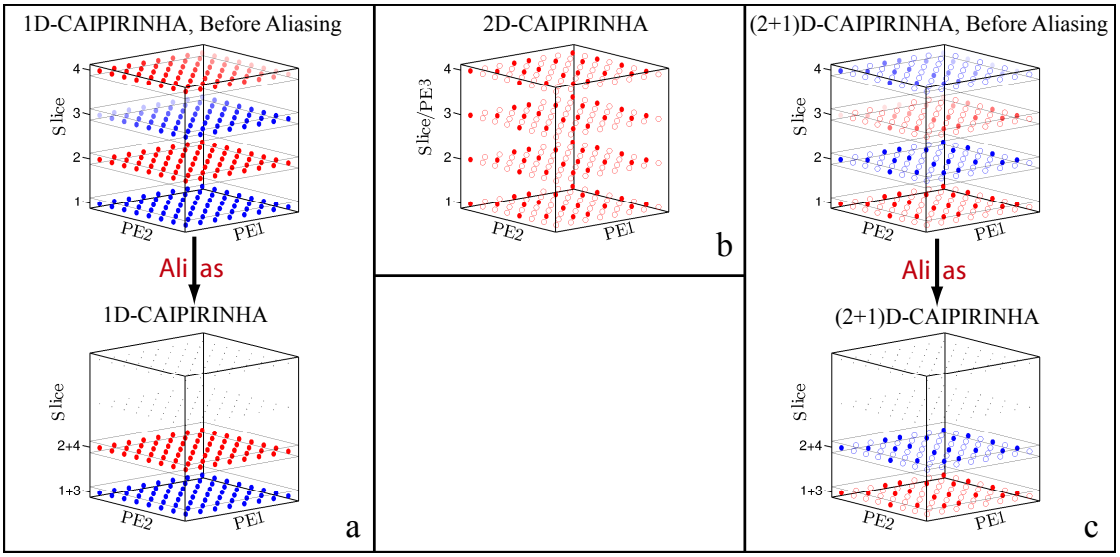

Figure 3.7: Comparison of 1D-CAIPIRINHA, 2D-CAIPIRINHA, and (2+1)D-CAIPIRINHA. (a) In 1D-CAIPIRINHA, slices 1 and 3 are excited, and all k-space points of those slices are measured. However, no method for differentiating between them is used, resulting in both slices to alias. The same is done for slices 2 and 4. The transparency of the k-space points represents a linear phase along the corresponding direction, causing an FoV-shift of that slice with respect to the others. (b) In 2D-CAIPIRINHA, k-space points are omitted using a certain under-sampling pattern. All four slices are measured independently (e.g. sequentially). (c) In (2+1)D-CAIPIRINHA, both methods are combined: The slices are measured with aliasing occurring in slices 1 and 3, and 2 and 4 as in (a), and additionally not all k-space points are measured for those aliased slices, resulting in additional in-plane aliasing. Adapted from: (42).

3.3 Methods

3.3.1 Reconstruction Algorithms

Two algorithms for simulating and reconstructing MRSI data accelerated with 2D- and 1D-CAIPIRINHA were written. The algorithms were similar as sketched in the Theory section. The 2D-CAIPIRINHA algorithm was implemented as follows:

1. Calculate the weights:
   a) Define the under-sampling pattern
   b) Choose one missing point in the under-sampling pattern as the target point group t
   c) Replicate the under-sampling pattern and concatenate the replicas. Find a kernel around the target point with a size big enough to include at least a predefined number of L measured points (source points)

d) Loop through all P unique possibilities for the kernel to be contained inside the ACS k-space. Gather all those source points in the matrix S with size $N \cdot L \times P$ and all target points in T with size $N \times P$, respectively. N is the number of channels.

e) Calculate the weights for the target point group t, W_t, and all N channels according to eq. (3.5)

f) Repeat steps (b)-(e) for all remaining target point groups

2. Apply the weights:

a) Choose one target point group t in the under-sampling pattern

b) Choose one occurence of such a point in the measured k-space (the under-sampling pattern is repeated several times to build up the whole, under-sampled k-space. Therefore, each target point occurs several times in the data, and the same weights W_t can be used for all of those)

c) Define the same kernel as in step 1 around the chosen target point

d) Reconstruct the target points of all channels according to eq. (3.4) by using the weights W_t

e) Repeat steps (b) - (d) for all occurrences of this target point group

f) Repeat steps (a) - (e) for all remaining target point groups

The 1D-CAIPIRINHA algorithm was implemented in a similar way:

1. Calculate the weights:

a) Sum the ACS slices with the same linear phases along the phase encoding directions as the MRSI data was measured with

b) Choose one target slice t

c) Define a kernel with a size big enough to include at least a predefined number of L measured points in the summed ACS k-space (source points)

d) Loop through all P unique possibilities for the kernel to be contained inside the ACS k-space. Gather all the source points from the summed ACS k-space in the matrix S with size $N \cdot L \times P$ and all target points from the non-summed ACS k-space of slice t in the matrix T with size $N \times P$, respectively. N are the number of channels.

e) Calculate the weights for slice t, W_t, and for all N channels according to eq. (3.5)

f) Repeat steps (b) - (e) for all remaining slices

2. Apply the weights:

a) Choose one target slice t

b) Choose one target point in this slice

c) Define the same kernel as in step 1 around the chosen target point

d) Reconstruct the target points of all channels according to eq. (3.4) by using the weighting set W_t

e) Repeat steps (b) - (d) for all remaining target points in slice t

f) Repeat steps (a) - (e) for all remaining slices

3.3.2 Simulations

Data Acquisition

Before (2+1)D-CAIPIRINHA was implemented into the sequence, the feasibility of the method was first tested in simulations, and compared to 2D-GRAPPA and 2D-CAIPIRINHA.

Therefore, seven healthy volunteers were measured on our Siemens 7T scanner (Magnetom, Siemens Healthcare, Erlangen, Germany) with a 32-channel head receive coil (Nova Medical, Wilmington, U.S.A.). A volume coil included in the same coil housing was used for signal transmission. Two data sets were excluded because of motion artifacts.

A 3D Magnetization-Prepared Two Rapid Acquisition Gradient Echoes (MP2RAGE) sequence was acquired for anatomical reference and for creating a brain mask (47). The TE was 2.96 ms, the TR 4.2 s, the first inversion time 0.85 s, and the second inversion time 3.4 s. A GRAPPA acceleration factor of 3 was used, and the matrix size was $256 \times 256 \times 160$ resulting in voxel sizes of $0.9 \times 0.9 \times 1.1\,\mathrm{mm}^3$.
Next, a pre-saturation turbo-Fast Low Angle Shot (FLASH) sequence (48, 49) was acquired to map the flip-angle in the MRSI slice. The reference voltage was adapted accordingly to achieve an average flip angle of 90°.
The MRSI data were acquired with the same sequence as in chapter 2 with a spectral bandwidth of 6 kHz, 2048 spectral points, WET water suppression (14), and an Ernst

flip angle of 45°. A matrix size of 64×64 was used with a FoV of $220 \times 220\,\mathrm{mm}^2$. Two slices with a thickness of 8 mm were acquired with pulse-cascaded Hadamard encoding (50), resulting in acquisition delays of 1.3 ms and 2.3 ms for the upper and lower slice, respectively.
A GRE imaging sequence of the same slices, and with the same parameters as the MRSI sequence, was measured to provide ACS data and for calculating the coil combination weights.

Finding Best Undersampling Patterns

The first step was to find the best patterns for 2D-GRAPPA, 2D-CAIPIRINHA and (2+1)D-CAIPIRINHA for different acceleration factors. Each (2+1)D-CAIPIRINHA pattern consisted of a 2D-CAIPIRINHA pattern, and the two FoV shifts (linear phases in k-space) in the x- and y-direction of the second slice with respect to the first.
The best 2D-GRAPPA patterns for a given total acceleration factor $2 \leq R_{Total} \leq 10$ were found in two steps. In step 1a, the Artifact Power (AP) was calculated for all possible patterns, and was defined as follows:

$$AP = 100 \cdot \frac{\sum_{i=1}^{N} \sum_{\vec{r} \in mask} \sum_{t \in T_{mask}} |S_{Accel}(i, \vec{r}, t) - S_{Full}(i, \vec{r}, t)|}{\sum_{i=1}^{N} \sum_{\vec{r} \in mask} \sum_{t \in T_{mask}} |S_{Full}(i, \vec{r}, t)|} \tag{3.8}$$

mask is the brain mask, T_{mask} is a mask in the time domain to minimize computational burden, S_{Accel} is the under-sampled and reconstructed MRSI data, and S_{Full} is the fully-sampled MRSI data. Patterns were considered as possible, if $R_x \cdot R_y \approx R_{Total}$, and $R_x, R_y \leq 5$, where R_x and R_y are the acceleration factors along the x- and y-direction, respectively. As an example, for $R_{Total} = 4$, three patterns are possible: $R_x = 1, R_y = 4$, $R_x = 4, R_y = 1$, and $R_x = 2, R_y = 2$. A so called Variable Density (VD)-radius up to 5 points, i.e. the radial distance to the k-space center, within which all k-space points are simulated to be measured, was used to achieve the intended R_{Total} as close as possible for patterns that would be excluded otherwise. Patterns which minimize AP were considered as the winners of this step.

In step 1b, the g-factors were calculated using a pseudo-replica method, see chapter 5. Patterns which minimized the g-factors inside the brain mask were considered winners

of step 1b.

The two patterns minimizing step 1a and 1b were further processed in step 2. In this step, the data were simulated to be under-sampled with the tested pattern, reconstructed with the algorithms described above, coil combined using MUSICAL, Hamming filtered, and fitted with LCModel. The Root Mean Square Error (RMSE) between the fitted concentrations of tNAA of the under-sampled and the fully sampled data was calculated according to eq. (3.9). The pattern minimizing the RMSE was defined as the best overall 2D-GRAPPA pattern.

$$RMSE = 100 \cdot \sqrt{\frac{\sum\limits_{\vec{r} \in mask} \left(\frac{C_{Accel}(\vec{r}) - C_{Full}(\vec{r})}{C_{Full}(\vec{r})} \right)^2}{M}} \tag{3.9}$$

The best 2D-CAIPIRINHA patterns were estimated the same way as the 2D-GRAPPA patterns, but one additional step was done before step 1. In step 0, all possible patterns were created by randomly placing j points (measured points) in a $k \times k$ matrix. j and k were chosen to fulfill $R_{Total} \approx k^2/j$. Several combinations of k and j are possible for a given R_{Total}. A VD-radius was again used to allow more patterns. The quality measure of this step was defined as the mean distance between a missing point and its three measured neighbors, since k-space points close to the missing point usually contribute most in the reconstruction of that point (43). The 20 patterns which minimized this measure were eligible for step 1. However, if more than 20 patterns yielded the same quality measure or if fewer than 20 were possible, all of these patterns were used for step 1. The process of step 0 is illustrated in fig. 3.8.

The best (2+1)D-CAIPIRINHA patterns were chosen the same as in the case of 2D-CAIPIRINHA, except that the best 20 patterns of step 0 were replicated 16 times, each replica with a different FoV shift $\in \{0, \frac{1}{6}, \frac{2}{6}, \frac{3}{6}\} \cdot FoV_x \times \{0, \frac{1}{6}, \frac{2}{6}, \frac{3}{6}\} \cdot FoV_y$. Furthermore, (2+1)D-CAIPIRINHA was only tested for $5 \leq R_{Total} \leq 10$, because the sensitivity variations in the x-y-plane of the used 32 channel coil are more than sufficient for $R < 5$.

The number of patterns of each step and for the different methods were compared. The g-factors and APs of step 1 were compared between the three methods.

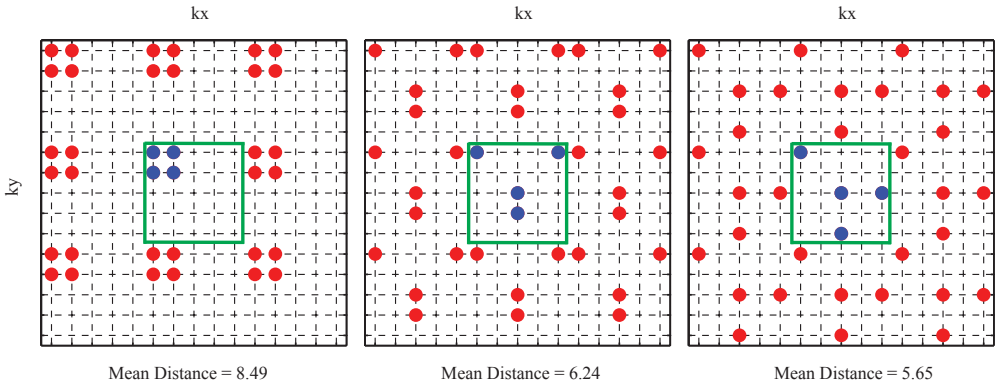

Figure 3.8: Illustration of step 0. Three different examples of under-sampling patterns are shown with their mean distance of the measured to the non-measured points. This quality measure selects patterns with evenly distributed target points as shown with these three patterns. The right-most pattern has the smallest mean distance, and the most homogeneous target point distribution. Reprinted from: (42).

Comparing Best Undersampling Patterns

Once the best under-sampling patterns were found in steps 0-2, they were compared between the three PI methods, 2D-GRAPPA, 2D-CAIPIRINHA, and (2+1)D-CAIPIRINHA using the RMSE of tNAA and the mean CRLB values of tCho and tCr. The APs, CRLBs, RMSEs and g-factors were further compared statistically between the three methods. Statistical significance was tested with the Wilcoxon signed rank test for the absolute error (i.e. same as RMSE without taking the mean over brain voxels) and the g-factors, while the AP and CRLB values were tested with the t-test. The statistical significance levels were chosen lower than usual for the CRLBs, absolute errors, and g-factors because the t- and Wilcoxon signed rank test assume independent measurements, but the values of the different voxels are not completely independent. Metabolic maps and spectra were compared visually.

Lipid Contamination

Parallel imaging usually results in remaining aliasing after the PI reconstruction. Although the remaining aliasing can be very small, the large lipid signals from the subcutaneous fat can still deteriorate the spectral quality, because the lipid signals are magnitudes higher than the metabolite signals. This is especially problematic if no lipid suppression method is used, as it was done in this work.
Therefore, the lipid signal increase was calculated by summing the absolute spectrum in

the range between 0.3 and 2.1 ppm, dividing the result from a reference, and computing the mean over all brain voxels and volunteers. This was performed for all three PI methods, and additionally after a lipid regularized reconstruction as proposed by Bilgic et al. (51) was done on all three methods. The regularization exploits the fact that lipid and metabolite signals are almost orthogonal in the spectral and spatial domains.
In both cases, with and without lipid regularization, the reference was defined as the lipid content when not simulating any PI ("fully sampled"), nor performing any lipid decontamination.

3.3.3 Implementing (2+1)D-CAIPIRINHA into MRSI Sequence

Three features, Hadamard encoding, 2D-CAIPIRINHA and 1D-CAIPIRINHA were implemented into the same MRSI sequence where the GRE pre-scan had been implemented. This sequence was tested in volunteers, and applied to measure MS patients. The latter is described in chapter 6.

Generalized Hadamard

Hadamard step	Signal sign slice 1	Signal sign slice 2
HadaStep1	+1	+1
HadaStep2	+1	-1
HadaStep1 + HadaStep2	2	0
HadaStep1 - HadaStep2	0	2

Table 3.1: Example of how Hadamard encoding (second and third row) and Hadamard decoding (last two rows) works for two slices. In the first Hadamard encoding step, both slices are excited with the same phase. In the second step, slice 1 is excited normally, while the signal of slice 2 is inverted (-1). Summing both Hadamard encoding steps results in the signal of slice 1 only, but with twice the normal signal intensity, and thus more SNR in comparison to consecutive measurement of the slices. Subtracting Hadamard encoding step 2 from step 1 results in signal from slice 2 only.

My colleague Gilbert Hangel implemented Hadamard encoding for exactly four slices into the MRSI sequence. Hadamard encoding is a method which provides the same high SNR/t as 3D-sequences, without the drawback of a miserable PSF due to only few phase encoding steps, e.g. 4 or 8. This high SNR/t is achieved by always exciting all slices, but with phases of the slices following a Hadamard matrix, where +1 of the matrix represents phase 0°, and -1 represents phase 180°. A phase of 180° is equivalent to inverting all signals. An example for two slices is given in table 3.1. From this table, it is clear that

the signal of the individual slices can be reconstructed by summing or subtracting the signal of the different Hadamard steps. In general, the Hadamard decoding is performed by multiplying the signal of the Hadamard steps with the inverse Hadamard matrix of the same size.

Hadamard encoding can be combined with 1D-CAIPIRINHA, since Hadamard encoding adds a constant phase to all phase encoding steps, but varying between Hadamard encoding steps and slices, while 1D-CAIPIRINHA adds a linear phase along the phase-encoding directions. This was done in the sequence.
Since Hadamard encoding provides a high SNR efficiency, it was combined with 2D- and 1D-CAIPIRINHA. Therefore, it had to be generalized from the fixed four slices to the possibilities of 1, 2, 4, or 8 slices.

2D-CAIPIRINHA

2D-CAIPIRINHA was implemented into the MRSI sequence of our 7T Siemens scanner with the software version VB17. The user can specify the in-plane acceleration factor in the so called "Special Card" of the sequence. Depending on this acceleration factor, GRAPPA acceleration patterns and five 2D-CAIPIRINHA patterns are available in a Graphical User Interface (GUI) field. For example, for an in-plane acceleration of 4, the GRAPPA patterns 4×1, 1×4, 2×2 and the five 2D-CAIPIRINHA patterns are available, see fig. 3.9 a. The 2D-CAIPIRINHA patterns can be specified by the user via files. For each integer in-plane acceleration factor, one file is available. In these files, the 2D-CAIPIRINHA under-sampling patterns can be specified by entering 0s (these k-space points will not be measured), and 1s (these will be measured). One such file is shown in fig. 3.9 b. With this approach, the under-sampling is very flexible. However, it is also prone to errors, e.g. if the user enters non-valid patterns, or if a pattern provides an acceleration different as specified by the file name.
In case if a 2D-CAIPIRINHA pattern is chosen, the correct file is read in by the sequence. If a GRAPPA pattern is chosen, it is defined directly in the code of the sequence. In both cases, an under-sampling pattern is then available in the sequence, which is replicated to the intended matrix size. The number of averages of those k-space points where the under-sampling pattern stores a "0", are set to 0, while the others are not changed. As a result those points will be omitted.
The third field in the special card is the VD-radius. This parameter specifies the radial distance to the k-space center, within which all k-space points will be measured. This is useful to better achieve the intended measurement time and to slightly mitigate the

aliasing, since the k-space center contains most spatial information, and not under-sampling it results in mainly high-frequency and low-intensity aliasing.

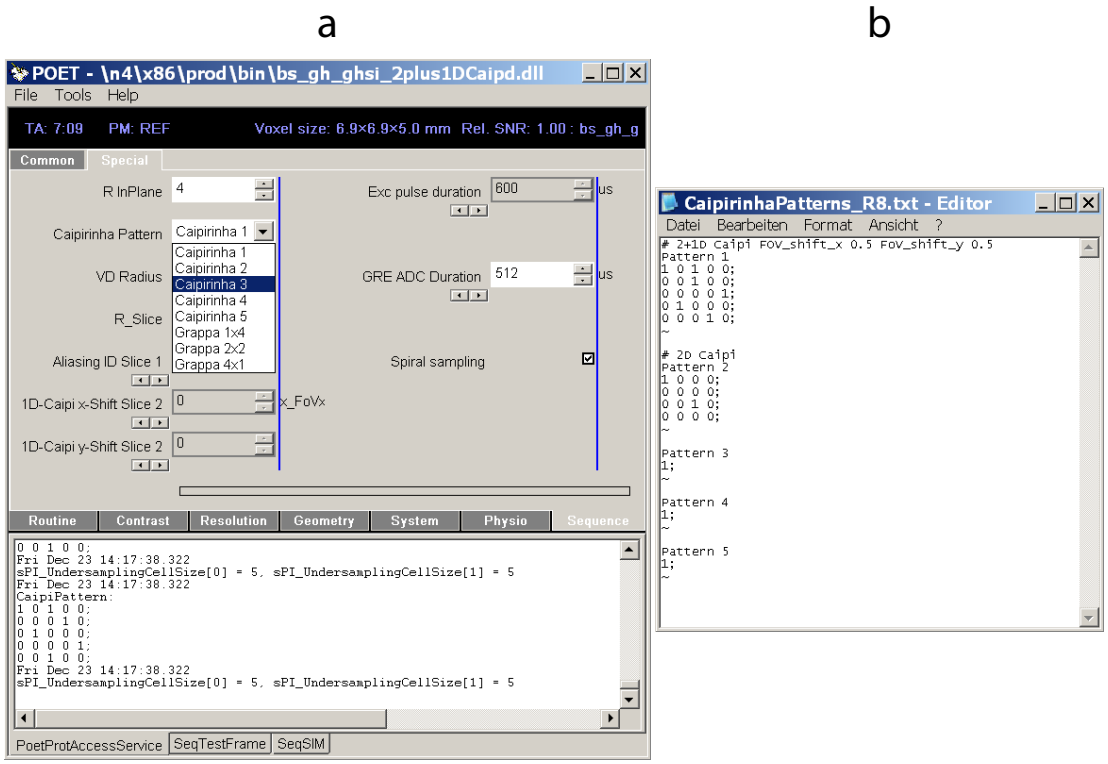

Figure 3.9: a: This figure shows how 2D-CAIPIRINHA was implemented into the sequence GUI. The user can choose the in-plane acceleration factor ("R InPlane"), the under-sampling patterns (in this case "Caipirinha 1-5", "Grappa 1×4", "Grappa 2×2" and "Grappa 4×1"), and the "VD-Radius". b: One sample ASCII-file for $R_{Total} = 8$ showing different 2D-CAIPIRINHA patterns. The patterns can easily be modified by the user by changing these files. The last three patterns are not used, and are therefore set to containing only 1's. The file with the used acceleration factor is read in by the sequence, and the measurement k-space is under-sampled according to the desired 2D-CAIPIRINHA pattern written in the file.

1D-CAIPIRINHA

I also implemented 1D-CAIPIRINHA into the same MRSI sequence. In the special card of the sequence, four parameters were inserted to control 1D-CAIPIRINHA. With the first, "R_Slice" the user can specify the slice acceleration factor. Only if $R\_Slice > 1$, the other fields have an effect. With the second, "Aliasing ID Slice [1-8]", the user can specify which slices should be aliased. The slices are counted from the lowest to the highest. Slices with the same ID will be aliased. E.g. if slices 1 and 3, and 2

and 4 should be aliased, the user can enter the aliasing IDs "1 2 1 2". The next two parameters, "1D-CAIPIA [x/y]-Shift Slice [2-8]" controls how much, in multiples of the FoV, the slices should be shifted with respect to the first slice in x- and y-direction.
When the sequence is run, the FoV-shift is applied to the slices by adding a phase to the RF pulses corresponding to the different slices. This phase changes linearly with the x- and y- phase encoding direction, according to the fields "1D-CAIPIA [x/y]-Shift Slice [2-8]". Hadamard encoding is then performed on the slice groups. E.g. if slices 1 and 3 are aliased by 1D-CAIPIRINHA, and thus form slice group 1, and slices 2 and 4 are aliased to slice group 2, only a Hadamard matrix of size 2×2 is used, although there are four slices. Therefore, with Hadamard decoding, we can differentiate between slice group 1 (slice1+slice3), and slice group 2 (slice2+slice4), but not between slice 1 and slice 3, nor slice 2 and slice 4.

Data Acquisition

One volunteer was measured the same as described above, but the PI was not simulated in post-processing. Instead, the data was **actually** under-sampled during the measurement with $R_{Total} = 8$ resulting in a measurement time of 15 minutes. Furthermore, four slices were measured instead of only 2. It was processed the same way as the other measurements. The resulting metabolic maps were examined qualitatively.

R_{Total}	PI Method	Step 0	Step 1	Step 2
2	2D-GRAPPA	2	2	2
2	2D-CAIPI	6438	6	2
2	(2+1)D-CAIPI	0	0	0
5	2D-GRAPPA	2	2	2
5	2D-CAIPI	$1.1 \cdot 10^5$	17	2
5	(2+1)D-CAIPI	$1.3 \cdot 10^6$	576	2
9	2D-GRAPPA	1	1	1
9	2D-CAIPI	$6.8 \cdot 10^7$	54	2
9	(2+1)D-CAIPI	$6.7 \cdot 10^6$	400	2

Table 3.2: Number of processed patterns for three different acceleration factors and steps 0-2. In step 0, an enormous amount of patterns had to be processed for some acceleration factors. Adapted from: (42).

3.4 Results

3.4.1 Simulations

Finding Best Undersampling Patterns

The number of patterns in each step for all PI methods and $R_{Total} = 2, 5, 9$ are listed in table 3.2. For some methods, a tremendous amount of patterns had to be processed. The g-factors and APs of step 1 are shown in fig. 3.10a and b. (2+1)D-CAIPIRINHA provides better APs and g-factors for all acceleration factors, except for $R_{Total} = 9$, where all methods virtually provide the same g-factors. 2D-GRAPPA consistently results in higher APs and g-factors. Similar results were obtained by Breuer et al., who compared conventional 2D-SENSE, which is similar to 2D-GRAPPA, with 2D-CAIPIRINHA (45).

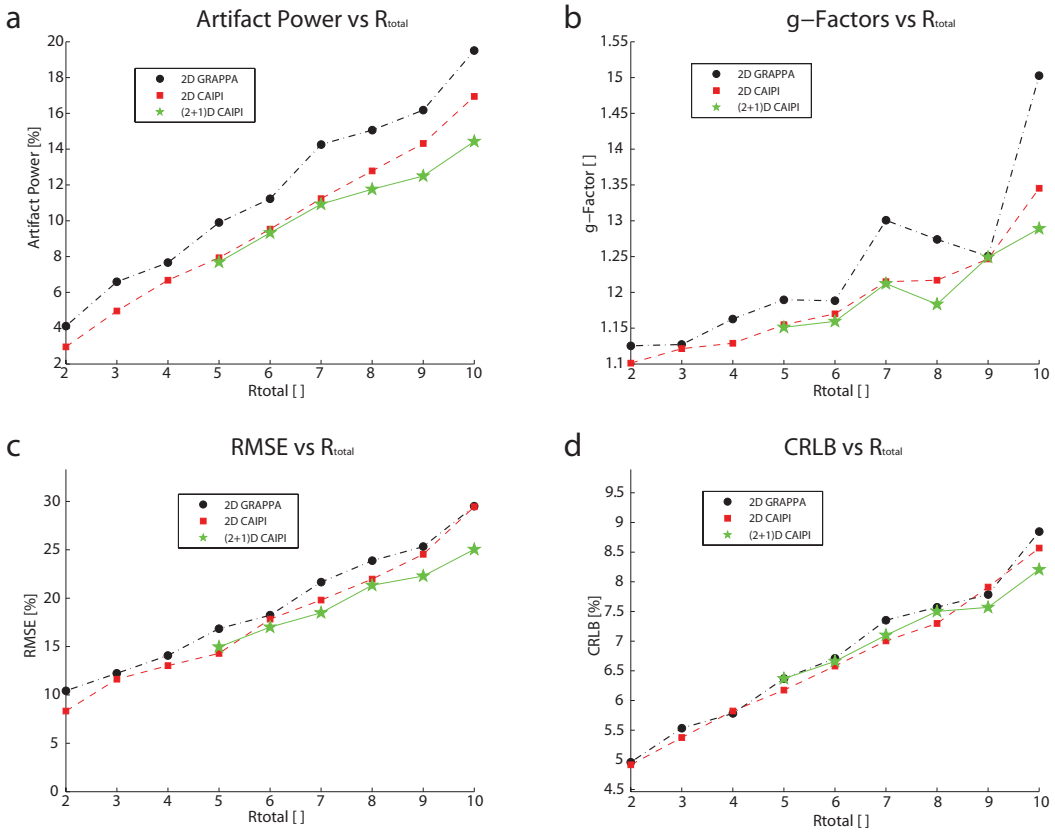

Figure 3.10: Artifact power, g-factor, RMSE, and CRLB values for different acceleration factors R_{Total}. The first two are the values of the best pattern of step 1. All of these quality measures show a trend of increasing with R_{Total}. In most cases, (2+1)D-CAIPIRINHA provides the lowest quality measure (best reconstruction quality), and 2D-GRAPPA the highest. Reprinted from: (42).

Comparing Best Undersampling Patterns

The RMSE and CRLB values are plotted in fig. 3.10c and d, respectively. Again, (2+1)D-CAIPIRINHA results in lower RMSE values, except for $R_{Total} = 5$. 2D-GRAPPA results in higher RMSE values in comparison to 2D-CAIPIRINHA. (2+1)D-CAIPIRINHA only provides lower CRLB for $R_{Total} = 9, 10$.
A statistical comparison between the AP, g-factor, absolute error, and CRLB values for the different methods is given in table 3.3. Bold figures indicate values where (2+1)D-CAIPIRINHA yields lower values than the corresponding method, while * means a statistical significance of $p < 5 \cdot 10^{-2}$ for the AP, and $p < 5 \cdot 10^{-3}$ for the others, and ** means $p < 5 \cdot 10^{-4}$ when tested against the values of (2+1)D-CAIPIRINHA. The AP gives one value for all brain voxels, and thus the compared values are statistically independent measures.

	PI Method	$R = 5$	$R = 6$	$R = 7$	$R = 8$	$R = 9$	$R = 10$
AP [%]	2D-GRAPPA	**8.86***	**9.89**	**12.54***	**13.22***	**14.18**	**17.94**
	2D-CAIPI	6.97	8.42	**9.86**	**11.56**	**13.51**	**15.14***
	(2+1)D-C	6.68	8.47	9.63	10.31	11.13	13.06
g-Factor	2D-GRAPPA	1.10**	**1.10****	**1.18****	**1.16****	1.14**	**1.30****
	2D-CAIPI	1.08**	**1.11****	1.12**	1.12**	1.14	**1.21****
	(2+1)D-C	1.10	1.08	1.12	1.17	1.14	1.15
Absolute [%] Error	2D-GRAPPA	**6.0****	**7.3****	**8.2****	**8.8****	**9.5****	**11.7****
	2D-CAIPI	5.7	**6.9****	**8.0****	**8.7****	**9.5****	**11.3****
	(2+1)D-C	5.9	6.5	7.2	8.4	8.5	10.0
CRLB [%]	2D-GRAPPA	6.37	**6.71**	**7.35****	**7.57**	**7.78****	**8.85****
	2D-CAIPI	6.18**	6.58	7.01	7.30**	**7.91****	**8.57****
	(2+1)D-C	6.37	6.66	7.10	7.50	7.57	8.21

Table 3.3: Comparison of the AP, g-factor, absolute error, and CRLB values for the best patterns of step 2. The values of 2D-GRAPPA and 2D-CAIPIRINHA were statistically compared against the value of (2+1)D-CAIPIRINHA. Statistical significance is denoted with *, while highly significant values are denoted with **, and bold values represent those where (2+1)D-CAIPIRINHA performs better than the considered method. Reprinted from: (42).

Maps of tNAA, tCho, tCr and RMSE of both slices for one volunteer and $R_{Total} = 7$ are shown in fig. 3.11. The metabolic maps of (2+1)D-CAIPIRINHA look more similar to the reference with $R_{Total} = 1$ for the upper slice, and comparable to the other methods for slice 2. The RMSE map of (2+1)D-CAIPIRINHA shows smaller deviations from the reference for the upper slice in comparison to 2D-GRAPPA and 2D-CAIPIRINHA, but

has a spot with higher RMSE values in slice 2.
A comparison between sample spectra resulting from LCModel fitting between not simulating any PI ("Full"), and the three different PI methods is shown in fig. 3.12 for the same volunteer shown in fig. 3.11. In those examples, 2D-GRAPPA and 2D-CAIPIRINHA partially result in artifactual spectra. The spectra of (2+1)D-CAIPIRINHA, on the other hand, are more similar to the reference spectra.

Lipid Contamination

The lipid contamination ratio to the reference of $R_{Total} = 1$ is provided before and after lipid decontamination in table 3.4 for the different acceleration methods and acceleration factors. Lipid decontamination reduces the lipid artifacts below the values of $R_{Total} = 1$ without lipid decontamination (values smaller than 100 %). The lipid contamination values before performing a decontamination are lower for (2+1)D-CAIPIRINHA than for 2D-GRAPPA, and lower than for 2D-CAIPIRINHA in the case of $R > 7$. This reflects the fact that (2+1)D-CAIPIRINHA tends to result in better reconstructions, especially for high acceleration factors.
An example for the potential of the lipid decontamination algorithm is shown in fig. 3.13, where 2D-GRAPPA with $R_{Total} = 10$ results in severe lipid artifacts in tNAA maps. After applying the regularized reconstruction, the lipid artifacts are almost completely removed, resulting in quite good tNAA maps.

	Without Lipid Decontamination			With Lipid Decontamination		
R	2D-G [%]	2D-C [%]	(2+1)D-C [%]	2D-G [%]	2D-C [%]	(2+1)D-C [%]
2	98.9	101.0	—	60.2	59.8	—
3	107.7	105.0	—	61.1	60.6	—
4	109.1	113.4	—	62.0	61.8	—
5	125.0	116.9	122.7	63.2	63.1	61.7
6	136.7	126.6	131.7	65.1	65.0	58.6
7	143.8	133.2	138.2	65.9	66.0	63.3
8	151.5	160.0	149.7	67.3	67.1	72.1
9	163.4	170.3	147.6	69.9	69.3	72.2
10	192.0	198.2	180.4	71.9	72.0	77.6

Table 3.4: Lipid contamination ratio relative to the reference with $R_{Total} = 1$ with and without lipid decontamination (i.e. regularized reconstruction), for different acceleration factors and different PI methods. All values are below 100 % when lipid decontamination is used. Such lipid levels are usually manageable, as long as no strong lipid hot-spots occur. Reprinted from: (42).

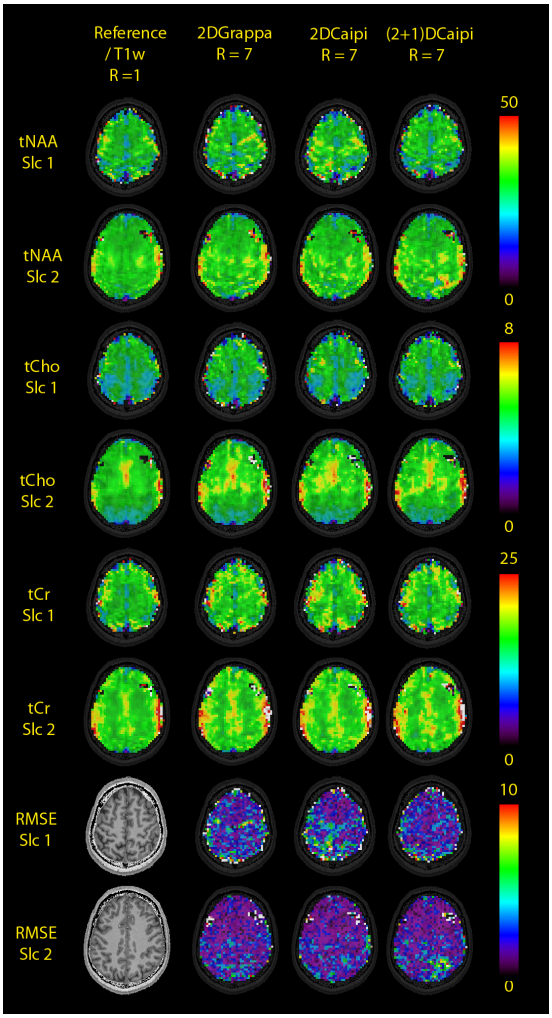

Figure 3.11: Metabolic maps of tNAA, tCho, and tCr, and the absolute error maps ("RMSE") for both slices of one volunteer and for the reference, $R_{Total} = 1$, and the three PI methods with $R_{Total} = 7$. The upper slice is very well reconstructed by (2+1)D-CAIPIRINHA, since it resembles very well the reference map. The (2+1)D-CAIPIRINHA reconstruction of the lower slice has a higher hotspot in the absolute error map than the other two methods. Adapted from: (42).

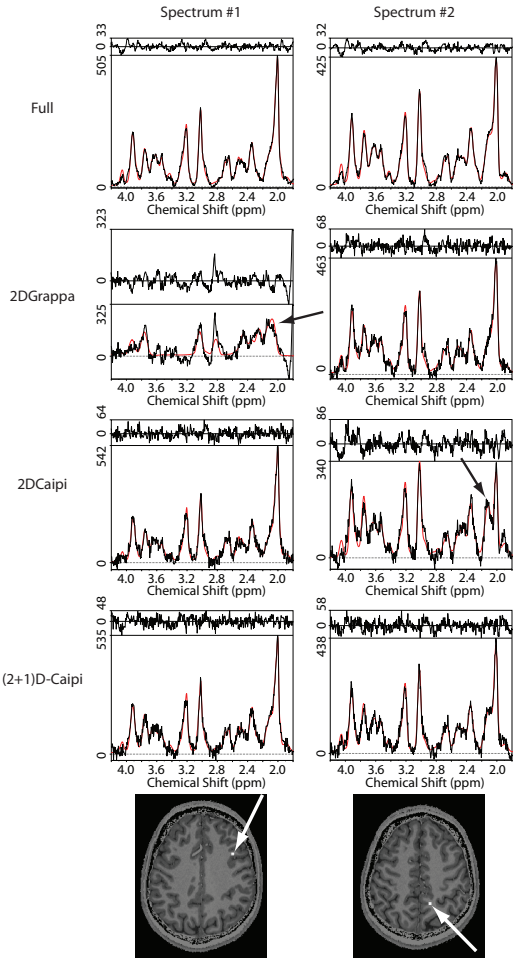

Figure 3.12: Two sample spectra of the same volunteer from fig. 3.11 for the reference ($R_{Total} = 1$), and the three PI methods. The voxel positions are shown on T_1-weighted images (white squares) in the native resolution and stressed by white arrows. Black arrows in the 2D-GRAPPA and 2D-CAIPIRINHA spectra indicate artifacts. All spectra were fitted with LCModel. The red lines represent the LCModel fit, the black lines the input spectra, and above the fit, the residuum is plotted. Reprinted from: (42).

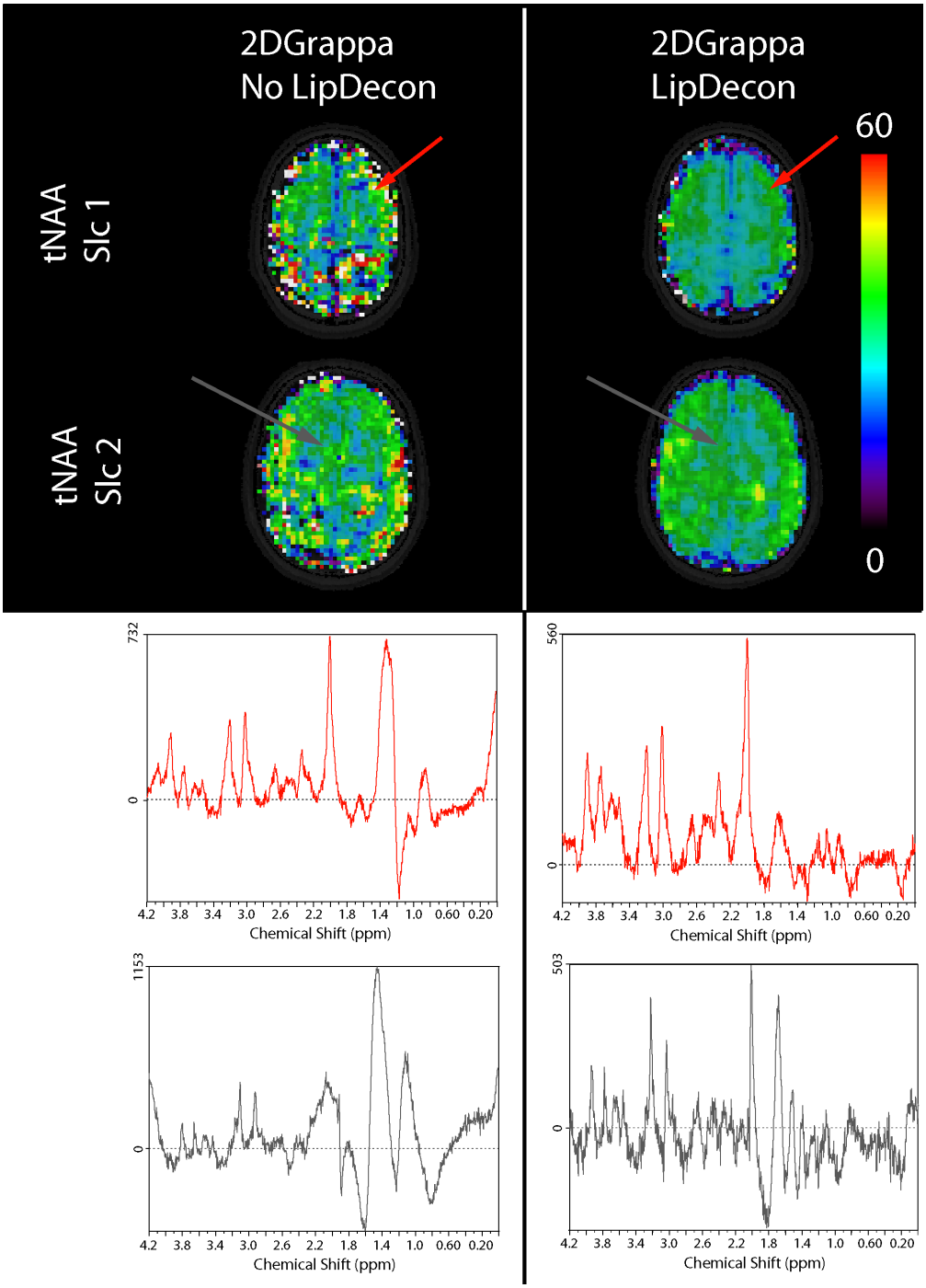

Figure 3.13: Left: Sample tNAA maps which are strongly altered by lipids due to the usage of 2D-GRAPPA and a high acceleration factor of $R_{Total} = 10$. After applying lipid decontamination (right), the tNAA maps look almost normal. Below, two spectra from the positions indicated by red and gray arrows, are shown. The decontaminated spectra show strongly reduced lipid signals, although the gray spectrum still has high lipid signals. Reprinted from: (42).

3.4.2 Implementing (2+1)D-CAIPIRINHA into MRSI Sequence

Metabolic maps of tNAA, tCho, tCr, Ins, and Glx are shown in fig. 3.14 for the volunteer which was measured with (2+1)D-CAIPIRINHA. The metabolic map quality is excellent, showing only small artifacts in the lowest slice which may be attributed to residual lipids. However, at such low positions, artifacts often occur in MRSI due to the proximity to the frontal sinus associated with strong B_0-inhomogeneities.

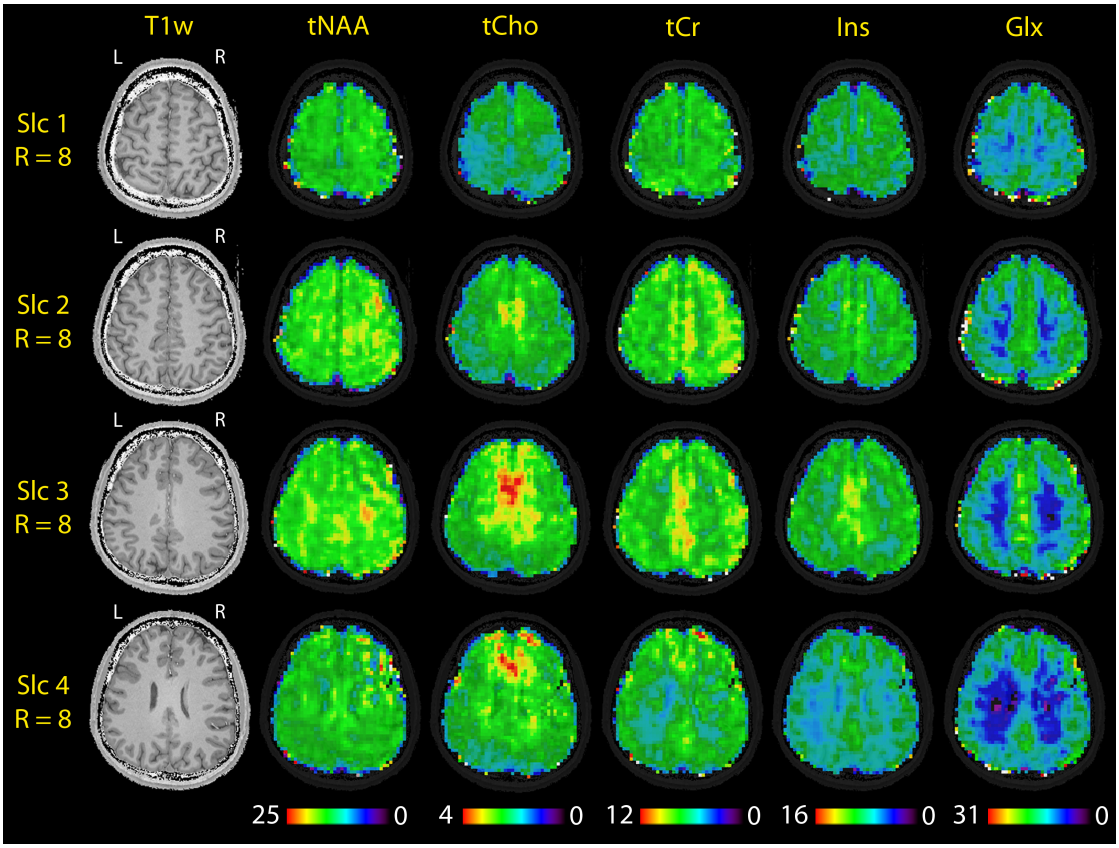

Figure 3.14: Sample metabolic maps comprising tNAA, tCho, tCr, Ins, and Glx of four slices from a volunteer measured with (2+1)D-CAIPIRINHA. The acceleration factor was $R_{Total} = 8$ resulting in a measurement time of 15 minutes. All metabolic maps have a high quality, with only minor artifacts occurring in the lowest slice. Even Ins and Glx could be reliably quantified. Reprinted from: (42).

3.5 Discussion

3.5.1 Simulations

Finding & Comparing Best Undersampling Patterns

The artifact power, g-factor, RMSE and CRLB values mostly follow the expected pattern: All values increase with higher accelerations, and are smallest for (2+1)D-CAIPIRINHA, and highest for 2D-GRAPPA. This is expected, because the reconstruction quality decreases with higher acceleration factors, as the system of linear equations in eq. (3.5) for calculating the weights is less over-determined, and therefore more prone to errors. The reason why the system of equations is less over-determined is due to the fact that fewer repetitions of the kernel in the ACS matrix are possible for high accelerations, because the kernel has to be larger to comprise a given number of source points, L.
Although this trend is visible, the CRLB values and the g-factors did not completely follow the pattern. For the CRLB values, this fact is not surprising, since small changes in the input data can have a big influence in the fitting results of LCModel, and thus on the CRLB values. The g-factors should in theory follow the trend more precisely, however. Yet, the VD-radius influences the SNR efficiency. Measuring a k-space density which does not match the target k-space density decreases the SNR efficiency (52), and with it the g-factor, as the g-factor is the ratio of the given SNR to a fixed SNR with a uniform k-space density (i.e. when not using any acceleration). When calculating the g-factor, the Hamming filter was not yet applied, and thus, the target density was a uniform one. As a result, increasing VD-radii decreased the g-factors. This is especially visible in the 2D-GRAPPA g-factors for $R_{Total} = 7, 8, 9$, which all result from a 3×3 GRAPPA pattern with different VD-radii to achieve the intended acceleration factors.

Lipid Contamination

Lipid decontamination worked quite well with the method of Bilgic et al. The lipid contamination ratios dropped from almost 200 % to about 70-80 % relative to using no PI and no lipid decontamination. Since lipids are mostly not a big issue if resolutions of $3.4 \times 3.4\,\mathrm{mm}^2$ are used in combination with a Hamming filter (24), lipid ratios below 100 % can be seen as manageable, as long as no strong lipid hot spots occur. The quite small lipid contamination decrease from 200 % to 70 % can be explained by the definition of the lipid contamination measure as summing a large spectral range of 0.3 to 2.1 ppm. Within this range, tNAA and macromolecules are included, and thus contribute to the lipid contamination measure as a baseline. As a result, even for perfect lipid decontamination,

the used measure would not be 0 %. On the other hand, lipids superimposing tNAA are taken into account by this definition. Thus, the lipid decrease is less strong in comparison to Bilgic et al., who obtained lipid reduction factors of about 9.5.

3.5.2 Implementing (2+1)D-CAIPIRINHA into MRSI Sequence

The measurement of one volunteer with four slices and an acceleration factor $R_{Total} = 8$ showed that (2+1)D-CAIPIRINHA not only performs well in simulations, but also works in actual measurements. The resulting metabolic maps were of very high quality, with even Ins and Glx being fitted reliably.

3.5.3 Comparison to Literature

In all studies in which MRSI was accelerated with PI, the acceleration was performed either along two spatial dimensions (26, 28–33, 35–37), or even only along one dimension (25, 27, 34, 38–41). To my knowledge, (42) is the first work accelerating MRSI in all three spatial dimensions with PI. In conventional MRI, an acceleration along all three dimensions was achieved by Breuer et al. (53) and Bilgic et al. (54). However, both approaches include non-Cartesian trajectories, similar to SSE trajectories in MRSI.
SENSE with its "strong approach" was used in many studies (25–35), although this approach can lead to artifacts when applied to low-resolution data. These artifacts can be avoided, however, at the expense of a more complicated reconstruction algorithm (30).
In other studies, the GRAPPA weights were calculated from MRSI k-space points in the k-space center (36, 40, 41), although there is no evidence that the GRAPPA-weights depend on spectral time points. This results in very small possible acceleration factors, and very small ACS matrix sizes, which is disadvantageous for the PI reconstruction.

In this work, on the other hand, three spatial dimensions were used for PI acceleration, a GRAPPA-based reconstruction was performed, avoiding the problems of the SENSE reconstructions, and ACS data based on the imaging pre-scan data were used. These pre-scans had to be measured anyway for coil combination, had a high matrix size of 128×128, which is even higher than the MRSI data themselves, and take only a few seconds measurement time.

3.5.4 Limitations & Outlook

It is important to stress that the found best acceleration patterns are specific for the used coil and field strength. They cannot be generalized for other systems, but can only

aid as a starting point. Thus, it is not possible to take the best patterns found in this work, use it with another coil or field strength, and expect them to be the best patterns also in this situation.
One drawback of PI is the lipid problems caused by residual aliasing, and thus the need to specifically deal with the lipids, e.g. with a regularized reconstruction.
Moreover, the acceleration factor in PI is theoretically limited to $R_{Total} \leq N$, where N is the number of AC channels. In practice, however it is limited to $R_{Total} \lesssim 10$, which therefore restricts its applications to 2D-encoding, and 2D-encoding with 1-8 slices, when combined with matrix sizes $\geq 64 \times 64$. The fact that each slice group has a different acquisition delay due to the pulse-cascaded Hadamard encoding is a distinct limitation, but could be mitigated by using Power Independent of Number of Slices (PINS) pulses (55).

These drawbacks are not present in SSE. Therefore, SSE was tested in the next step, see chapter 4.

4 Accelerated MRSI via Spatio-Spectral Encoding

4.1 Motivation

As already motivated in chapter 3, a means to accelerate MRSI is needed, if larger matrix sizes of about 64×64 are used. PI can provide acceleration factors of up to 10 with standard array coils consisting of e.g. 32 channels. If 3D-encoding with matrix sizes of about $50 \times 50 \times 50$, or more than 8 slices with a matrix size of 64×64 are demanded, the acceleration factor has to be at least 20-40 to achieve clinically reasonable measurement times. Such high acceleration factors cannot be realized with PI, but can be achieved with SSE, and even more so with the combination of both methods. Another advantage of SSE in comparison to PI is that lipid signals are less of a concern, as no aliasing occurs in SSE.

Several trajectories were used in SSE, such as an Echo Planar Imaging (EPI) based trajectory, termed Echo Planar Spectroscopic Imaging (EPSI) or Proton-EPSI (PEPSI) (56–59), spiral trajectories (60, 61), rosette trajectories (62), or concentric circle trajectories (5, 63). These trajectories have different advantages and disadvantages like different quality factors due to k-space densities, $\Omega_{Density}$, and due to gradient rewinders, Ω_{AcqEff}.

To overcome the problems of PI in MRSI, SSE was tested and implemented in the form of spiral encoding (only tested and small changes in the source code) (64, 65), and CONCEPT (implemented and tested) (5, 63) on the Siemens 7T Magnetom scanner. The implementation of CONCEPT into the sequence was done together with my colleague Lukas Hingerl. The whole CONCEPT reconstruction was implemented by him.

The work desccribed in this chapter has not been published yet, but will be presented at the annual meeting of the International Society for Magnetic Resonance in Medicine

(ISMRM) 2017 in Hawaii. It is still under development, as still some baseline problems occur due to an unknown reason, but preliminary results are shown in this chapter.

4.2 Theory

SSE accelerates sequences by measuring several k-space points within one spectral dwell time. The paths along which we traverse in k-space are called k-space trajectories. In most cases, several k-space trajectories (sometimes called spatial interleaves) are necessary to cover the whole k-space which is intended to be measured. However, these trajectories are usually very similar to each other, and are therefore often called "**the** k-space trajectory", and thereby meaning in fact the whole set of very similar trajectories. Since we need to measure each k-space point repetitively, these trajectories have to be closed curves, a distinct difference to conventional MRI. If the trajectory is not naturally closed, a so called "gradient rewinder" has to be played out to get back to the k-space starting point, and thereby closing the trajectory artificially. These rewinder data are usually not useful, and therefore the SNR efficiency drops for long gradient rewinders. The trajectory defines or influences a lot of important characteristics of the corresponding SSE sequence, such as the quality factor Ω, the maximum achievable resolution and spectral bandwidth, the caused Maxwell fields and Eddy current artifacts.

One concept common to all SSE trajectories is temporal interleaving, which is a method for having more time to complete one spatial interleaf, and therefore increasing the quality factor or even making the trajectory possible altogether. Instead of repeating the trajectory within the temporal duration $dT_{spectral}$, we repeat it with $nTI \cdot dT_{spectral}$, with $nTI \in \mathbb{N}$ being the temporal interleaf number. By measuring only every nTI'th time point, we reduce the spectral bandwidth from $BW_{spectral} = \frac{1}{dT_{spectral}}$ to $BW_{spectral,nTI} = \frac{1}{nTI \cdot dT_{spectral}} = \frac{BW_{spectral}}{nTI}$. To obtain spectra with the full bandwidth again, we measure all the missed time points in another nTI-1 repetitions by measuring exactly the same as in the first repetition, but time shifted. However, temporal interleaving has some drawbacks: Since no excitation can be exactly the same (e.g. small movements, small variations in the RF excitation, small variations in the water suppression etc.), only every N'th time points are fitting perfectly to each other. For example, if $nTI = 2$, every second time point will be slightly different, which corresponds to the highest representable frequency. Thus an additional signal occurs at the highest frequency. With $nTI > 2$, even more artifact signals occur, specifically nTI-1. Because of these artifacts,

only temporal interleaves of 2 and 3 are considered here.

The quality factor of SSE sequences simplifies to the ratio of the useful trajectory time to the total trajectory time, Ω_{AcqEff}, and the difference of the local density function of the k-space trajectory to the target k-space density, $\Omega_{Density}$.

Following is a small overview of different proposed SSE methods with a short discussion of their advantages and disadvantages.

4.2.1 EPSI

In EPSI, one k-space line is measured repetitively by going back and forth within one TR. The k-space lines are parallel to each other, thereby lying on an equidistant, rectilinear grid, often called Cartesian k-space. The gradient scheme of an EPSI sequence is given in fig. 4.1 a. If we do not use the data from the gradient ramps, resulting in $\Omega^{Density} = 1$ by definition, the EPSI quality factor can be calculated as follows:

Consider the sequence diagram as depicted in fig. 4.2. Let S_{max} be the maximum slew rate with which we ramp the x-gradient up and down, T_{Ramp} the time we need to ramp up from $G_x = 0$ to $G_x = G_A$. The acquisition happens during the time T_{Acq} while the gradient is constant. The time between measuring the same k-space locations in the same direction is $dT_{Spectral} = 4T_{Ramp} + 2T_{Acq}$. Therefore the spectral bandwidth with nTI temporal interleaves is given by:

$$BW_{Spectral} = \frac{nTI}{4T_{Ramp} + 2T_{Acq}} \tag{4.1}$$

Higher spectral bandwidths might be achieved with more complicated reconstruction schemes by considering that each k-space point is in fact traversed three times within $dT_{Spectral}$, but once in opposite direction, and with different temporal spacings for different k-space points. Due to the complex reconstruction, this is not considered here.
After ramping up, we keep the gradient constant. The area of this gradient (= integral), also called Gradient Moment (GM), is the k-space extent we need to measure for achieving a certain FoV. The relation between those is $GM = \frac{N_x}{\gamma FoV}$, where N_x is the desired number of voxels ("matrix size") in x-direction. GM can also be calculated as the area of the gradient during which it is constant, which results in

$$GM = \frac{N_x}{\gamma FoV} = G_A T_{Acq} = S_{max} T_{Ramp} \cdot T_{Acq} \tag{4.2}$$

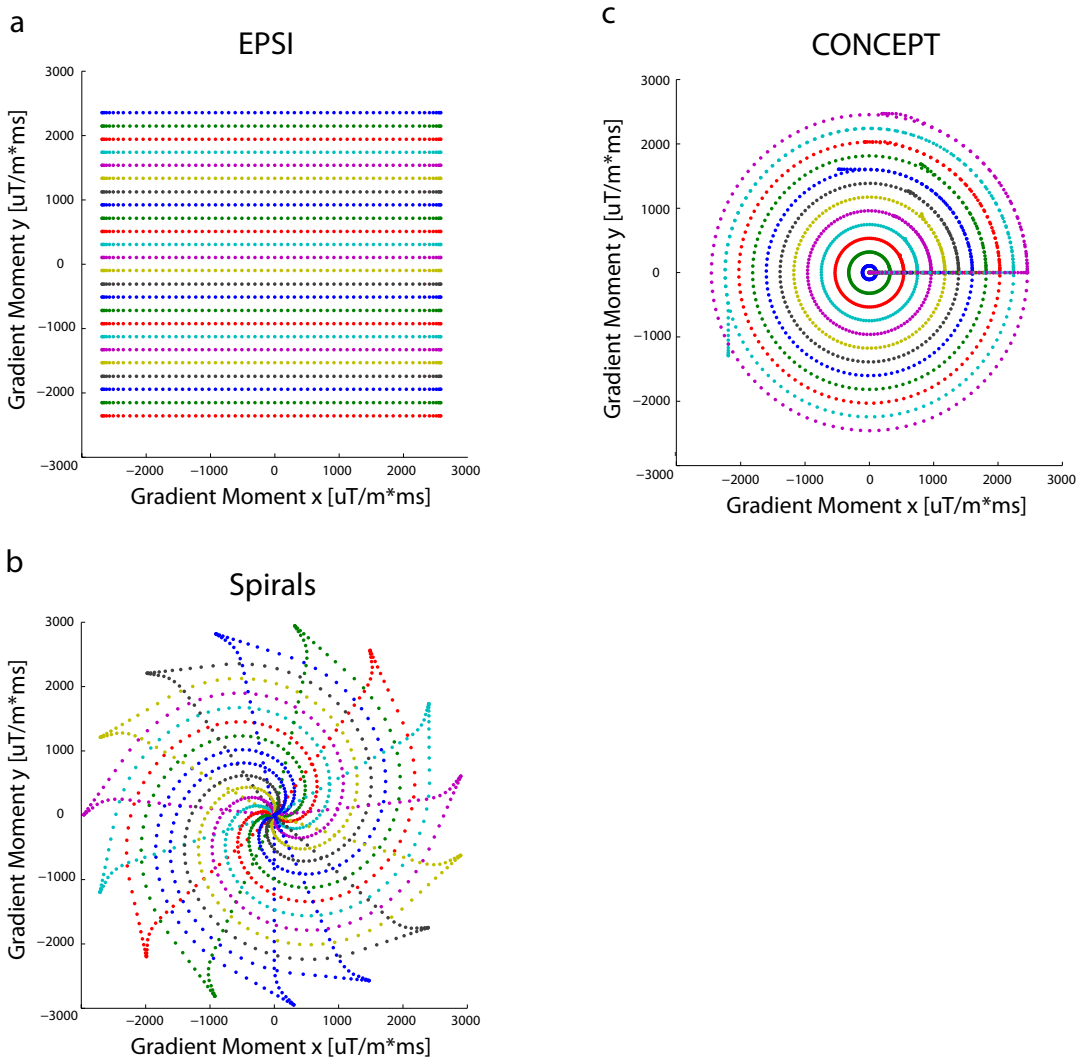

Figure 4.1: Illustration of an EPSI, spiral and CONCEPT trajectory in k-space for a 48×48 matrix with a FoV of 200×200 mm. The points along one spatial interleaf are equidistant in time, therefore indicating the trajectory velocity. Different colors represent different spatial interleaves, the recurrence of colors has no special meaning. The rewinders (EPSI and spirals), the trajectory for getting to the intended circles, and the trajectories for getting velocity zero at the end of the acquisition (CONCEPT) are also plotted. The latter are visible as deviations from the ciricles, especially well depicted in the previous to last circle.

We can solve eqs. (4.1) and (4.2) for T_{Ramp}, resulting in

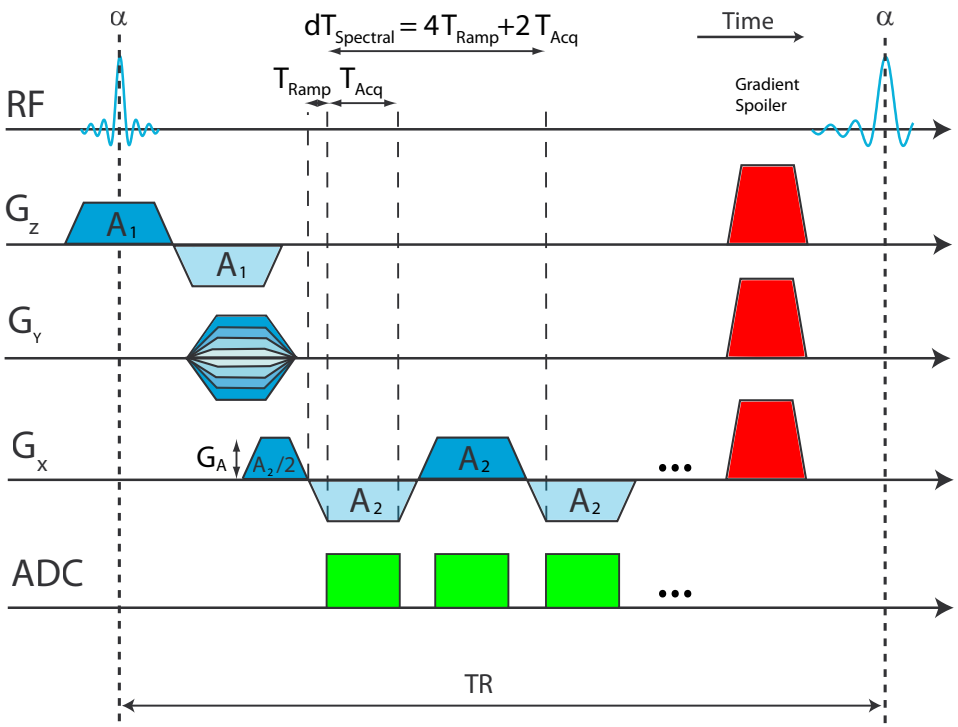

Figure 4.2: Sequence diagram of an EPSI sequence. At the end of the slice excitation block (RF excitation, slice-selection and slice-refocusing in z-direction), phase encoding is performed in the y-direction, and we move to the maximum k-space value along the x-direction with the gradient prewinder (first trapezoidal-shaped gradient in x-direction). Afterwards, we go back and forth along a k-space line by repetitive positive and negative gradients in x-direction. After repeating that about 500-2000 times, the transverse signal is spoiled (destroyed), and a new k-space line is measured in another repetition. The symbols A_1 and A_2 in the gradients should indicate gradients with the same area. The times T_{Ramp}, T_{Acq}, and $dT_{Spectral}$ are also shown.

$$T_{Ramp\pm} = \frac{nTI}{8BW_{Spectral}} \pm \sqrt{\frac{nTI^2}{4^3 BW_{Spectral}^2} - \frac{N_x}{2\gamma FoVS_{max}}} \tag{4.3}$$

The solution T_{Ramp-} results in higher quality factors, since less time is spent for ramping up and down, and more for acquiring the signal (T_{Acq}). Thus, the whole rewinding time, T_{Rew}, per TR is $T_{Rew} = 4 \cdot T_{Ramp-}$. According to Pohmann et al., the efficiency relative to a spin-echo phase encoded sequence is given by

$$\Omega_{EPSI}^{Total} = \Omega_{EPSI}^{AcqEff} = \sqrt{1 - T_{Rew}^{EPSI} \cdot BW_{Spectral}/nTI} \tag{4.4}$$

In the results section, the reached quality factors and acceleration factors of EPSI for different settings are given in table 4.1 and table 4.2. EPSI provides mediocre acceleration factors for the calculated settings in the range of 7-40 in comparison to elliptical phase encoding. From this table it is clear that EPSI has a low quality factor for very high resolutions ($\geq 220/64 \times 220/64\ mm^2$) and field strengths ≥ 7 T ($BW_{Spectral}/nTI \geq 926Hz$). Otherwise EPSI sequences are good choices, especially because the reconstruction is easier than for other sequences, as no regridding to a Cartesian grid is necessary. Therefore, PI in combination with EPSI is easier to perform than for other trajectories, however, with the drawback of higher g-factors (66).

4.2.2 Constant Linear Velocity, Constant Density Spirals

Idealized constant linear velocity, constant density spiral trajectories can be described by

$$k_{Spirals}(t) := \lambda\sqrt{t/T_{Acq}} \cdot (\sin(\omega\sqrt{t/T_{Acq}}), \cos(\omega\sqrt{t/T_{Acq}})) \tag{4.5}$$

with $t \in [0, T_{Acq}]$, where T_{Acq} is the duration of one spiral without its rewinder, $\lambda = N_x/(2FoV)$, N_x the matrix size in x-direction, $\omega = 2\pi n$, and $n = (N_x - 1)/(2nSI)$ being the number of spiral turns per number of spatial interleaves nSI to achieve the matrix size N_x. One example of a spiral trajectory is depicted in fig. 4.1 b.

We can calculate the linear velocity v of spirals as follows:

$$v(t) := ||d/dt\, k_{Spirals}(t)|| = \frac{\lambda}{2}\sqrt{\frac{\omega^2}{T_{Acq}^2} + \frac{1}{t \cdot T_{Acq}}} = \frac{\lambda}{2T_{Acq}}\sqrt{\omega^2 + \frac{T_{Acq}}{t}} \tag{4.6}$$

The velocity of a trajectory determines the time that is spent in a certain area of k-space, which in turn determines the k-space density. As we can see from eq. (4.6), the velocity is not constant with time, resulting in a non-uniform k-space density. However, the changes are small for large t, corresponding to the outer k-space. In other words, the spirals described by eq. (4.5) are non-uniform in the central part, but become nearly-uniform in the outer parts.

Nonetheless we can approximate spirals to be of constant k-space density, which will be done in this work. Thus, for calculating the efficiency, we do not need to consider the k-space density, but only the "sampling efficiency", i.e. the time during which we measure useful information. Therefore we need to compute the duration of the rewinders, which bring the spiral trajectory back to k-space center after each repetition of the trajectory. We can subdivide these rewinders into two parts: First, we need to slow down to zero velocity. Second, we have to play out a gradient to move the spirals back to k-space center. In theory, these two parts could be merged into one, giving a shorter total duration. However, this complicates the rewinder calculation and is therefore usually not done in practice, especially because the first part of the rewinder is very short anyway.

According to eq. (4.6) we have a linear velocity of $v(T_{Acq}) = \lambda/(2T_{Acq})\sqrt{\omega^2+1}$ right before the start of the rewinder, T_{Acq}, which can be written as $T_{Acq} = dT_{Spectral} - T_{Rew,Pt1} - T_{Rew,Pt2}$, where $T_{Rew,Pt1/2}$ are the durations of part 1 and 2 of the rewinder.

If we use the maximum slew rate, S_{max}, the time to slow down is implicitly given by:

$$T_{Rew,Pt1} = \frac{v(T_{Acq})}{\gamma S_{max}} = \frac{N_x\sqrt{4\pi^2(\frac{N_x-1}{2nSI})^2+1}}{4FoV\gamma S_{max}(dT_{Spectral} - T_{Rew,Pt1} - T_{Rew,Pt2})} \tag{4.7}$$

Solving this equation for $T_{Rew,Pt1}$ leads to

$$\begin{aligned} T_{Rew,Pt1} &= \frac{dT_{Spec} - T_{Rew,Pt2}}{2} - \sqrt{\frac{(dT_{Spec} - T_{Rew,Pt2})^2}{4} - x}, \\ x &= \frac{N_x\sqrt{\pi^2(\frac{N_x-1}{nSI})^2+1}}{4FoV\gamma S_{max}} \end{aligned} \tag{4.8}$$

where only the smaller solution was used. The number of spatial interleaves nSI is another degree of freedom which we can choose. From eq. (4.8) we can see that part 1 of the rewinder is shorter for larger nSI's. Later, we will further calculate that part 2 of the rewinder does not depend on nSI, see eq. (4.13). Therefore, spiral encoding gets more efficient with more spatial interleaves. However, if we choose a lot of spatial interleaves, we end up with an almost radial sequence, which of course is not our intention. Moreover, the k-space center is sampled more densly than the periphery as mentioned before. Using large nSI's increases this portion of the high-density k-space center. An easy compromise is setting $nSI = (N_x - 1)/2$, i.e. having exactly one spiral turn per

spatial interleaf, $n = 1$.

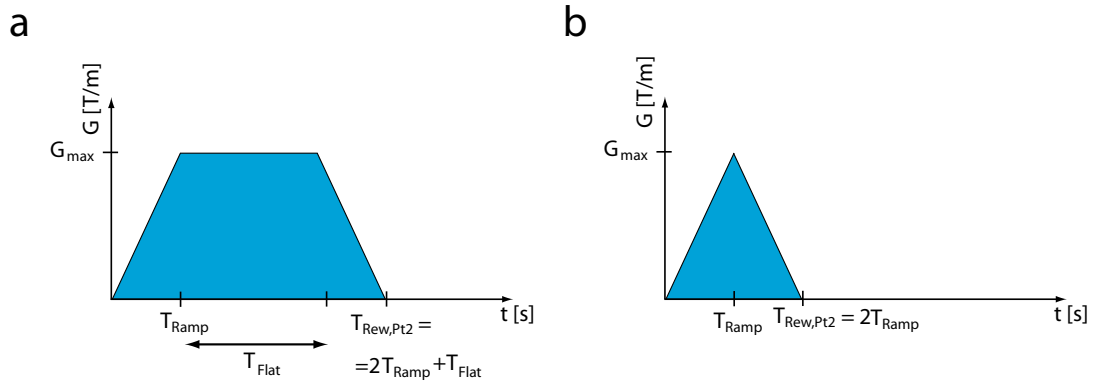

Figure 4.3: a: A trapezoidal-shaped gradient is the fastest gradient shape for rewinding the spiral k-space trajectory back to the k-space center. The gradient is ramped up within T_{Ramp} to the maximum gradient $G_{max} = S_{max}T_{Ramp}$ with the maximum slew rate S_{max}. After the ramping, the gradient is constant for the time T_{Flat} and then ramped down again within T_{Ramp}. b: The largest possible triangle using the maximum slew rate S_{max}. This is the border case between having a triangle gradient shape and a trapezoidal-shaped gradient shape: If a smaller gradient moment than that of this triangle is needed, it can be achieved with a triangle gradient within even shorter time. If a larger gradient moment is required, a trapezoidal-shaped gradient is needed, with a longer duration.

Let us now calculate the second part of the rewinder for getting back to the k-space center. At the end of the spiral trajectory, the distance of the trajectory to the k-space center is $k_{max} = ||k_{Spirals}(T_{Acq})|| = N_x/(2FoV)$, when ignoring the effect of the first part of the rewinder. Thus, the gradient moment we need to rewind is $GM = k_{max}/\gamma$. The fastest way to achieve a certain gradient moment is a trapezoidal-shaped gradient with an acceleration using the maximum slew rate S_{max} during the "ramp-up" and -down parts, see fig. 4.3 a. For the following treatise we will need the gradient moment that we can achieve with a triangle gradient, i.e. if the "flat top" part of the trapezoidal-shaped gradient has duration zero. This results in ramping with S_{max} up to the maximum gradient amplitude G_{max} during the time T_{Ramp}, and then ramping down to zero during the same duration, see fig. 4.3 b. The area of this triangle is its gradient moment and is given by $GM_{Tri} = T_{Ramp}G_{max}$, and the maximum gradient amplitude can be written as $G_{max} = S_{max}T_{Ramp}$, leading to

$$GM_{Tri} = G_{max}^2/S_{max} \tag{4.9}$$

Let us distinguish two cases for calculating $T_{Rew,Pt2}$:

Case 1: $GM = k_{max}/\gamma \leq GM_{Tri}$
In this case we can use a triangle gradient shape and do not need the full gradient amplitude G_{max}, but only a weaker gradient strength G_{used}. With $T_{Ramp} = T_{Rew,Pt2}/2$, the gradient moment can be calculated as $k_{max}/\gamma = G_{used}T_{Rew,Pt2}/2$. G_{used} can be written as $G_{used} = S_{max}T_{Rew,Pt2}/2$, resulting in

$$T_{Rew,Pt2} = 2\sqrt{\frac{k_{max}}{\gamma S_{max}}} \tag{4.10}$$

Case 2: $GM = k_{max}/\gamma > GM_{Tri}$
In this case we need the "flat-top" of the trapezoidal-shaped gradient, and therefore the total duration is $T_{Rew,Pt2} = T_{Flat} + 2T_{Ramp}$, the gradient moment is $k_{max}/\gamma = T_{Ramp}G_{max} + T_{Flat}G_{max}$ with $T_{Ramp} = G_{max}/S_{max}$, see fig. 4.3 a. We can rewrite the gradient moment as follows:

$$\begin{aligned} &k_{max}/\gamma = G_{max}(T_{Flat} + 2T_{Ramp} - T_{Ramp}) = G_{max}(T_{Rew,Pt2} - T_{Ramp}) = \\ &= G_{max}(T_{Rew,Pt2} - G_{max}/S_{max}) \end{aligned} \tag{4.11}$$

resulting finally in

$$T_{Rew,Pt2} = \frac{k_{max}}{\gamma G_{max}} + \frac{G_{max}}{S_{max}} \tag{4.12}$$

and

$$T_{Rew,Pt2} = \begin{cases} 2\sqrt{\frac{k_{max}}{\gamma S_{max}}} & k_{max}/\gamma \leq G_{max}^2/S_{max} \\ \frac{k_{max}}{\gamma G_{max}} + \frac{G_{max}}{S_{max}} & k_{max}/\gamma > G_{max}^2/S_{max} \end{cases} \tag{4.13}$$

The total efficiency of spiral encoding is thus

$$\Omega_{Spiral}^{Total} = \Omega_{Spiral}^{AcqEff} = \sqrt{1 - T_{Rew}^{Spiral} BW_{Spectral}} \tag{4.14}$$

with $T_{Rew}^{Spiral} = T_{Rew,Pt1} + T_{Rew,Pt2}$.

In the results section, the reached quality factors and acceleration factors of spirals for different settings are given in table 4.1 and table 4.2. In summary, spiral encoding offers

the highest acceleration factors R of up to 77. The acceleration can be even higher if more turns per angular interleaves are used. Yet, spirals offer rather low efficiencies for high spectral bandwidths and high resolutions.

4.2.3 Concentric Circles (CONCEPT)

In CONCEPT, concentric circles centered at the k-space center are measured. Circles are intrinsically closed trajectories, causing no time to be wasted for rewinder gradients. Therefore, $\Omega_{CONCEPT}^{AcqEff} = 100\%$. The spectral dwell time, i.e. the time between two consecutive circumnavigations of a circle, is usually kept constant between different circles. Since the area difference between two consecutive circles increases with the radius, the k-space density (time spent per k-space area) decreases with the circle radius k_r. This causes a drop of efficiency, if the target k-space density is uniform. Jiang et al. calculated this SNR drop to be $1 - \frac{\sqrt{3}}{2} \approx 13\%$, resulting in

$$\Omega_{CONCEPT}^{Density} = \Omega_{CONCEPT}^{Total} = 87\% \tag{4.15}$$

when a uniform k-space density is desired.

On the other hand, MRSI data are often filtered, e.g. with a Hamming filter, to reduce the leakage of signal from one voxel to its neighbouring voxels. Such filters are always low-pass filters, and therefore need a higher density around the k-space center than in the periphery. Since CONCEPT also has higher densities around the k-space center, it is closer to most target densities (filters) than a uniform density. This results in higher efficiencies of CONCEPT than EPSI or even phase encoded MRSI if the target density function is e.g. a Hamming filter.

Following is a derivation of the efficiencies of CONCEPT and of a uniformly sampled k-space when the target density is a Hamming filter. I follow the notation and calculations of Kasper et al. who derived efficiencies when measuring with a Gauss-shaped density vs. measuring uniformly and then applying the Gauss-filter in post-processing (52).

We can write the densities of CONCEPT, $\rho_{CONCEPT}$, the uniform acquisition, ρ_{Uni}, our Target density, ρ_{Target}, and the "matched" density, $\rho_{Matched}$, i.e. the density we would actually measure if we measured the target density, as follows:

$$\rho_{CONCEPT} = \frac{C_2}{\sqrt{k_x^2 + k_y^2}} \tag{4.16}$$

$$\rho_{Uni} = \frac{dT_{Spectral}}{k_{max}^2 \pi} \tag{4.17}$$

$$\rho_{Target} = C_1 \cdot Hamming(\frac{\sqrt{k_x^2 + k_y^2}}{k_{max}}) := C1 \cdot [\alpha - \beta cos(\pi(\frac{\sqrt{k_x^2 + k_y^2}}{k_{max}} + 1))] \tag{4.18}$$

$$\rho_{Matched} = dT_{Spectral} \cdot \rho_{Target} \tag{4.19}$$

where C_1 and C_2 are scaling constants, k_x and k_y are the positions in k-space, k_{max} is the maximum k-space value that should be measured (defined by the resolution), and $dT_{Spectral}$ is the acquisition time for one spectral time point. We additionally demand the following identities, to ensure a fair comparison between the different densities:

$$\int_{V_k} \rho_{CONCEPT}\, d^2k = \int_{V_k} \rho_{Uni}\, d^2k = \int_{V_k} \rho_{Matched}\, d^2k = dT_{Spectral} \tag{4.20}$$

where $V_k = k_{max}^2 \pi$ is the measured k-space volume, which I assume to have a circular area. We can derive the following equations from above identities:

$$dT_{Spectral} = \int_{V_k} \rho_{Matched}\, d^2k = dT_{Spectral} \cdot \int_{V_k} \rho_{Target}\, d^2k =$$
$$= 2\pi\, dT_{Spectral}\, C_1 \int_0^{k_{max}} k_r Hamming(\tfrac{k_r}{k_{max}})\, dk_r = 2\pi\, dT_{Spectral}\, C_1 \tfrac{k_{max}^2}{2}(\alpha - \tfrac{4\beta}{\pi^2})$$

where in the previous to last equality a transformation from Cartesian to polar coordinates was performed.
Therefore,

$$C_1 = \left(\pi k_{max}^2 \left(\alpha - \frac{4\beta}{\pi^2}\right)\right)^{-1} \tag{4.21}$$

The same can be done for C_2:

$$dT_{Spectral} = \int_{V_k} \rho_{CONCEPT}\, d^2k = C_2 \cdot \int_{V_k} \tfrac{1}{\sqrt{k_x^2 + k_x^2}}\, d^2k = C_2 2\pi \cdot \int_0^{k_{max}} \tfrac{k_r}{k_r}\, dk_r = C_2 2\pi k_{max}$$

leading to

$$C_2 = \frac{dT_{Spectral}}{2\pi k_{max}} \tag{4.22}$$

Now that we have determined the constants, we can calculate the noise powers $|\sigma|_2^2$ which are relevant for the SNR. If the target density is ρ_{Target} and the acquired density is ρ_{Acq}, the noise power can be calculated as follows according to Kasper et al. (52):

$$|\sigma_{Acq}|_2^2 = \int\limits_{V_k} \frac{\rho_{Target}^2}{\rho_{Acq}}\, d^n k \tag{4.23}$$

We can therefore calculate the noise power of CONCEPT:

$$|\sigma_{CONCEPT}|_2^2 = \int\limits_{V_k} \frac{\rho_{Target}^2}{\rho_{CONCEPT}}\, d^2k = \frac{C_1^2}{C_2} 2\pi \int\limits_0^{k_{max}} k_r^2 Hamming^2(\tfrac{k_r}{k_max})\, dk_r =$$
$$= \frac{C_1^2}{C_2} 2\pi \frac{k_{max}^3(4\alpha^2\pi^2+\beta^2(3+2\pi^2)-48\alpha\beta)}{12\pi^2} =: \frac{C_1^2}{C_2} 2\pi \frac{k_{max}^3 A_2}{12\pi^2}$$

resulting in

$$|\sigma_{CONCEPT}|_2^2 = \frac{A_2}{3\pi^2 dT_{Spectral}(\alpha - \frac{4\beta}{\pi^2})^2} \tag{4.24}$$

The same for the uniformly weighted k-space:

$$|\sigma_{Uni}|_2^2 = \int\limits_{V_k} \frac{\rho_{Target}^2}{\rho_{Uni}}\, d^2k = C_1^2 \cdot \frac{2\pi^2 k_{max}^2}{dT_{Spectral}} \cdot \int\limits_0^{k_{max}} k_r Hamming^2(\tfrac{k_r}{k_max})\, dk_r =$$
$$= \frac{1}{\pi^2 k_{max}^4 (\alpha - \frac{4\beta}{\pi^2})^2} \cdot \frac{2\pi^2 k_{max}^2}{dT_{Spectral}} \cdot \frac{k_{max}^2}{4}(2\alpha^2 + \beta^2 - \frac{16\alpha\beta}{\pi^2}) =: \frac{1}{\pi^2 k_{max}^4 (\alpha - \frac{4\beta}{\pi^2})^2} \cdot \frac{2\pi^2 k_{max}^2}{dT_{Spectral}} \cdot \frac{k_{max}^2}{4} A_1$$

resulting in

$$|\sigma_{Uni}|_2^2 = \frac{A_1}{2 dT_{Spectral}(\alpha - \frac{4\beta}{\pi^2})^2} \tag{4.25}$$

And for the matched density:

$$|\sigma_{Matched}|_2^2 = \int\limits_{V_k} \frac{\rho_{Target}^2}{\rho_{Matched}}\, d^2k = \frac{1}{dT_{Spectral}^2} \int\limits_{V_k} \rho_{Matched}\, d^2k = \frac{1}{dT_{Spectral}} \tag{4.26}$$

According to Kasper et al., the density-induced quality factors can then be calculated as follows (52)

$$\begin{aligned}\Omega^{HammTarget}_{CONCEPTVsMatched} &= \frac{SNR^{HammTarget}_{CONCEPT}}{SNR^{HammTarget}_{Matched}} = \sqrt{\frac{|\sigma_{Matched}|_2^2}{|\sigma_{CONCEPT}|_2^2}} = \\ &= (\alpha - \frac{4\beta}{\pi^2})\pi\sqrt{\frac{3}{A_2}} = \Omega^{HammTarget}_{CONCEPTVsMatched} \approx 0.9172\end{aligned} \tag{4.27}$$

$$\Omega^{HammTarget}_{UniVsMatched} = \frac{SNR^{HammTarget}_{Uni}}{SNR^{HammTarget}_{Matched}} = \sqrt{\frac{|\sigma_{Matched}|_2^2}{|\sigma_{Uni}|_2^2}} = (\alpha - \frac{4\beta}{\pi^2})\sqrt{\frac{2}{A_1}} \approx 0.7985 \tag{4.28}$$

$$\Omega^{HammTarget}_{CONCEPT} = \frac{SNR^{HammTarget}_{CONCEPT}}{SNR^{HammTarget}_{Uni}} = \frac{\Omega^{HammTarget}_{CONCEPTVsMatched}}{\Omega^{HammTarget}_{UniVsMatched}} = \pi\sqrt{\frac{3A_1}{2A_2}} \approx 1.1486 \tag{4.29}$$

This finally results in

$$\Omega^{Total}_{CONCEPT} = \Omega^{Density}_{CONCEPT} \approx \begin{cases} 0.87 \text{ for } \rho_{Target} = \rho_{Uni} \\ 1.15 \text{ for } \rho_{Target} = \rho_{Hamming} \end{cases} \tag{4.30}$$

Thus, the SNR of CONCEPT is even 15 % higher than for a conventional phase-encoded, uniformly weighted sequence, if the target k-space density is a Hamming filter. This is often the case in practice, as the PSF of unfiltered data is usually very poor for resolutions worse than $3.4 \times 3.4\,\mathrm{mm}^2$. Plots of $\rho_{Hamming}$, ρ_{Uni}, and $\rho_{CONCEPT}$ against the k-space radius are shown in fig. 4.4. ρ_{Acq} can be even shaped to match ρ_{Target} exactly by varying the distance between consecutive circles with the k-space radius k_r. Although we can achieve the same weighting in parts with spiral and EPSI MRSI, it is especially easy with CONCEPT. In spiral, introducing a variable density weighting prolongs the spectral dwelltime $dT_{Spectral}$, as we have to spend more time in the k-space center in comparison to constant density weighting. In EPSI, we would need to slow down in the center of each k-space line, which also prolongs $dT_{Spectral}$.

In the results section, the reached quality factors and acceleration factors of CONCEPT for different settings are given in table 4.1 and table 4.2. In summary, CONCEPT has many advantages, such as a very high SNR efficiency if a Hamming weighted k-space is desired, quite high acceleration factors, an easy to shape k-space density, and a quality factor $\Omega^{Total}_{CONCEPT}$ which does not decrease with increasing k-space extents or

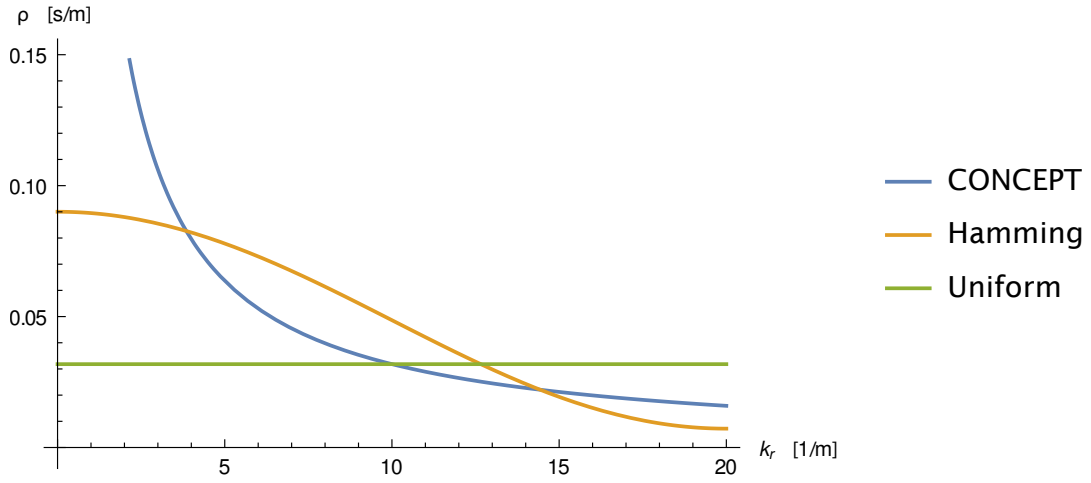

Figure 4.4: A comparison of different k-space densities: Uniform (e.g. EPSI or spirals), Hamming, and CONCEPT, i.e. $1/k_r$. The integral of all three densities is the same if multiplied by $2\pi k_r$ (due to the polar coordinate transform), thereby satisfying eq. (4.20). The CONCEPT density is closer to the desirable Hamming density than the uniform density, resulting in a higher SNR efficiency of CONCEPT than for a uniform density, and thus in $\Omega_{CONCEPT} > 1$ if the target density is Hamming.

spectral bandwidths. Among its drawbacks we have to count the inability to sacrifice SNR efficiency for increased resolutions or spectral bandwidths, and the worse $\Omega^{Density}$ in comparison to EPSI and spirals if a uniform k-space is desired.

4.3 Methods

4.3.1 Finding a Well-Suited Trajectory

Before any trajectory was implemented on the scanner, a trajectory fitting our needs had to be found. The trajectory had to fulfill the following requirements:

1. Acceleration of about $R \gtrsim 30$
2. Quality factor Ω^{Total} as high as possible
3. An intrinsically closed trajectory to achieve high Ω^{Total}

In addition to above requirements, the following settings were further demanded:

1. Spectral bandwidth of about $\gtrsim 1800\,\mathrm{Hz}$
2. Spectral bandwidth of at least 750 Hz free of temporal interleaving artifacts $\Rightarrow BW_{Spectral}/nTI > 750\,\mathrm{Hz}$

3. voxel sizes of $\lesssim 3.4 \times 3.4\,\mathrm{mm}^2$

The closedness of the trajectory is not an absolute necessity, but closed trajectories tend to have higher Ω^{Total}, because no time is wasted for the gradient rewinder.

Several trajectories were considered and estimated whether they could fulfill the criteria: EPSI, radial EPSI (also called Projection Reconstruction Echo-Planar (PREP) imaging), spirals, rosettes, and CONCEPT. EPSI was estimated to provide too low accelerations R, too low Ω^{Total} for the demanded spectral bandwidths and spatial resolutions, and is further not an intrinsically closed trajectory. Radial EPSI has far too low Rs, is not closed, but could nevertheless provide quite high Ω^{Total}, since the length of one line is only half of that of conventional EPSI. Spirals provide a bad Ω^{Total}, as they are not intrinsically closed.
The remaining two trajectories, rosettes and CONCEPT, both fulfill all criteria, but provide highly non-uniform k-space densities. As a result, the $\Omega^{Density}$ and thus Ω^{Total} are below 1 if the target density is uniform. In case of rosettes it is 0.9, while for CONCEPT this factor is 0.87. However, this disadvantage can be converted into an advantage, if the target density is chosen to be e.g. a Hamming filter. In this case, CONCEPT has two advantages over rosettes: First, the density of rosettes is high in the center, decreases with the radius, and then increases again at the k-space periphery. CONCEPT, however decreases with $1/k_r$. Therefore, the density of CONCEPT is closer to the Hamming filter than rosettes, resulting in a higher $\Omega^{Density}$, if the target density is Hamming. Second, the k-space density can be easily modified in CONCEPT, e.g. by varying the distance between consecutive concentric circle. This task is not trivial at all for rosettes.
Thus, CONCEPT was finally chosen as the trajectory suited best for our needs, and was implemented on the scanner.

4.3.2 Implementation of CONCEPT

The CONCEPT read-out was implemented into the sequence of chapter 3. The modules of 2D-CAIPIRINHA, and the integrated MUSICAL pre-scan were removed from the sequence, as 2D-CAIPIRINHA cannot be performed in CONCEPT, and the MUSICAL pre-scan was implemented differently: In every TR, the same trajectory is played out as for the MRSI scan, but before the water suppression, only with a small flip angle of 5°, and only with a few circumnavigation of the current circle, i.e. vector size points.

The implementation of the circular gradient trajectories consists of three parts: The first is the gradient pre-winder, with the purpose to bring the current k-space position to the desired circle radius k_r (Part 1a), and accelerate tangentially along the circle to acquire the tangential velocity $k_r \cdot 2\pi BW_{Spectral}$ (Part 1b). Part 1a and 1b can be merged by solving a calculus of variation problem, but for simplicity they were implemented sequentially here. Part 2 simply consists of all the circumnavigations of the circles: The gradient waveform of the current circle is played out $vecSize/nTI$ times, where vecSize is the desired number of FID points. The gradient waveforms were defined as:

$$\begin{pmatrix} G_x \\ G_y \end{pmatrix} := k_r 2\pi BW_{Spectral} \begin{pmatrix} -\sin(2\pi BW_{Spectral} \cdot t) \\ \cos(2\pi BW_{Spectral} \cdot t) \end{pmatrix} \tag{4.31}$$

In the third part, the velocity has to be reduced to zero by simply ramping down from the current velocity to zero velocity in both directions using the maximum slew rate.

One problem occurring on a real scanner is the change of the gradients with the frequency $BW_{Spectral}$ which is in the order of 500-3000 Hz, i.e. in the acoustic range. The gradient coils in an MR system are bent if gradient waveforms are played out due to the interaction between the main magnetic field and the field caused by the gradients. These gradients are the main source of the audible noise caused by an MR system. For certain acoustic frequencies, the gradients can cause other parts of the MR system to vibrate in resonance, which therefore produces even more noise or can even destroy the gradient coils (67). The acoustic resonances are specified as 550 ± 50 Hz, and 1100 ± 150 Hz for our Siemens 7T Magnetom scanner with the gradient system SC72C. Therefore, some spectral bandwidths are not safe to be used in our CONCEPT sequence. This problem was solved by checking for the acoustic resonances of the MR system the sequence is run on, and if the user chooses a spectral bandwidth within an acoustic resonance, the closest allowed spectral bandwidth is chosen.

This and some other checks for the operationality of the settings were implemented in the so called “prep”-part of the sequence. In this part, the sequence is tested with many different settings (different TRs, TEs, bandwidths, etc.), and only possible settings are shown to the user. To minimize computational burden, only the setting operationality is tested in this part, but the gradient waveforms themselves are not yet calculated.
The gradient waveforms are calculated in the so called “run”-part of the sequence. This

might cause problems, if the calculations are slower than the duration of the played out objects. Yet, this problem has never occurred when running the sequence.

To prove the successful implementation of CONCEPT including the MUSICAL pre-scan, a silicone oil phantom was measured without water suppression with a matrix size of 64×64, FoV $220 \times 220\,\mathrm{mm}^2$, and a spectral bandwidth of 1852 Hz. The MUSICAL pre-scan, as well as the MRSI data, were regridded to an equidistant, rectilinear k-space, density compensated and Fourier transformed to obtain images. The fifth FID point (i.e. fifth circumnavigation of the circle) of the MRSI data was compared against the MUSICAL pre-scan data for one of the 32 array coil channels.

4.3.3 Implementation of MUSICAL into Spiral Sequence

The spiral sequence source code was provided by Borjan Gagoski. Only three minor changes were done in the sequence source code: The spectral bandwidth and spatial resolution were adapted to our needs, some small bugs were fixed in the gradient rewinder, which slightly reduced their duration and slew rate overshoots, and a MUSICAL pre-scan was implemented into the sequence. The latter was done almost the same way as in the CONCEPT sequence. The MUSICAL coil combination was implemented into the image reconstruction of the spiral sequence, which was also provided by Borjan Gagoski.

4.3.4 Theoretical Comparison of Spirals, EPSI and CONCEPT

The chosen gradient waveform, i.e. CONCEPT, was theoretically compared to two other standard gradient waveforms, EPSI and spirals. The quality factors, Ω_{Total}, according to eqs. (4.4), (4.14) and (4.30), as well as the achieved acceleration factors, were calculated for different settings. These settings were chosen as a low (32×32), high (64×64), and an ultra-high (100×100) spatial resolution, all with a FoV of $220 \times 220\,\mathrm{mm}^2$, and a low (1230 Hz, $nTI = 2$) and a high (2778 Hz, $nTI = 3$) spectral bandwidth. The 64×64 matrix with 2778 Hz bandwidth corresponds to the setting most suitable to our needs.

4.3.5 In-Vivo Comparison of Spirals, 2D-CAIPIRINHA and CONCEPT

Data Acquisition

Since EPSI is not available at our scanner, CONCEPT was compared *in-vivo* only to spirals and 2D-CAIPIRINHA. One volunteer was measured on a 7T MR scanner with a 32-channel head coil including a single channel volume coil for signal transmission. The

parameters common for all sequences were as follows: FoV of $200 \times 200\,\mathrm{mm}^2$, TR of 600 ms, acquisition delay of 1.3 ms, one slice with a slice thickness of 12 mm, acquisition window of 272 ms, elliptically filtered (i.e. only k-space points within a circle were measured).
The parameters of the 2D-CAIPIRINHA sequence were: 48×48 matrix size, 2D-CAIPIRINHA with an acceleration of $R = 3$, 6000 Hz spectral bandwidth, 1632 spectral points (truncated in post-processing), measurement time 6m 20s.
The parameters of the spiral sequence were: 48×48 matrix size, 1852 Hz spectral bandwidth, 512 spectral points (truncated in post-processing), 11 averages, two temporal interleaves, measurement time 6m 40s.
The parameters of the CONCEPT sequence were: 64×64 matrix size (reconstructed once as a 48×48 matrix in post-processing by omitting the outer circles, and once with the full matrix size), 1852 Hz spectral bandwidth, 512 spectral points, two temporal interleaves, 13 averages, measurement time 8m 20s for the 64×64 matrix size, resulting in a corresponding measurement time of 6m 20s for the 48×48 matrix size.

Reconstruction

The spiral reconstruction was done by the online image reconstruction provided by Borjan Gagoski, including the MUSICAL coil combination. The CONCEPT data were regridded to a Cartesian k-space, and density compensated, while the 2D-CAIPIRINHA data were reconstructed with the algorithm described in chapter 3. In both cases, the data were then Fourier transformed, and coil combined using MUSICAL. The spiral, 2D-CAIPIRINHA, and CONCEPT data were finally Hamming filtered and the spectra were fitted with LCModel.

Evaluation

Metabolic maps of tNAA, tCho and Glx, and CRLB maps of tCho and Glx were compared between the three methods. Representative spectra were further compared. The SNR and Glx CRLB values were compared quantitatively between the different methods.

4.3.6 Refined Setting

The settings with only 1852 Hz spectral bandwidth of the spiral and CONCEPT sequences resulted in spectral aliasing of a lipid sideband from -3.4 ppm to 2.85 ppm. This caused tCr not to be reliably fitted. Therefore, the spectral bandwidth was increased to 2778 Hz, with $nTI = 3$ instead of $nTI = 2$. The spectral bandwidth per nTI

remained the same. Increasing nTI causes an additional spectral interleaving artifact. However, since the bandwidth per nTI did not change, the artifacts are at the same distance from water as with 1852 Hz and $nTI = 2$, but on both sides of water instead of only on one side. The settings with only 1852 Hz spectral bandwidth also caused the lipids to alias to the downfield regions.
To show the problem that is caused by the lipids aliasing to the downfield side of water, a comparison of spectra with the full spectral range for the Cartesian and CONCEPT sequence is shown.

Further measurements for comparing spirals, 2D-CAIPIRINHA and CONCEPT with the refined settings will be performed in the future with several volunteers. Here, the measurement of only one volunteer with the old and the refined settings, and only with CONCEPT, has to suffice to show that the refined settings improved the data quality.

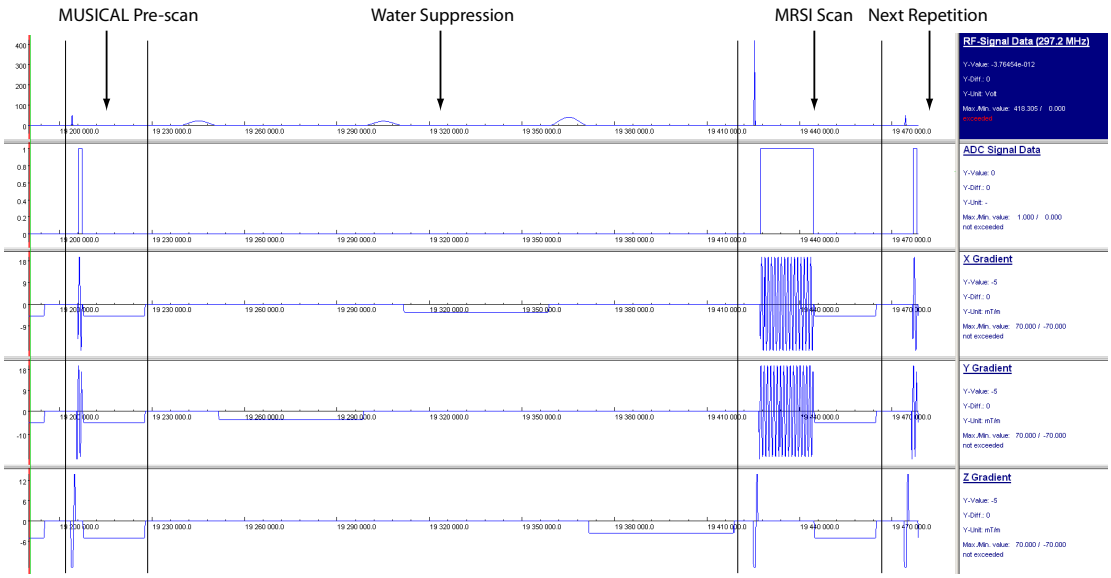

Figure 4.5: Sequence diagram showing the MUSICAL pre-scan, the water suppression module, and the MRSI scan of the CONCEPT sequence. From top to bottom, the RF pulses, analog-to-digital converter data acquisition, and x-, y-, and z-gradients are shown. The MUSICAL pre-scan is the same as the actual MRSI scan, but before water suppression, with a smaller flip angle, and with fewer spectral points (circumnavigation of the circle).

4.4 Results

4.4.1 Implementation of CONCEPT

The MUSICAL pre-scan modules are indicated in fig. 4.5. In fig. 4.6, the three parts of the CONCEPT implementation, pre-winder, circumnavigations of the circles, and ramp down are shown in more detail. Images of a phantom showing the MUSICAL pre-scan and the normal MRSI scan, also without water suppression, are shown in fig. 4.7. The magnitude as well as the phase of the two datasets look very similar, except of different SNRs and a global scaling factor between the two magnitude images, stemming from different flip angles. This proves that MUSICAL is very well suited to provide good coil combination weights, as one gold standard for coil combination in MRSI is to measure the same MRSI data without water suppression, and using these additional data as weights.

4.4.2 Theoretical Comparison of Spirals, EPSI and CONCEPT

The quality factors of EPSI, spirals, and CONCEPT are shown in table 4.1 for the different simulated settings. For CONCEPT, the quality factor is given if a uniform k-space density is desired, as well as if a Hamming weighted k-space density is requested. In table 4.2, the acceleration factors are shown for EPSI, spirals, and CONCEPT for the same settings. The acceleration is calculated with elliptical phase encoding as the reference.

4.4.3 In-Vivo Comparison of Spirals, 2D-CAIPIRINHA and CONCEPT

In fig. 4.8, the metabolic maps of tNAA, tCho, and Glx are shown for 2D-CAIPIRINHA, Spiral, CONCEPT with a 48×48 matrix size, and CONCEPT with a 64×64 matrix size. The 2D-CAIPIRINHA maps clearly look best and show most anatomical details. Spiral seems to have more artifacts than the other methods.
Fig. 4.9 shows the CRLB maps of Glx for the same methods. Again, 2D-CAIPIRINHA has the lowest values, and spiral the highest.
In fig. 4.10, spectra fitted by LCModel at the positions indicated by arrows in fig. 4.9 are shown. This figure shows the problem of the spiral and CONCEPT sequences: The baseline, as fitted by LCModel, is very curved. Using a higher resolution improved the baseline in CONCEPT. Also, if the spectra were shifted before regridding, causing the main lipid peak not to alias, often improved the baseline (not shown). The baseline distortions are partly caused by a lipid sidelobe at $-3.4\,\mathrm{ppm}$, which aliases between tNAA

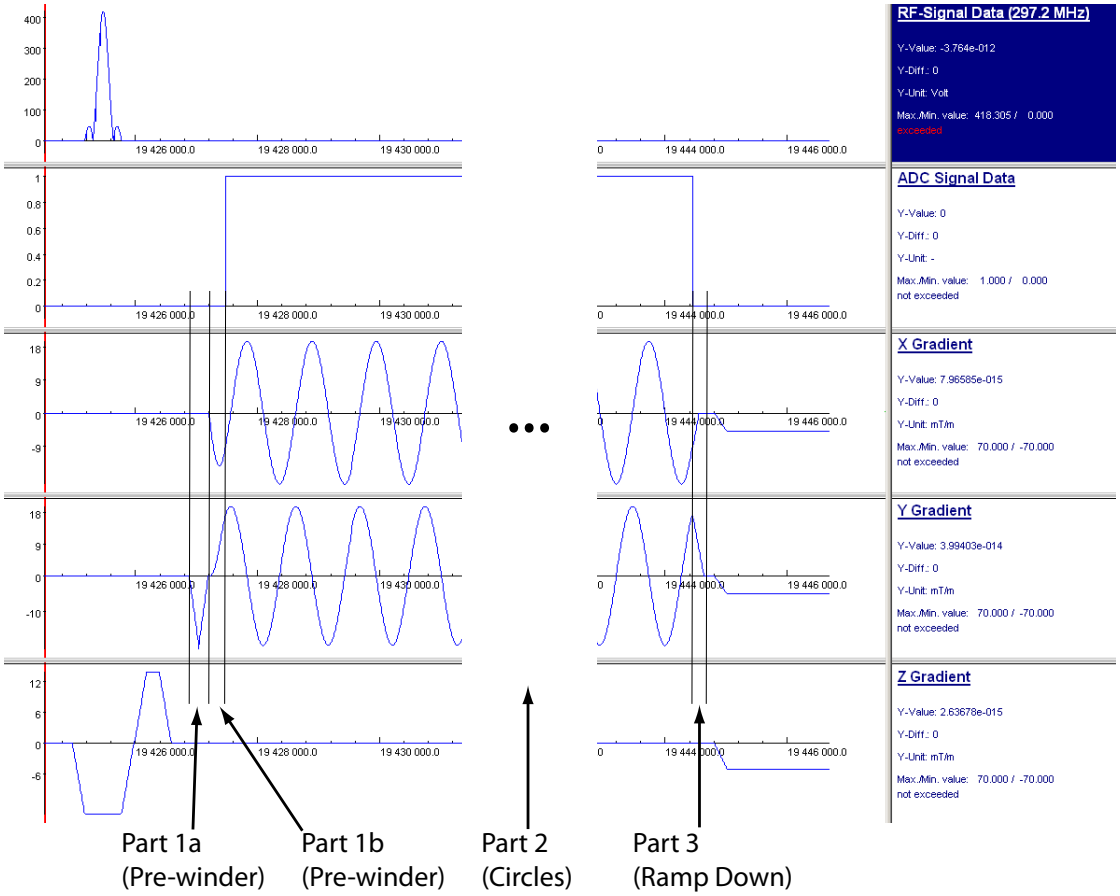

Figure 4.6: Diagram of the CONCEPT sequence showing the three parts of the gradient trajectory. The first part brings the current k-space location to the desired radius (part 1a), and accelerates tangentially (part 1b) for acquiring the necessary angular velocity so that one circle circumnavigation can be performed within the time $dT_{Spectral}/nTI$. Part 2 are all circumnavigations of the circle. In part 3, the gradients are ramped down to zero.

and tCr for the used spectral bandwidth. In contrast, the spectra of 2D-CAIPIRINHA are quite flat.

The SNRs (median ± mad) as reported by LCModel were 16.0±1.8, 9.0±1.6, 13.0±2.3, 13.0±2.8 for 2D-CAIPIRINHA, spirals, CONCEPT 48 × 48, and CONCEPT 64 × 64, respectively. The Glx CRLB values (median ± mad) were 5.0±1.0, 9.0±2.0, 6.0±1.7 and 6.0±1.8, for the same methods.

	Ω^{Total}_{EPSI} [%]	Ω^{Total}_{Spiral} [%]	$\Omega^{Total}_{Concept,Uni}$ [%]	$\Omega^{Total}_{Concept,Hamm}$ [%]
32×32 1230Hz, 2 TIs	97.2	93.5	86.6	114.9
32×32 2778Hz, 3 TIs	93.0	89.4	86.6	114.9
64×64 1230Hz, 2 TIs	94.0	90.2	86.6	114.9
64×64 2778Hz, 3 TIs	79.1	83.0	86.6	114.9
100×100 1230Hz, 2 TIs	89.3	87.0	86.6	114.9
100×100 2778Hz, 3 TIs	-	75.3	86.6	114.9

Table 4.1: Theoretical quality factors of the different SSE methods with respect to elliptical phase encoded MRSI for different measurement parameters. The 1230Hz correspond to 10 ppm at a 3T-scanner, while the 2778Hz correspond to 9.3 ppm at a 7T scanner. The 100×100 resolution and 2778Hz with 3 temporal interleaves is not possible to achieve with EPSI. The quality factor for CONCEPT is given for a uniform target density and a Hamming weighted target density, in both cases in comparison to a uniform density as gold standard. For spiral and EPSI, the Hamming target density is the same as the uniform target density, because the k-spaces of spiral and EPSI, as well as of the gold standard, are uniform.

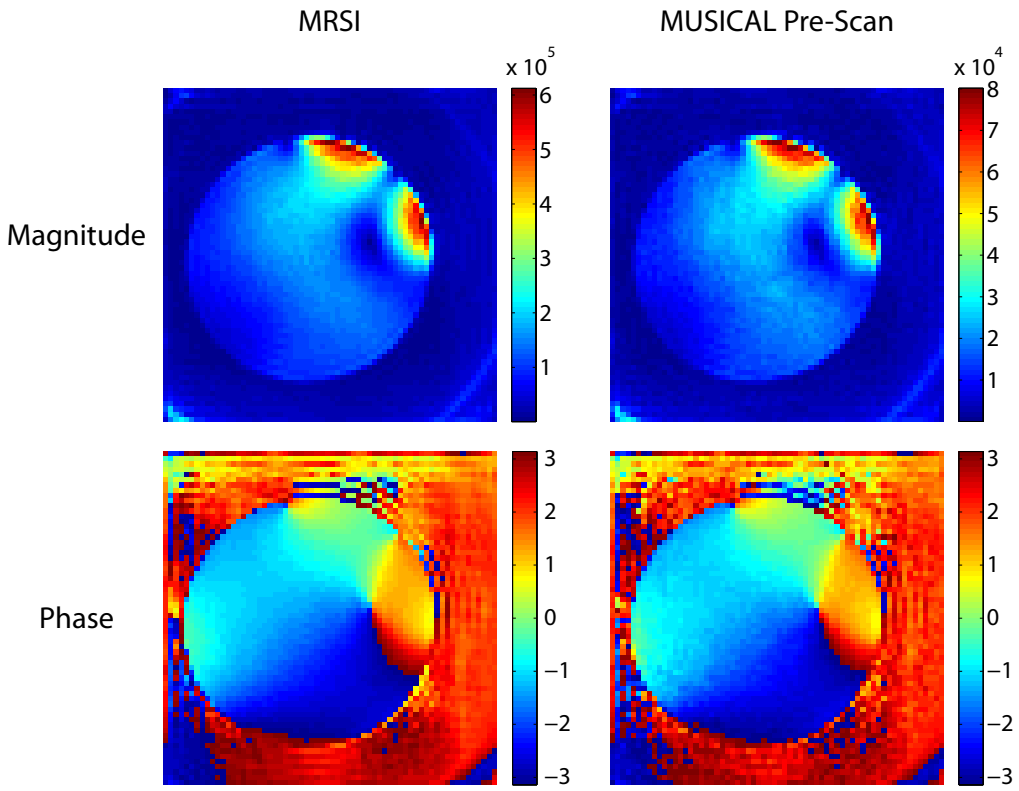

Figure 4.7: Magnitude and phase images of one channel of the MRSI data without water suppression, and the MUSICAL pre-scan. In both cases, the fifth FID point was used. The phantom was filled with silicone oil. Both data sets were gridded to a Cartesian k-space and Fourier transformed. The images look very much alike, except of different SNRs and a global scaling factor. Thus, the MUSICAL pre-scan can be assumed to provide good coil combination weights.

4.4.4 Refined Setting

To show the problem of the curved baseline and the aliased lipid sideband, a comparison of the full spectral range between the Cartesian sequence and CONCEPT for a voxel close to the skull is shown in fig. 4.11. In case of the CONCEPT sequence, the lipid aliases from 1.3 ppm to 7.5 ppm. This seems to strongly deteriorate the baseline of the spectrum, even in the metabolite range of $1.5 - 4.0$ ppm. Additionally, the lipid sideband around 2.85 ppm is visible. The aliased lipid peak is much higher than for the Cartesian data. One reason for that is that due to the aliasing, a wrong frequency is assigned to the lipid peak, which causes a wrong reconstruction before regridding. As a result, the aliased lipid signal is spread over the whole slice. A comparison between

	R_{EPSI} [ ]	R_{Spiral} [ ]	$R_{CONCEPT}$ [ ]
32×32 1230Hz, 2 TIs	11.1	23.6	22.2
32×32 2778Hz, 3 TIs	7.4	15.8	14.8
64×64 1230Hz, 2 TIs	23.4	48.4	46.9
64×64 2778Hz, 3 TIs	15.6	32.3	31.3
100×100 1230Hz, 2 TIs	37.6	76.8	75.3
100×100 2778Hz, 3 TIs	-	51.2	50.2

Table 4.2: Theoretical acceleration factors with respect to elliptical phase encoded MRSI of the different SSE methods for different measurement parameters. The 1230Hz correspond to 10 ppm at a 3T-scanner, while the 2778Hz correspond to 9.3 ppm at a 7T scanner. The 100×100 resolution and 2778Hz with 3 temporal interleaves is not possible to achieve with EPSI.

the metabolic maps of tNAA, tCho, and Glx from CONCEPT with the old settings, 1852 Hz, $nTI = 2$, and the refined settings, 2778 Hz, $nTI = 3$ is shown in fig. 4.12. Spectra from the positions indicated by red arrows in the T_1-weighted image of fig. 4.12 are shown in fig. 4.13. Increasing the spectral bandwidth clearly reduced the curviness of the baseline spectra, and thus improved the metabolic map quality, especially of the tCr map. With $nTI = 2$, a lipid sideband artifact is present at the locations indicated by arrows in fig. 4.13, which aliases from -3.4 ppm to frequencies between tNAA and tCr.

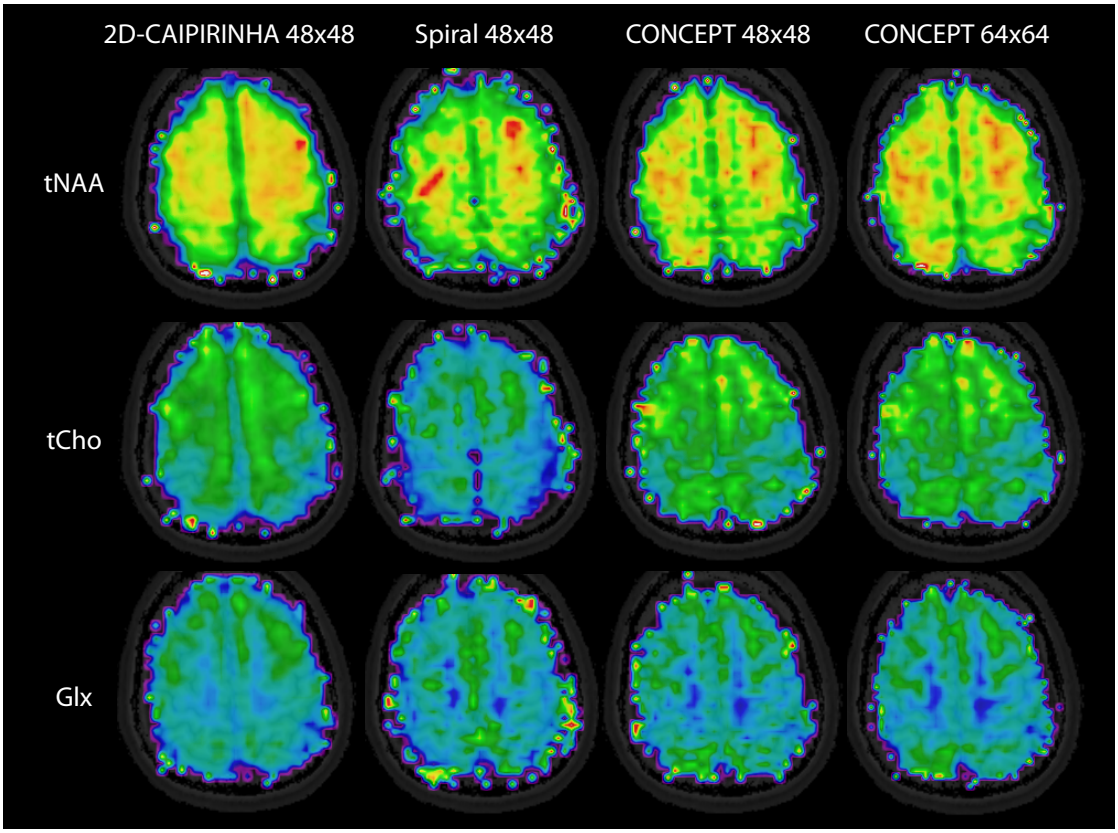

Figure 4.8: Metabolic maps of tNAA, tCho and Glx for the four compared methods, 2D-CAIPIRINHA, spirals, CONCEPT 48×48, and CONCEPT 64×64. 2D-CAIPIRINHA shows most anatomical details, while spirals show the least. The reason for the poor quality of the spiral and CONCEPT maps are the lipid aliasing to the downfield side of water as shown in fig. 4.11, and the lipid sideband aliasing to 2.85 ppm as shown by fig. 4.13, both due to the low spectral bandwidth. These problems were overcome with the refined settings.

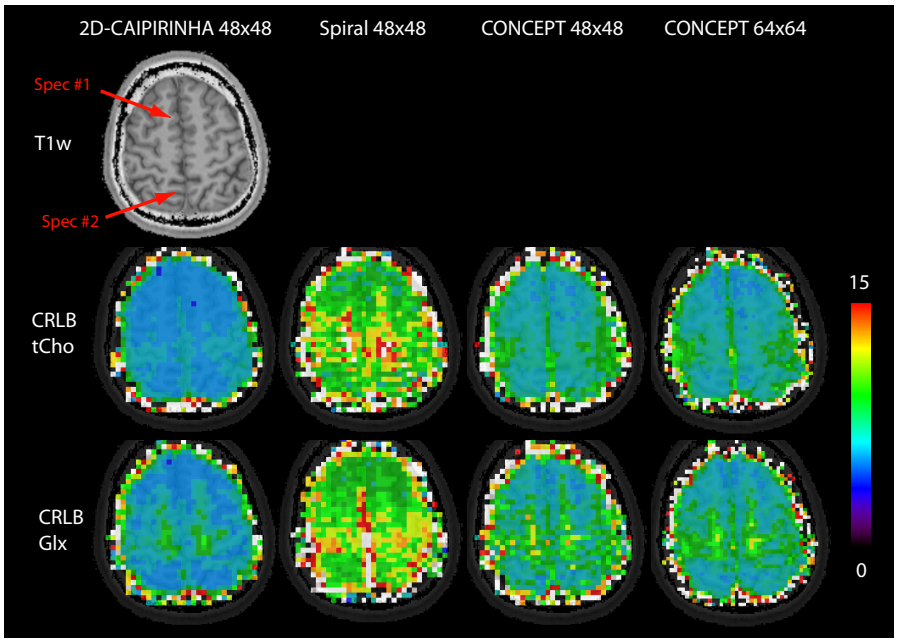

Figure 4.9: A T_1-weighted image of the same slice as the Glx CRLB maps for 2D-CAIPIRINHA, spirals, CONCEPT 48×48, and CONCEPT 64×64 as provided by LCModel. 2D-CAIPIRINHA provides the lowest values, while the spiral has the highest.

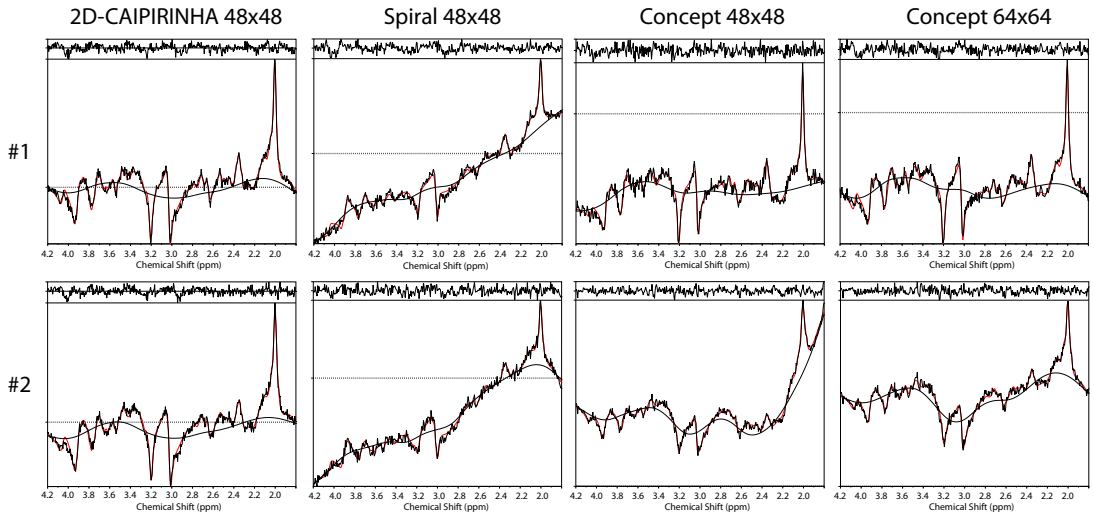

Figure 4.10: Spectra as provided by LCModel from the positions indicated by the red arrows in fig. 4.9. The baseline of spiral and CONCEPT data is very curved, which is why the metabolic maps in fig. 4.8 are of quite low quality. The reason for the curved baseline is the low spectral bandwidth of only 1852 Hz. This issue was fixed with the refined settings.

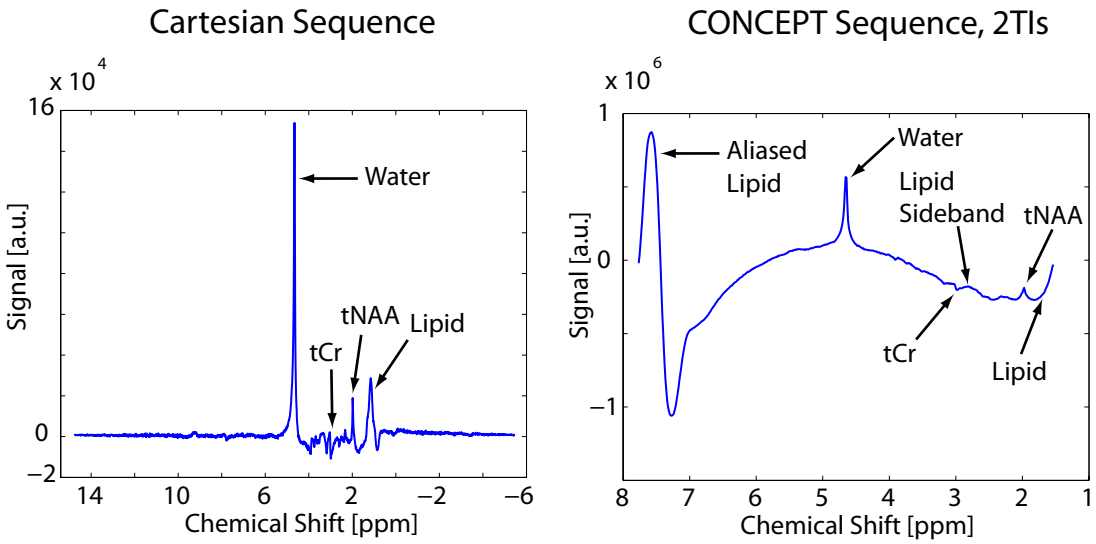

Figure 4.11: Comparison of the whole spectral range between the Cartesian and the CONCEPT sequence of the same voxel. Due to the narrow spectral range of the CONCEPT sequence, the lipid signals at 1.3 ppm alias to 7.5 ppm. This causes the aliased lipid signal to spread over the whole slice, which explains why this signal is so much higher in the CONCEPT spectrum in comparison to the Cartesian spectrum. For an unknown reason, this also seems to strongly distort the whole baseline. In addition, the lipid sideband artifact is visible around 2.85 ppm in the CONCEPT spectrum.

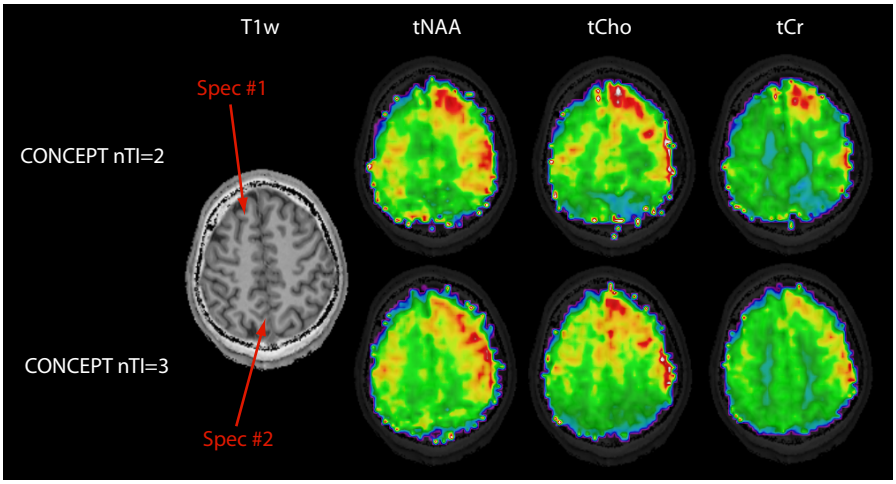

Figure 4.12: Metabolic maps of CONCEPT with the old settings, $BW_{Spectral} = 1852\,\text{Hz}$, $nTI = 2$, and the refined settings with $BW_{Spectral} = 2778\,\text{Hz}$, $nTI = 3$. The new settings improved the metabolic maps, especially of tCr.

4.5 Discussion

4.5.1 Finding a Well-Suited Trajectory

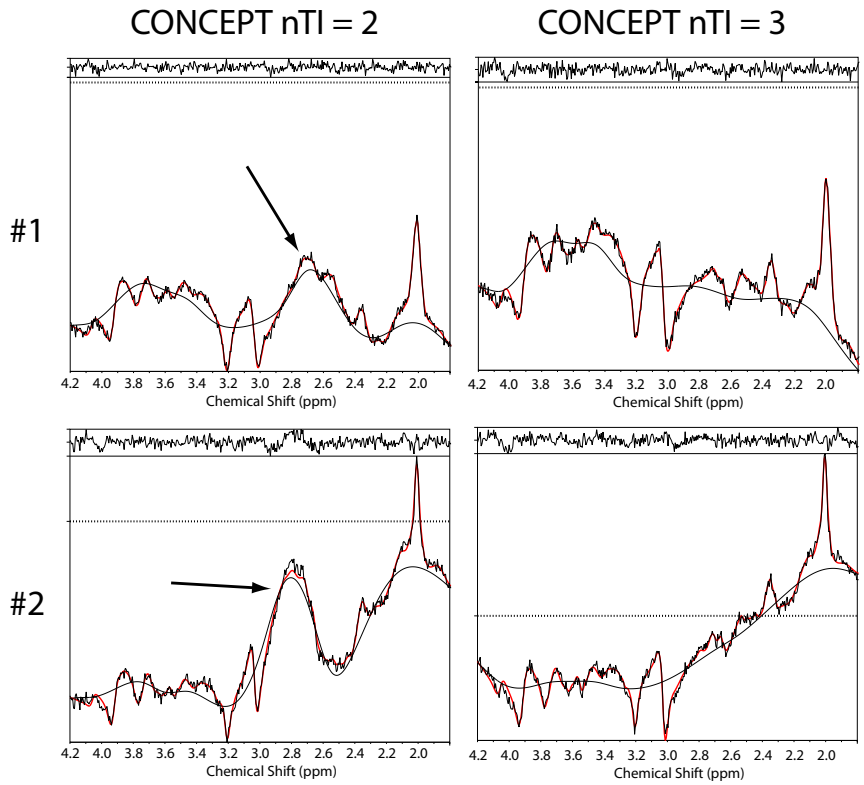

Figure 4.13: Spectral comparison of the old settings and the refined settings of the voxels indicated by red arrows in fig. 4.12. The increased bandwidth reduced the lipid artifacts which are present in the old settings ($nTI = 2$), as indicated by black arrows.

A trajectory was found which suited our needs, i.e. high spectral bandwidths per temporal interleaf, necessary due to the high magnetic field, and small voxel sizes of $\lesssim 3.4 \times 3.4\,\mathrm{mm}^2$. EPSI, radial EPSI, and spirals did not fulfill our needs because of too low acceleration factors or too low quality factors. Rosettes and CONCEPT were both suitable, but CONCEPT was chosen due to its rather easy adaption to any target k-space density and its natural k-space density of $1/k_r$ closer to a Hamming filter.

The requirement of the trajectory to be closed is a distinct difference to conventional MRI, where the trajectory has to be traversed only once, whereas in MRSI the trajectory has to be traversed $500 - 2000$ times for acquiring spectral information. Therefore, most

trajectories that are excellently suited for MRI are suboptimal in MRSI, such as EPSI or spirals. The penalty on Ω^{Total} stemming from a non-closed trajectory increases with the acquired k-space extent (equivalent to high resolutions), and with shorter durations for one repetition of the trajectory (equivalent to the inverse of the spectral bandwidth per temporal interleaf). Thus, at lower magnetic fields or lower resolutions, Ω^{Total} can be easily in the range of 0.90-0.99 even for non-closed trajectories. In such situations, it is of course not important to use a closed trajectory.

4.5.2 Implementation of CONCEPT

The CONCEPT gradient waveforms were sucessfully implemented into an FID-sequence, including MUSICAL. The MUSICAL pre-scan can be assumed to provide very good coil combination weights, since it matches very well with the non-water suppressed MRSI data.

4.5.3 Theoretical Comparison of Spirals, EPSI and CONCEPT

For low resolutions or small spectral bandwidths, the quality factor of spirals and EPSI are close to 100 %. However, for the target setting, 64×64, 2778 Hz, $nTI = 3$, the quality factors drop already to 79.1 and 83.0 % for EPSI and spiral, respectively. If a flat k-space density is desired, CONCEPT is barely more efficient with 86.6 %. Yet, if a Hamming density is desired, the quality factor of CONCEPT rises to 114.9 %, which means CONCEPT is even more efficient than conventional phase-encoded MRSI with a uniform k-space density. Of course, conventional, phase encoded MRSI can also be measured to match any target filter, e.g. by changing the distance between k-space points depending on the k-space position (re-gridding of the k-space points is then necessary, as the points do no longer lie on a Cartesian grid), or to approximate the target filter by acquisition weighting (68). However, these options would require enormous measurement times in the order of several hours for one slice with a matrix size of 64×64. If calculating the quality factors with a phase encoded MRSI sequence having a Hamming weighted k-space density as the gold standard, the quality factor of CONCEPT would drop to $\Omega^{HammTarget} \approx 91.72\%$, while the other methods such as EPSI and spirals would also drop by another factor of $\approx 79.85\%$, as calculated in the theory section. Yet, I decided to calculate the quality factor of CONCEPT, $\Omega^{HammTarget}$, with a **uniform**, phase encoded MRSI as a reference. I think this is justified by the impracticability of phase

encoded MRSI with a Hamming k-space density due to the very long measurement times.

The acceleration factors are especially low for the EPSI sequence, reaching its maximum of 38 for a 100×100 matrix. The acceleration of spirals and CONCEPT are very similar. Spirals could in principle accelerate much more, if the requirement of the spiral turns per spatial interleaves being one, $n = 1$, would be relaxed. However, this would cause the number of temporal interleaves to increase in the settings of matrix sizes ≥ 64, and $BW_{Spectral} \geq 2778$, and would thus be not practical.
Although the accelerations of spirals and CONCEPT are on the lower end of the acceptable range for the target settings (matrix size of 64×64, $BW_{Spectral} = 2778$, $nTI = 3$), 3D-encoding is feasible. As an example, assuming a TR of 0.6 s, a matrix size of $50 \times 50 \times 50$, $nTI = 2$, $BW_{Spectral} = 2778$ Hz, and 3D-elliptical encoding, CONCEPT has an acceleration factor of 31 with respect to a conventional, 3D-elliptically phase encoded MRSI sequence. The resulting measurement time is 18.4 minutes. 3D-elliptical encoding means that the number of circles decreases with the distance from the k-space center in z-direction. Although this might be slightly too long for *in-vivo* measurement of patients in clinical routine, the time can be reduced to 9 minutes by either decreasing the TR to 0.3 s, or by PI with an acceleration factor of only 2.

4.5.4 In-Vivo Comparison of Spirals, 2D-CAIPIRINHA and CONCEPT

The actual spiral trajectory consisted of 42 % rewinders, in contrast to the theoretical prediction of 31 %. Therefore, the quality factor was reduced to $\Omega_{Spiral}^{AcqEff} = \sqrt{1 - 0.42} \approx 76\%$. The SNR ratio to 2D-CAIPIRINHA was $9.0/16.0 \approx 56\%$. The most likely explanation of this difference is the bad fitting quality caused by strongly curved baselines. The same reason might explain why CONCEPT does not reach its 115 % as predicted, but rather has a poor SNR ratio of $13.0/16.0 \approx 81\%$ with respect to 2D-CAIPIRINHA. This is further indicated by the fact that the 64×64 CONCEPT and the 48×48 CONCEPT have the same median SNR, although a decrease by a factor of $\sqrt{\frac{6m20s}{8m20s}} \cdot \frac{64 \cdot 64}{48 \cdot 48} \approx 1.55$ is expected.

In addition to the higher quality factor, CONCEPT can also be used with resolutions of $200/64 \times 200/64\,\mathrm{mm}^2$ or up to $200/106 \times 200/106\,\mathrm{mm}^2$, while spiral even cannot achieve $200/64 \times 200/64\,\mathrm{mm}^2$ with the used spiral source code (with the idealized spirals of the theory section, it is possible, however). High resolutions seem to improve the curved baseline and the Glx map.

4.5.5 Refined Setting

Increasing the spectral bandwidth from 1852 to 2778 Hz improved the spectral quality by reducing the curviness of the baseline and by getting rid of the aliased lipid sideband between tNAA and tCr. Choosing a bandwidth of 1852 Hz results in an acquired spectral range of 1.6-7.8 ppm, if centered around water. The main lipid peaks fold in to the downfield (high ppms) side of the spectrum. Although this of course is artifactual, it should not pose any problem, since the downfield side of water is usually not fitted in ^1H-MRS. Nevertheless, the baseline often improved drastically, if the spectra were not centered around water, and the lipids were thus prevented from aliasing. The reason for this is unknown. The aliasing of lipids is illustrated in fig. 4.11. An additional problem causing the strong baseline distortion might be present even in the refined settings, as the metabolic maps still do not look as good as the Cartesian maps accelerated with 2D-CAIPIRINHA. Reasons could be an inaccurate density compensation, which would deteriorate the PSF, a mismatch between the theoretical and actually measured k-space trajectory, Eddy currents, or a problem in the gridding of the data.
Nevertheless, with the refined settings, SSE, especially CONCEPT was shown to have a high potential to be used as an alternative to phase encoded MRSI with PI.

4.5.6 Comparison to Literature

So far, only one article has been published in a peer-reviewed journal using a ^1H-MRS SSE method at 7T for *in-vivo* measurements of human brains (69). In this work, EPSI is used with a gradient insert with stronger gradients (maximum amplitude 80 mT/m instead of 40 mT/m) and relaxed safety constraints (slew rate of 600 mT/m/ms instead of the usual 200 mT/m/ms). This is feasible due to a dedicated head-only gradient system causing less peripheral nerve stimulation, because the gradient coils are very short. The spectral bandwidth was only 1380 Hz and the spatial resolution was only $10 \times 10\,\mathrm{mm}^2$. Why they did not have problems with such low spectral bandwidths as shown here is not known. Therefore, the used settings were less challenging for the sequence than in our case.

Furthermore, three abstracts using EPSI, rosette and CONCEPT trajectories were presented at a conference (70–72). The quality factor of the EPSI sequence of the first abstract was presumably low, because the in-plane resolution was $5.6 \times 5.6\,\mathrm{mm}^2$ with a spectral bandwidth of 2466 Hz, although it was not stated. For the rosette and CONCEPT sequences, the resolutions were only $10 \times 10\,\mathrm{mm}^2$ and $8.3 \times 8.3\,\mathrm{mm}^2$, respectively.

Only with the rosette trajectory, a J-refocused acquisition was additionally acquired with a resolution of $4 \times 4\,\mathrm{mm}^2$, however with five temporal interleaves. Again, the settings were less challenging on the sequence than our settings.

At lower magnetic fields, several different SSE methods were successfully used in MRSI. The most used sequence is EPSI (56–59), followed by spirals (60, 61), CONCEPT (5, 63), and rosettes (62, 73). Some other trajectories were proposed, but are rarely used (74, 75). In comparison to 7T, SSE at lower fields is less demanding due to the usually lower spectral bandwidths.

4.5.7 Comparison to Parallel Imaging

SSE methods provide higher acceleration factors in comparison to PI. This is no issue as long as 2D phase encoding with 1-8 slices is used, but the acceleration of PI is too low for ultra-high resolution 3D phase encoding applications. Furthermore, SSE methods do not have the problem that lipid signal is spatially aliased to central regions of the brain. As shown in this work, lipids can nevertheless be problematic, if the spectral bandwidth is too narrow. One disadvantage of SSE methods is the high stress on the gradient coils. This can cause frequency drifts and thus broadened spectral resonances, and Eddy currents. Eddy currents are one reason for a mismatch between the actual trajectory, and the theoretical, intended one.
The SSE methods used in this work were shown to result in worse spectra and metabolic maps. However, this is most probably not due to a fundamental, unchangeable reason, but is caused by a not yet considered artifact or reconstruction problem.

4.5.8 Outlook

CONCEPT can be tuned to have a Hamming k-space density, or if not enough time is available for acquiring those extra circles, the k-space density can be approximated to a Hamming filter. It further has a high enough acceleration factor to enable 3D-encoding, especially if combined with PI.
Therefore, the next steps will be to implement an algorithm into the CONCEPT sequence for adjusting the k-space density to different target densities. This can be achieved by varying the distance between consecutive circles. After that, 3D-encoding will be implemented into the sequence for improved coverage of the brain. This will be combined with a 3-dimensional elliptical filter, i.e. the maximum circle radii decrease with larger distances from the k-space center in the z-direction. As a result, only a sphere in the

three-dimensional k-space is measured. With that, clincally acceptable measurement times for 3D-encoding are feasible. Finally, approximating a target k-space density in all three dimensions could be implemented in a way that the steps between consecutive radii are varied together with the steps in k_z, which could be more efficient than varying both independently to approximate the given target density.
After all these changes, patients will be measured with the CONCEPT sequence in clinical studies to prove its feasibility in clinical routine.

5 Automatic Reconstruction Pipeline for MRSI

5.1 Motivation

Three facts motivated the programming of an own reconstruction pipeline for MRSI: First, at Siemens MR scanners (e.g. our Magnetom scanner), only MRSI data with a maximum matrix size of 32×32 can be displayed. Yet, our group is aiming for high and ultra-high resolution MRSI up to matrix sizes of 100×100. Therefore, most of our data can not be displayed at the scanner. Second, the fitting of MR spectra is very limited with the vendor provided fitting software. Therefore, the data has to be fitted offline anyway. Third, the implementation of image reconstructions directly on the scanner (so called "Image Calculation Environment (ICE) programs") is quite complicated and cumbersome, since contemporary C++ libraries can not be included easily due to the outdated C++ standard of ICE. As the fitting and display of the MRSI data had to be done offline anyway, and MATLAB programs are much faster to program, our own reconstruction pipeline for MRSI data was developed.
The need for an **automatic** pipeline stems from the fact that high resolution MRSI data without any Volume of Interest (VoI)-selection results in a very large number of spectra, in the order of thousands. Such amounts of data cannot be handled manually.

This pipeline should perform three major tasks: The MRSI data have to be pre-processed (PI reconstruction, coil combination, filtering, lipid removal), the LCModel fitting has to be started including an efficient way to control the fitting, and the fitting results have to be summarized and put into the right format for visualization.

The work described in this chapter is based on scripts written by Wolfgang Bogner, was extended during my diploma thesis, and has been further developed and adapted to our needs subsequently. The second part of the pipeline was partly programmed by my colleague Michal Považan. The whole reconstruction pipeline was presented by him

at the ISMRM 2015 in Toronto. The reconstruction pipeline is open-source, and was provided to three other sites.

5.2 Methods

In the following section, the MRSI reconstruction pipeline will be described. Most of the code was written as MATLAB scripts and functions, but these scripts and some other programs are called from BASH scripts. The reconstruction pipeline was developed for Ubuntu 12.04.3, uses BASH, and the programs Medical Image NetCDF (MINC), MATLAB, BET2 of the FMRIB Software Library (FSL) package, and LCModel. The pipeline is divided into two parts: Part 1 does everything before, and including LCModel, while part two performs the post-processing. Both parts can be called independently. Therefore, if an error occurs in part 2 due to wrong input parameters, only part 2 has to be repeated. Both parts are BASH scripts, which can be called with certain input parameters such as input paths (MRSI data, T_1-weighted images, etc.), or other parameters controlling the process. These scripts call the appropriate tools and MATLAB scripts with the user-provided input parameters. Flowcharts of part 1 and 2 are provided in figs. 5.1 and 5.2.

5.2.1 Part 1: Pre-Processing & LCModel Fitting

Housekeeping

In the beginning of part 1, some housekeeping has to be performed. A temporary folder is created for storing intermediate files. The input parameters are logged in a log file as well as all the other text output of the script (e.g. if an error occurs). The user-provided input parameters are read in, and checked for consistency. These parameters are written to a file so that MATLAB can use the same parameters. This is all done in BASH.

MINC Template & Brain Mask

After the housekeeping, the next subtask is to create a MINC template file. The MINC template saves some information such as the slice position, slice angulation, slice thickness, number of slices etc. in a small MINC file. It is used for making the process of converting raw data files to minc files as simple as possible. This process is mostly done in MATLAB. After the template construction, a brain mask is created, which marks voxels inside the brain with 1s, and voxels outside with 0s. The brain mask is created by applying the BET2 algorithm of the FSL package on a T_1-weighted image, which has to

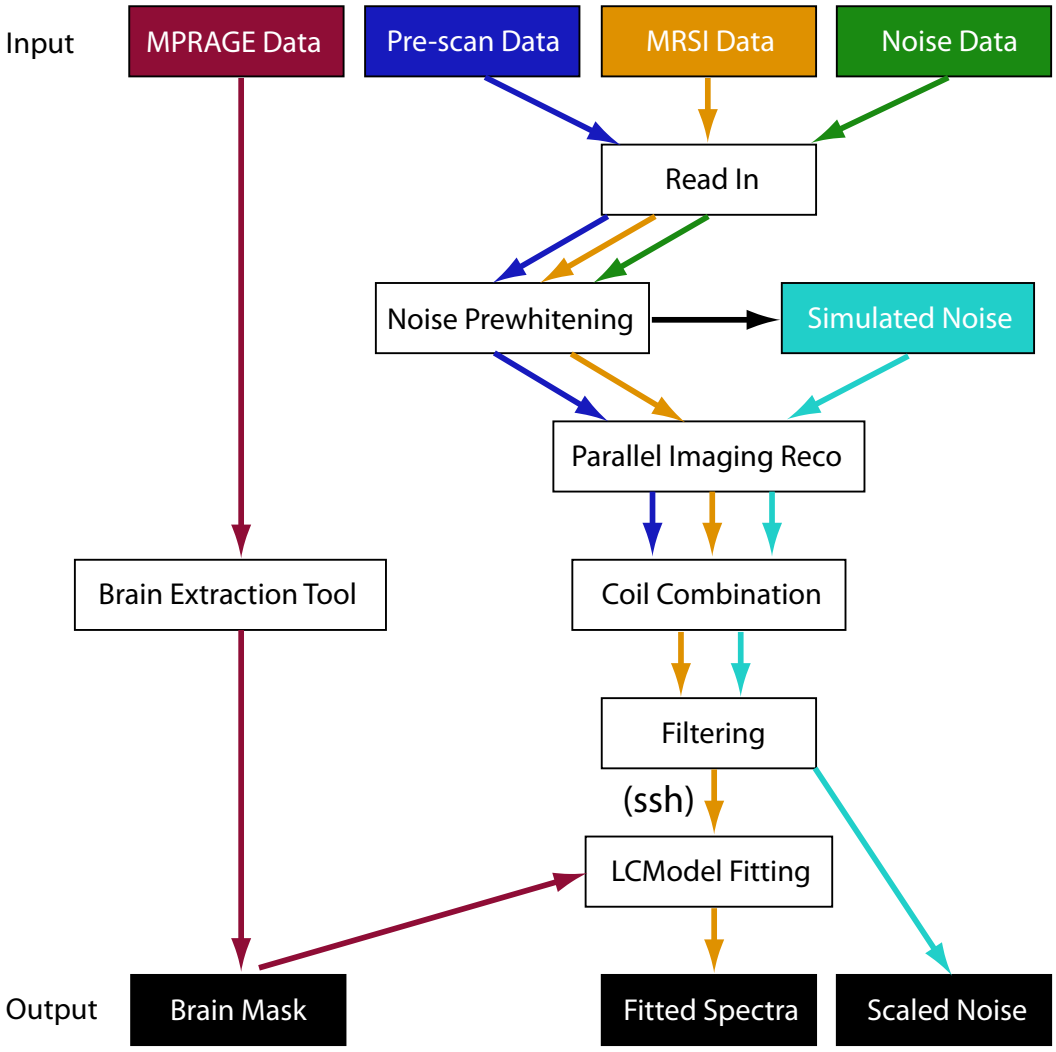

Figure 5.1: Flowchart of part 1. The BET2 program of the FSL package is used for creating a brain mask from the MPRAGE data. MRSI, pre-scan, and noise data are read in by the program. The pre-scan and MRSI data are noise pre-whitened with the aid of the noise data, and simulated noise is created. A PI reconstruction and coil combination is performed on the MRSI and simulated noise data using the pre-scan data. Next, the noise and MRSI data are filtered, e.g. with a spatial Hamming filter, and the noise data are written to a file for later usage. The voxels within the brain mask are fitted with LCModel.

be measured in addition to the MRSI data with an MPRAGE or MP2RAGE sequence. The resulting brain mask is then resampled to the same slice position and resolution as the MINC template. This process is mostly done in BASH.

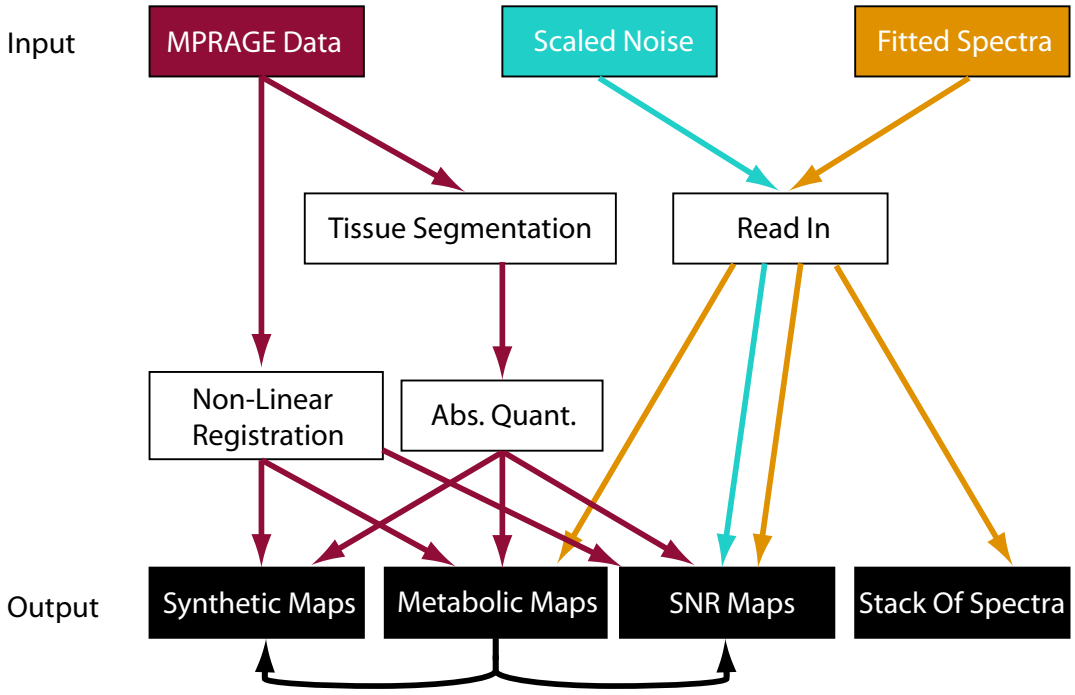

Figure 5.2: Flowchart of part 2. From the spectra fitted by LCModel (part 1), stack of spectra images are created if demanded by the user. The spectra are further used to create metabolic maps. The scaled noise, the spectra, and the metabolic maps are used to create different SNR maps with different methods, depending on the user input. The metabolic maps are additionally used for creating synthetic maps and metabolic ratio maps. Using the MPRAGE input data, a non-linear registration can be performed on all maps, e.g. for longitudinal studies. From the same data, tissue segmentation can be performed, which is used for absolute quantification. This last part has not been fully implemented yet.

Read-In of Data

Next, the MATLAB script "MRSI_Reconstruction.m" is called. In this script, all major reconstruction steps are performed. First, the MRSI data are read in. If provided, the external GRE images, the brain mask, and some noise data for noise decorrelation are read in. In case of an MRSI sequence including such pre-scans, they are read in together with the MRSI data with the function "read_csi". Because the ICE program weights the data of the individual AC channels according to the method of Brown et al. (9), even when not performing a coil combination, the MRSI data has to be read in in the "Siemens raw data format" in some cases. Therefore, the function can read in both, the standard Digital Imaging and Communications in Medicine (DICOM) file format, and the raw data format, and automatically chooses the correct sub-function for reading in

the data. Right after the read in, the GRE and MRSI data are noise decorrelated using the pre-whitening algorithm, if noise data are available.
Accompanying the read in of the data, an array comprising simulated noise with standard deviation 1 and mean 0 is created. The size of the array is the same as the MRSI data, except that the vector size is smaller. Since the MRSI data are pre-whitened, their noise also has standard deviation 1 and mean 0. If all reconstruction steps are performed exactly the same on the simulated noise as on the MRSI data, the simulated noise is an accurate representation of the noise in the MRSI data, and can thus be used for calculating the noise part in the signal to noise ratio. This method is called pseudo multiple replica method (76). In its original implementation, simulated noise was added to the raw, pre-whitened input data, the data were reconstructed, and this process was repeated several hundred times. By calculating the mean of all these reconstructions, the signal can be estimated, and the noise by calculating the standard deviation. Finally, this results in the signal to noise ratio. In my adapted version, the noise is not added to the MRSI data, because fitting every spectrum of a data set several hundred times with LCModel is very time consuming. Instead, the very same reconstruction is done on the MRSI and noise data. At the end, the standard deviation of the noise can be calculated, and the signal can be estimated by using the concentration of tNAA as estimated by LCModel.

Parallel Imaging

Next, a GRAPPA based PI reconstruction is performed on the k-space data of the MRSI and noise data. Because this part is lengthy, it is performed in its own MATLAB script, “ParallelImagingSimReco.m”, which is called by “MRSI_Reconstruction.m”.
In this script, the first step is to define the ACS data. In case of slice-PI, an additional ACS data set is necessary, and is created by FoV-shifting and summing the slices of the original ACS data. If PI should be simulated, although a full data set was acquired, the MRSI slices are summed and some of the k-space points are set to zero according to the used PI pattern.
Finally, a 2D-CAIPIRINHA reconstruction followed by a 1D-CAIPIRINHA reconstruction is performed with the MATLAB functions “opencaipirinha_MRSI” and “openslice-caipirinha_MRSI”, respectively. The data are Fourier transformed, and some images for logging, and quality assurance are created before returning back to the main script, “MRSI_Reconstruction.m”.

Coil Combination

The next pre-processing part is the coil combination. The coil combination weights are defined depending on the available input data: If a GRE pre-scan of the AC as well as of the VC is available, the sensitivity map, eq. (2.4) of chapter 2, is used as weights. If only the AC pre-scan is available, the MUSICAL weights are used according to eq. (2.5). If no GRE pre-scan is available, the Brown weights are used according to eq. (2.3). The scaling factor λ is then calculated from the weights, see eq. (2.2). Lastly, the coil combination is performed by multiplying with the weights, summing all channels of the data, and scaling them with the scaling factor. The same is applied to the noise data.

Lipid Decontamination

After the coil combination, lipid decontamination is performed, if requested by the user via an input parameter. Two different methods are available: An iterative reconstruction using an L1-norm (51), and a direct (non-iterative) reconstruction using an L2-norm (77). The user can specify the strength of the lipid decontamination with an input parameter, in case of the L1-regularization the number of iterations, and in case of the L2-regularization a regularization parameter which weights the cost function term in comparison to the data consistency term.

Both methods exploit the fact that lipid spectra are almost orthogonal to metabolite spectra in the spatial and frequency domains, $S(\vec{r}_{Lip}, \omega_{Lip}) \cdot S(\vec{r}_{Met}, \omega_{Met}) \approx 0$. In words: At spatial locations where lipids are, there are almost no metabolites and vice versa, and at spectral frequencies where lipids are, there are no metabolites and vice versa. Therefore, we can define a "lipid-only" region from the subcutaneous lipids surrounding the brain, take the spectra from there, and minimize the function

$$S_{Bilgic} = argmin_S\{||F(S) - y||_2^2 + \beta \sum_{i \in BrainMask} ||L^* \cdot S_i||_2^2\} \tag{5.1}$$

where S is the signal, F is the Fourier transform operator, $y := F(S_{orig})$, S_{orig} is the uncorrected original signal, β is a parameter weighting the cost, and L is the set of spectra containing only lipids. L is of size $P \times Q$, where P is the number of lipid voxels, and Q is the number of spectral points. * is the complex conjugate operator, and $|| \cdot ||_2$ is the L2-norm over all voxels and all frequencies. The term $L^* \cdot S_i$ calculates the dot-product between all P lipid spectra with the i'th brain spectrum, which is thus of size $Q \times 1$. The

first term of eq. (5.1) ensures data consistency, and the second term represents the cost function, penalizing reconstructions with high dot products between the lipid spectra, and the brain spectra. The L1-regularization is performed likewise.

The MATLAB functions for the regularized reconstruction were provided by Berkin Bilgic, and were slightly adapted for our purpose. The lipid mask is created using the scaling factor λ from the coil combination part, and the corresponding regularization function (L1 or L2) is called from the main script. Recently, my colleague Philipp Moser generalized the computation of the lipid mask for cases when no coil combination is performed (and therefore λ is not available).

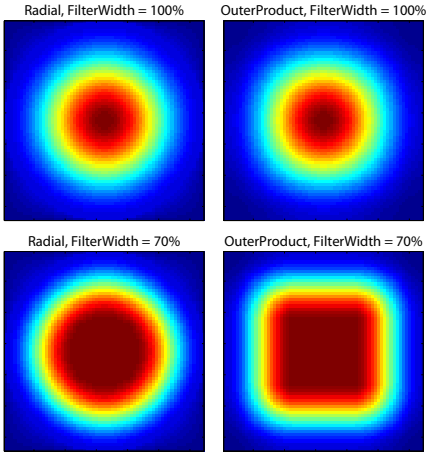

Figure 5.3: Different Hamming filters. The left filters are calculated as radial filters, i.e. a one dimensional Hamming filter is created and rotated around the axis perpendicular to the image plane. The right filters, in contrary, are created by taking the outer product between a one dimensional Hamming filter along the x-axis, and another one along the y-axis. These filters are therefore more rectangular. Another option is to apply the filters only to a certain degree as in the lower two filters, where the central parts are set to 1s, and the actual filter only starts from a certain distance from the center.

Filtering

Before the data are sent to LCModel, some filters are applied to the MRSI and noise data, if demanded by the user via input parameters. A spatial Hamming filter can be applied to the k-space data to improve the PSF. This filter can be applied in a "radial" definition, or defined as an outer product. Furthermore, the filter can be applied only to a certain degree, by setting a fixed percentage of the inner part to 1s, and then starting

with the normal filter. Different examples are shown in fig. 5.3.

A simple exponential filter can be applied on the FID of each voxel. The filter can be used as an exponential decaying function in time to increase the SNR at the cost of also broadening the spectral linewidth, or as an exponential increasing function in time for decreasing the linewdith at the cost of reducing the SNR.

Finally, a first order phase correction can be done. Since our group often acquires the FID directly, without any spin echo, the spectra have a first order phase error. This phase causes different spectral peaks to have a different phase, as shown in fig. 5.4. The correction simply applies the opposite phase to the spectrum according to eq. (5.2):

$$S_{Corr}(x, y, z, \omega) = S_{Orig}(x, y, z, \omega) \cdot \mathrm{e}^{-2\pi i \cdot T_{AD} \cdot \omega} \tag{5.2}$$

where $S_{Corr}(x, y, z, \omega)$ is the corrected MRSI data set of voxel (x, y, z) and frequency ω, S_{Orig} is the original, uncorrected data, and T_{AD} is the acquisition delay.

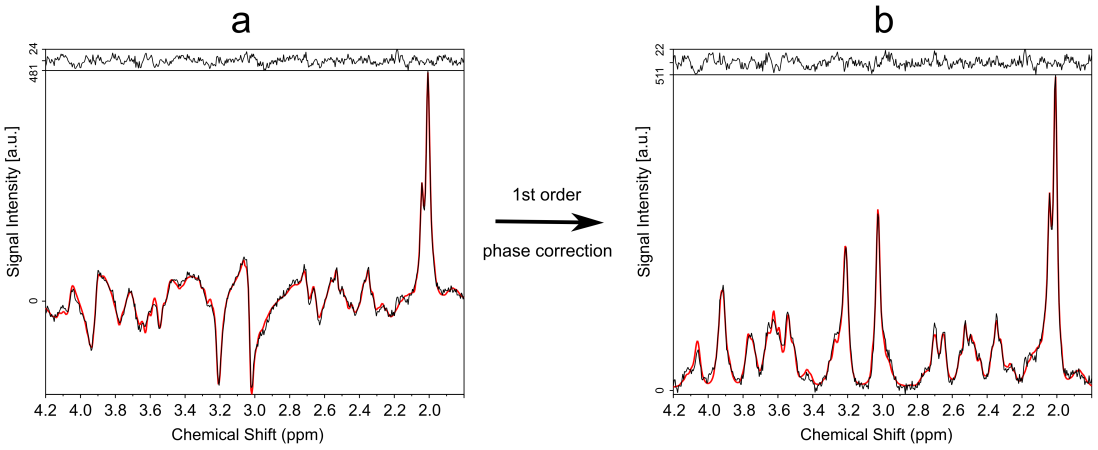

Figure 5.4: The effect of first order phase correction. If no phase correction is performed, the tNAA peak looks upwards, while the tCr and tCho peaks look downwards due to a phase linear with the frequency. The phase correction can cancel this effect, but often causes a curved baseline in the spectrum (not shown). Reprinted from: (3).

Performing such a correction results in a curved baseline in the spectrum. Although LCModel can handle this by subtracting an uneven baseline, the fitting might be slightly disturbed. Therefore, this option is mainly used for display purposes, e.g. for articles.

The standard processing is to not correct for the first order phase error, and apply the same error on the LCModel basis set spectra (15, 24).

LCModel Fitting

The last step of part 1 is to perform the LCModel fitting of the spectra. At the end of "MRSI_Reconstruction.m", the function "Write_LCM_files" is called, which writes two files for each voxel inside brain mask: A file containing the spectrum in raw format, and a file controlling the LCModel fitting ("control-file"). The content of this control-file is determined by a file which can be passed to the reconstruction pipeline via an input parameter. Therefore, the user can control the LCModel fitting by changing variables in this file.
Furthermore, the MATLAB function writes a number of BASH files, which contain nothing else than a list of calls to LCModel to process one specific spectrum, and an echo command to show how many percentages of the spectra are already processed. The number of these files determines the number of used CPU cores for the LCModel fitting.

After all these files are created, the MATLAB script "MRSI_Reconstruction.m" ends, and the calling BASH script connects to the server where LCModel is installed via Secure Shell (SSH). On this computer, all the fitting is started on several CPU cores in parallel. When all the fitting is finished, the script of part 1 ends, a log-file is written and some small housekeeping tasks are performed again.

5.2.2 Part 2: Post-Processing

In the second part, all the post-processing after the LCModel fitting is performed. This includes creating metabolic maps in MINC format, calculating the SNR, calculating different tissue contributions (gray matter, White Matter (WM), cerebrospinal fluid) for absolute quantification, and a non-linear registration for comparison in longitudinal and cross-sectional studies.

Housekeeping

In the beginning of part 2, some housekeeping is again performed: The output folders have to be created, the logging of the text output has to be started, and the input variables have to be written into a file for MATLAB usage.

Metabolic Maps

Next, the results of LCModel are read in by a MATLAB script. The metabolic ratio maps, interpolated maps, maps with excluded outliers, and maps where outliers and voxels not passing certain quality assurance criteria are calculated. Furthermore, some synthetic maps are calculated. These are linear combinations of metabolic maps as suggested by Hagberg et al. They were found by an orthonormal discriminant vector analysis of all metabolites to explain the differences between healthy volunteers, and high and low grade glioma patients (78). Two such synthetic maps were calculated as follows:

$$\begin{aligned} ODV1 = &0.4232 \cdot tNAA/tCr - 0.3116 \cdot Glx/tCr - 0.3116 \cdot MM/tCr - \\ &0.6605 \cdot tCho/tCr - 0.5348 \cdot Ins/tCr \end{aligned} \tag{5.3}$$

$$\begin{aligned} ODV2 = &0.4422 \cdot tNAA/tCr - 0.3909 \cdot Glx/tCr - 0.3909 \cdot MM/tCr + \\ &0.7321 \cdot tCho/tCr - 0.3317 \cdot Ins/tCr \end{aligned} \tag{5.4}$$

where MM are the macromolecules. The lipid ratios had to be excluded, because the quantification of lipids is unreliable with our methods, and would be strongly biased if lipid decontamination is done. Additionally, an own principal component analysis was used on our tumor and MS patients. The two eigenvectors for explaining the metabolic variations in the patients with the strongest contrast between healthy and tumor/lesion tissue were chosen. These own synthetic maps are also created in this script.

Calculate SNR

In the main MATLAB script of part 2, the SNR is calculated. Three different methods are used: Time SNR, spectral SNR, both calculated from the noise of part 1, and SNR calculated with our own script. If noise-only data were available in part 1 of the reconstruction pipeline, the spectral and temporal SNRs are calculated. For the temporal SNR, the metabolic concentrations of tNAA as fitted by LCModel is used as a signal, and the standard deviation of the time domain noise from part 1 is used as the noise. The noise is further scaled with a constant factor to take into account any scaling introduced by LCModel due to spectral integration.
For the spectral SNR, only a Fourier transform with corresponding scaling is performed on the noise. The signal component of the SNR is estimated by reading in the spectral plots of LCModel of all voxels, and calculating the maximum of this plot in the range

between $1.9 - 2.1$ ppm. If PI is used, a g-factor map is estimated with the following formula:

$$g = \frac{SNR_{Full}}{SNR_{PI} \cdot \sqrt{R}} = \frac{Signal_{Full}/Noise_{Full}}{Signal_{PI}/Noise_{PI} \cdot \sqrt{R}} \approx \frac{Noise_{PI}}{Noise_{Full} \cdot \sqrt{R}} \tag{5.5}$$

where eq. (5.5) of chapter 3 is used, and the approximation of $Signal_{Full} \approx Signal_{PI}$ is made.

The third algorithm for calculating the SNR is also performed in the spectral domain by our own MATLAB script, but directly uses the tNAA signal and the noise of each spectrum. The algorithm loops through all brain voxels, tries to find tNAA in each, and calculates the maximum of tNAA for the signal estimation. For estimating the noise, all peaks within a pre-defined spectral region are excluded. From the remaining spectral region, the standard deviation is calculated. However, this approach proved to be prone to errors, e.g. if lipid signal is close to tNAA.

At the end, all maps, including the metabolic maps, synthetic maps, and SNR maps are written to files in a raw format, and are converted to MINC format using the MINC template from part 1. This process is done in a BASH script.

Create Stack of Spectra

After creating the metabolic maps and calculating the SNR, another MATLAB script is called from BASH. This script reads all the LCModel plots of the spectra, concatenates plots within x-y-, x-z-, and y-z- planes, and saves all these projections in an image file. This is useful to directly compare the spectral quality between different regions for low matrix size data. For high matrix sizes, the spectra are usually squeezed too much to see details. This script was written by Wolfgang Bogner, and was only slightly adapted and implemented into our pipeline by me.

Calculate Tissue Contribution

In this step, the different contributions from gray matter, WM, and cerebrospinal fluid to each MRSI voxel is estimated. This is necessary for estimating the absolute concentration of metabolites. The metabolic concentration relative to water can be estimated from an MRSI scan, and an MRSI scan without water suppression. In case of MUSICAL, the scan without water suppression can be omitted. To translate this relative concentration into an absolute concentration in mol/kg, the concentration of water has to be

known. Each brain tissue type has roughly the same water concentration in different brain regions, and for different humans. Yet the water concentration differs between tissue types. Therefore, an estimate of the absolute metabolite concentration can be derived if the contributions of the different tissue types to the MRSI voxels are known.

Technically, this process is achieved by segmenting the images of an MPRAGE or MP2RAGE sequence into the different tissue types using FMRIB's Automated Segmentation Tool (FAST) of the FSL package. The resulting segmented images are then convolved with the PSF of the MRSI data, and can be used in the process of absolute quantification.
The segmentation part was written by my colleague, Michal Považan. The absolute quantification is developed by Eva Heckova.

Non-linear registration

If the same patient or volunteer needs to be measured several times in a longitudinal studies, and accurate changes between the time points need to be calculated, the metabolic images have to be translated or rotated in order to exactly match. Also, if several patients or volunteers are measured in a cross-sectional study, their metabolic maps have to be transformed into a common space, in order to be able to search for metabolic differences in certain brain regions. This is done by our pipeline with a non-linear registration between the MPRAGE image and a so called brain atlas.
To improve the results of the non-linear registration, a linear registration is first performed using the "bestlinreg_s2" method of the MINC toolkit. Then, a non-linear registration is performed from the resulting image again to the brain atlas. The transform for achieving these two registrations is then applied to all metabolic maps.
This part was programmed by Michal Považan.

5.2.3 Evaluation

The duration and the approximate memory usage of each substep of part 1 was estimated when running the reconstruction pipeline on a server with 24 Intel® Xeon® 2.66 GHz CPU cores and 94 GB RAM. This was tested on five input data sets:

1. 3D GABA-edited, $16 \times 16 \times 16$ matrix size, vector size 512, AC, no lipid decontamination, no PI, DICOM format
2. Single slice, 64×64 matrix size, vector size 2048, VC, no PI, no lipid decontamination, raw format

3. Single slice, 64×64 matrix size, vector size 2048, AC, no PI, lipid decontamination L1 with 10 iterations, raw format

4. Single slice, 64×64 matrix size, vector size 2048, AC, 2D-CAIPIRINHA with $R_{InPlane} = 4$ and $R_{Slice} = 2$, lipid decontamination L2, raw format

5. Four slices, 64×64 matrix size, vector size 2048, AC, (2+1)D-CAIPIRINHA, lipid decontamination L2, raw format.

The durations of the different substeps of part 2 were also logged when running on the same server. The memory usage was negligible, and is therefore not reported. The following data sets were used as input:

1. 3D GABA-edited, $16 \times 16 \times 16$ matrix size, 512 voxels inside brain, no SNR calculated, stack of spectra images created

2. Single slice, 64×64 matrix size, 1566 voxels inside brain, spectral and temporal SNR calculated, no stack of spectra images created

3. Single slice, 64×64 matrix size, 1566 voxels inside brain, spectral, temporal and "own-script" SNR calculated, no stack of spectra images created

4. Four slices, 64×64 matrix size, 5588 voxels inside brain, spectral amd temporal SNR calculated, no stack of spectra images created.

Several example outputs, such as stack of spectra, SNR maps or synthetic maps are further shown for different data sets.

5.3 Results

The durations and memory usages per substep of part 1 are listed in tables 5.1 and 5.2. The durations of part 2 are listed in table 5.3.
A g-factor map, and three SNR maps, from the pseudo replica method in time-domain and in the spectral domain, and calculated with our own script, are shown in fig. 5.5 for one volunteer. The two spectral methods provide quite similar SNR maps, but with the pseudo replica method having slightly higher values. The process of calculating the SNR with our own script is illustrated in fig. 5.6. Four synthetic maps are shown in fig. 5.7 together with a T_1-weighted image. The left two synthetic maps are from our own principal component analysis, showing two eigen-vectors to explain the variation in

	Reconstruction Time [s]				
Substep	Dataset1	Dataset2	Dataset3	Dataset4	Dataset5
Housekeeping	3	<1	<1	<1	<1
Creating Mask	28	30	33	30	26
Read In	5	9	224	97	510
PI Reco	-	-	-	2330	3778
Coil Combination	-	-	40	88	190
LipidDecon	-	-	20789	225	408
Filtering	1	4	4	6	14
Write LCM Files	15	24	20	35	98
LCM Fitting	79	1483	1604	3266	8191

Table 5.1: Durations of the different substeps of part 1.

	Memory Usage [GB]				
Substep	Dataset1	Dataset2	Dataset3	Dataset4	Dataset5
Housekeeping	<1	<1	<1	<1	<1
Creating Mask	<1	<1	<1	<1	<1
Read In	<1	<1	11	10	24
PI Reco	-	-	-	12	33
Coil Combination	-	-	4	5	20
LipidDecon	-	-	2	2	5
Filtering	<1	<1	<1	2	6
Write LCM Files	<1	<1	<1	1	2
LCM Fitting	<1	<1	<1	<1	<1

Table 5.2: Memory usage of the different substeps of part 1.

	Reconstruction Time [s]			
Substep	Dataset1	Dataset2	Dataset3	Dataset4
Housekeeping	3	<1	9	<1
Reading Spectra	17	27	23	86
Calculate SNR	2	112	154	482
Writing Maps	30	18	24	46
Stack Of Spectra	101	-	-	-

Table 5.3: Durations of the different substeps of part 2.

the patient data sets and which showed a contrast between tumor and healthy tissue. The second synthetic map seems to not show much contrast in this example. The right two synthetic maps are calculated according to Hagberg et al. for differentiating between healthy tissue, low-grade, and high-grade gliomas. Again, only the first map shows a contrast between the tumor and the healthy tissue. An example stack of spectra image is shown in fig. 5.8 for a GABA-edited measurement of a patient. The big peaks of negative signal amplitude are tNAA which is visible in GABA-edited spectra, while the peaks in the center of the spectra are GABA. The most-left peaks, and one of the peaks to the left of tNAA is Glutamate (Glu). With such images, the spectral quality can be assessed very fast if low-resolution data were acquired.

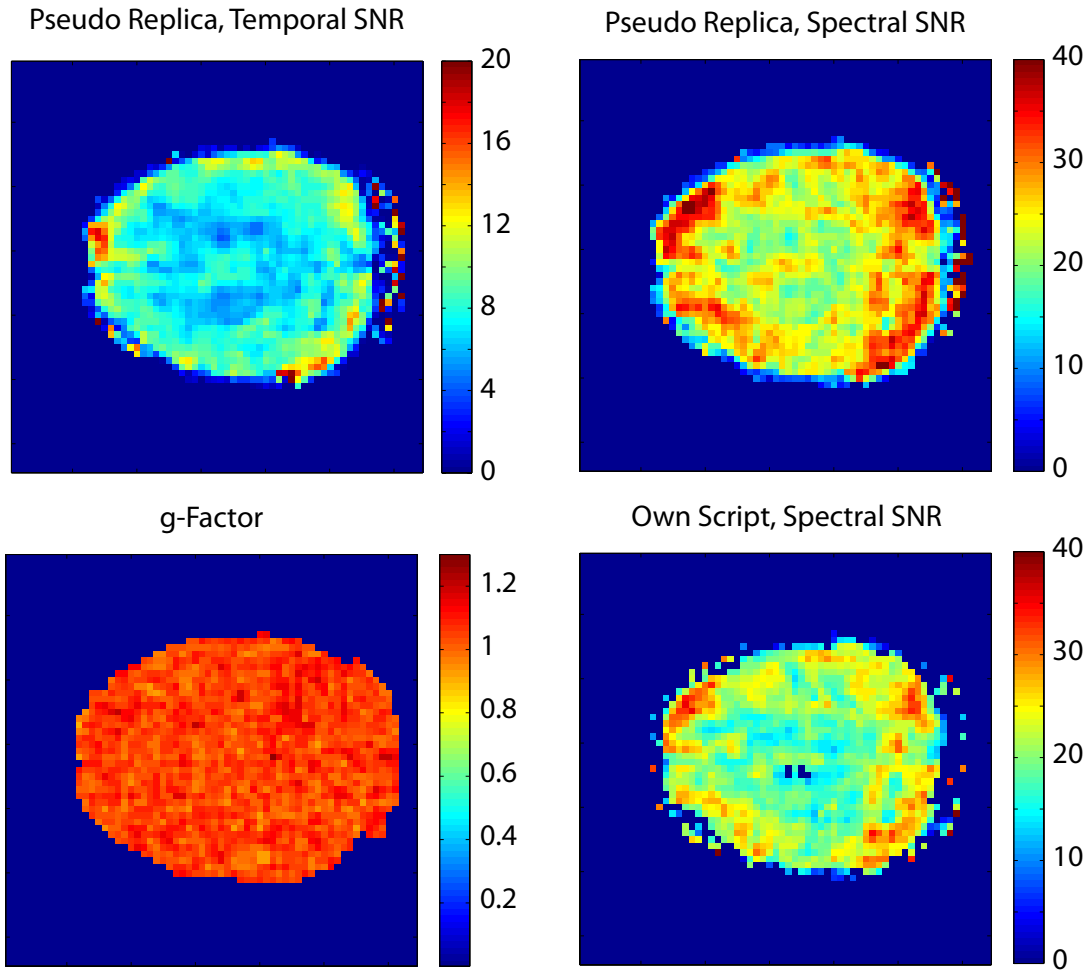

Figure 5.5: The g-factor map and the three different SNR maps that are calculated by our program. In the upper left subfigure, the temporal SNR calculated with the pseudo replica method is shown, which is calculated by the tNAA concentration as fitted by LCModel and the noise from part 1. In the upper right subfigure, the spectral SNR is shown, also calculated with the pseudo replica method, but using the spectral peak height from the LCModel plots as signal. In the lower left image, a g-factor map is shown for the same data set which was accelerated with $R_{InPlane} = 4$ and $R_{Slice} = 2$. It was calculated using eq. (5.5). In the lower right image, the SNR calculated from our own MATLAB script is shown.

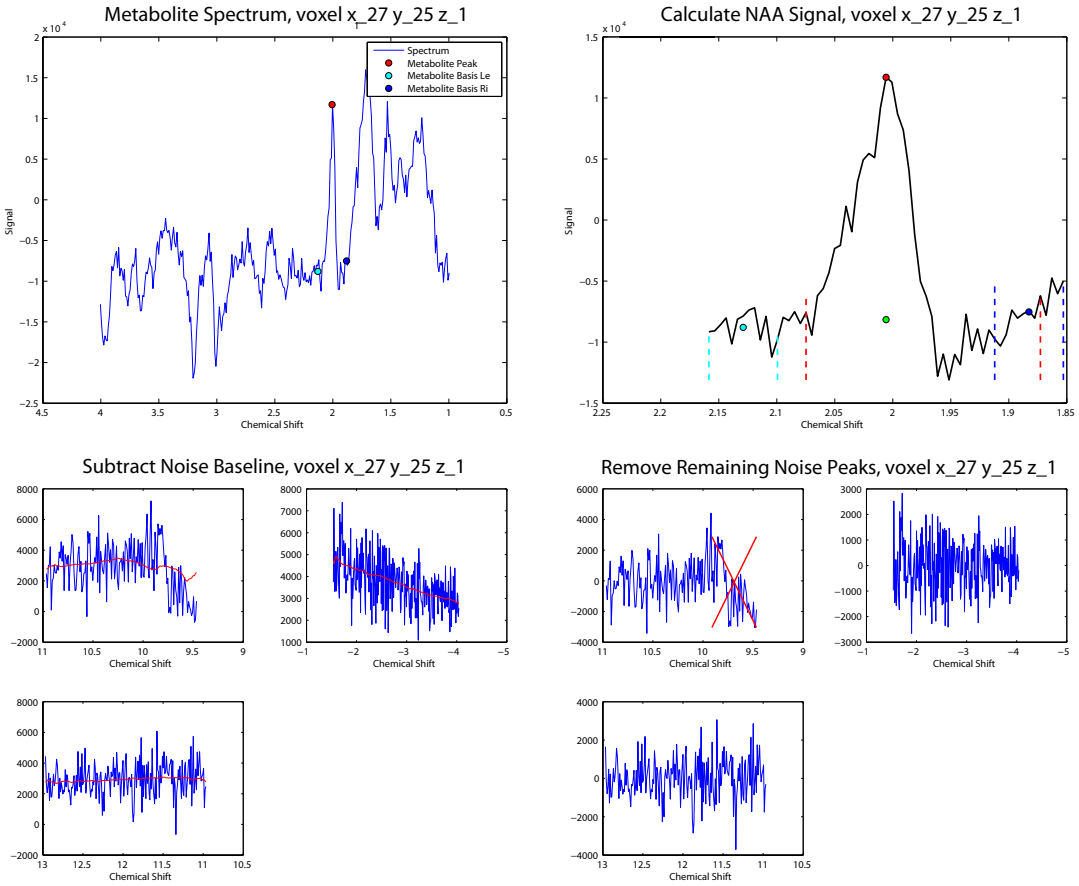

Figure 5.6: Process illustrating the SNR calculation with our own MATLAB script. Upper left: A peak is searched in a broad range around 2.01 ppm. Upper right: If a peak is found and fulfills certain criteria, the peak height of tNAA is estimated by the peak maximum, and two points at the basis of the peak. Bottom left: A baseline (red line) is fitted to the noise of all noise regions. Bottom right: After the noise baseline is subtracted, remaining peaks in the noise regions are searched and excluded. The standard deviation is calculated to obtain the SNR.

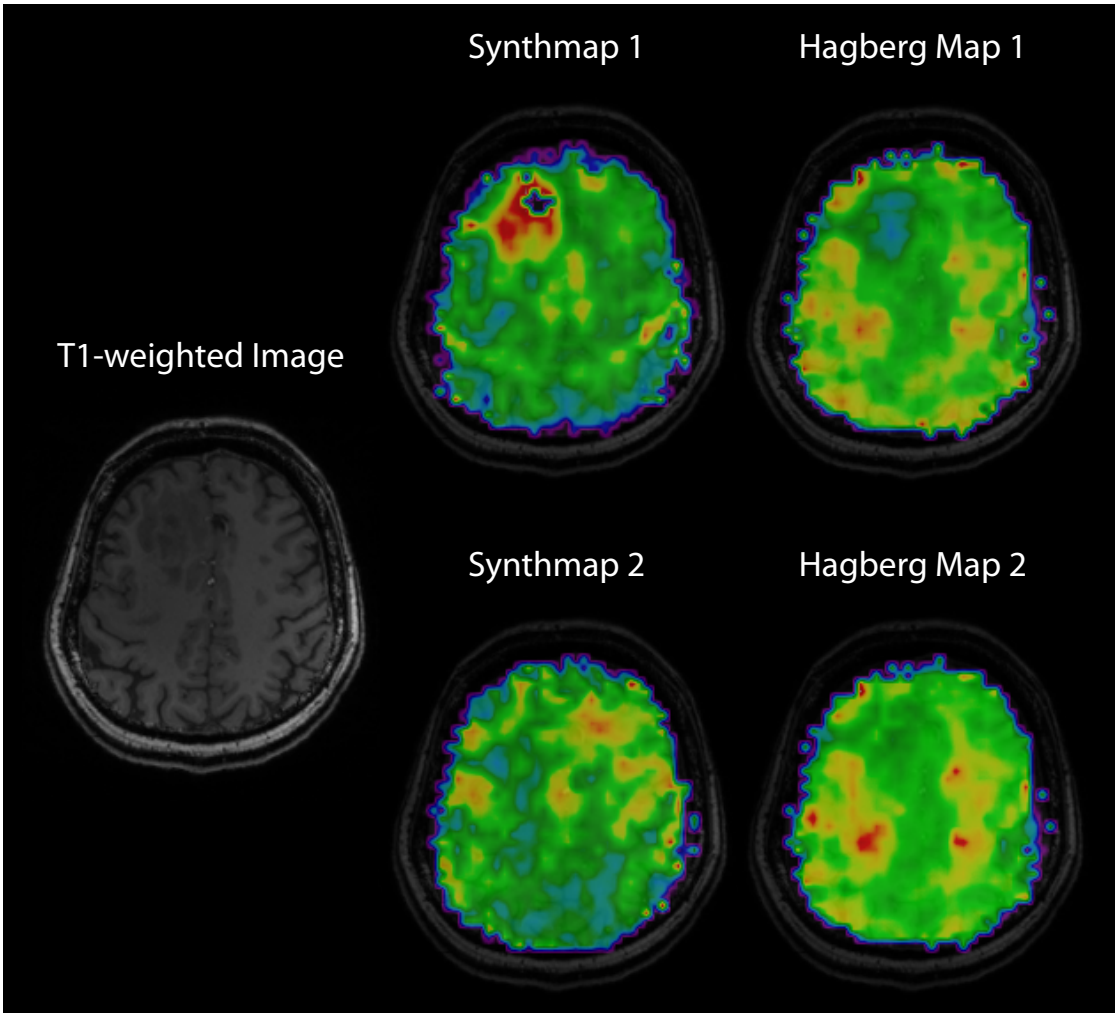

Figure 5.7: Four synthetic maps and the T_1-weighted image of a brain tumor patient. The left two synthetic maps are calculated on the basis of our own principal component analysis, while the two right maps are calculated according to Hagberg et al. for differentiating between healthy tissue, and low- and high-grade gliomas. Only in the first maps of both methods, a contrast between the tumor and healthy tissue is visible.

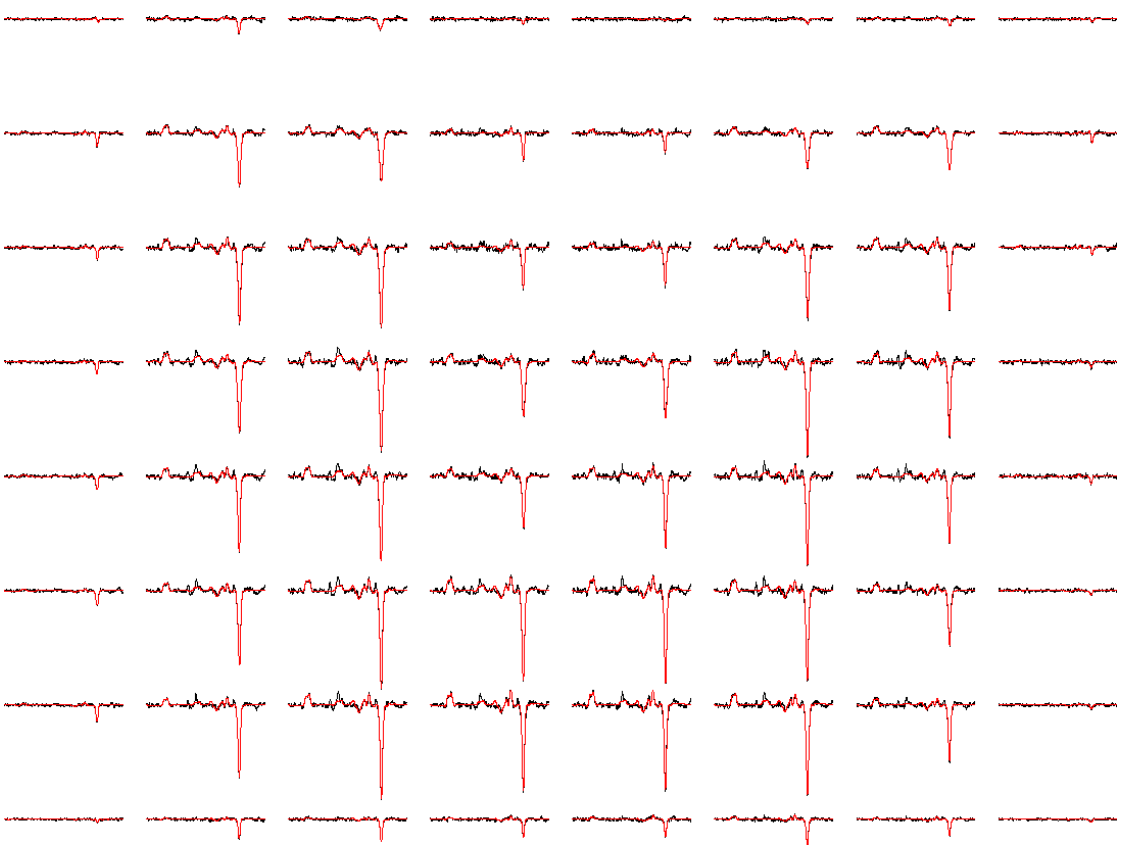

Figure 5.8: An example of a stack of spectra image output for a GABA-edited data set of a patient. With such images, the spectral quality, and the fit quality can be easily assessed for several adjacent spectra at once.

5.4 Discussion

Part 1 of our reconstruction pipeline is very CPU and memory intensive. Especially the PI reconstruction, the lipid decontamination using the L1-regularization, and the LCModel fitting take very long. The memory usage is especially high in the PI reconstruction. In part 2, only the SNR calculations take long in some cases. The memory efficiency could be increased by not processing the entire data set at a time, but performing the whole reconstruction only on parts of the data at a time, as it is done in ICE. The duration could be drastically reduced by porting the code to another language such as C++, e.g. by implementing the reconstruction into ICE.

Our reconstruction pipeline is a flexible tool with many options as illustrated by the figures of the results section. It can be readily extended with new modules, and is completely based on open-source programs, except of LCModel. Changing the pipeline to allow fitting with an open-source tool as for example with Totally Automatic Robust Quantitation in NMR (TARQUIN) (79), can be easily achieved by replacing the "Write_LCM_files" function with another one.
The fact that our reconstruction pipeline is exclusively based on command lines is a benefit and a drawback at the same time. On the one hand, processings can be readily scheduled and repeated, since scripts containing several calls to the pipeline can be saved, and called again later. On the other hand, users with little experience in BASH and programming in general might have troubles using it, or even might be scared off.

5.4.1 Comparison to Literature

Other similar reconstruction pipelines for MRSI data are available: Simpson et al. focused mostly on single voxel data (80), but they have a very similar approach otherwise. The whole pipeline is based solely on MATLAB, and does not automatically start a fitting routine. Different vendors of MR scanners provide a reconstruction pipeline, such as ICE, and fitting tools for ^1H-MRSI. The reconstruction is performed during and after the measurement, and the results can be viewed directly, or minutes after the measurement finished. This is a big advantage, but with restrictions of a maximum matrix size of 32×32, the reconstruction on the scanner has few benefits over offline-reconstruction. Moreover, the fitting tools provided by the vendors are usually quite rudimentary. The reconstruction pipeline Metabolite Imaging and Data Analysis System (MIDAS) devel-

oped by Andrew Maudsley et al. is a versatile tool (81), but is mostly tailored to the EPSI sequence.

5.4.2 Outlook

After the remaining problems with the CONCEPT sequence are solved, an additional module for reconstructing SSE data will be added before the PI module. This has been programmed already in great parts by Lukas Hingerl, but is not yet implemented into the main reconstruction pipeline. Additionally, a GUI written in MATLAB has already been programmed by Michal Považan. This might be interesting for users less experienced with BASH, and for avoiding user errors when providing lengthy paths to the program. Moreover, a third part is planned, which summarizes and condenses the output of part 2 As an example, the results of part 2 could be statistically processed, providing e.g. mean metabolic concentrations in different brain regions based on a segmentation of the MPRAGE images. Furthermore, a comparison between different measurements could be automatically calculated in part 3 (after non-linear registration to an atlas in part 2), e.g. for comparing volunteers with patients, or different measurements of the same patient. A packaged version of the reconstruction pipeline with all dependencies installed in a virtual machine, except for LCModel, is also planned for the future.

6 Application: Multiple Sclerosis Patients

6.1 Motivation

To conclude my thesis, I want to show the feasibility of using one of the developed methods in clinical studies. In this study, MS patients were measured with the 2D-CAIPIRINHA MRSI sequence. MS is an inflammatory autoimmune disease that mainly causes axons to be demyelinated in the white matter of the central nervous system, but can also affect the gray matter. Although conventional MRI can detect MS lesions, the sensitivity and specificity are usually limited and MRI has poor prognostic value for clinical disability, i.e. the lesion load of conventional MRI correlates only weakly with clinical disability (82): MRI lesions can occur without any clinical disability, and clinical disability can occur without any lesions visibile in MRI. Furthermore, the contrast of MRI lesions is not specific for the stage the lesion is in, e.g. demyelination, remyelination, or axonal loss (82). By contrast, several metabolites detectable with MRS such as NAA, Choline (Cho), Creatine (Cr), Ins, Glutathione (GSH), lactate, Glx and lipids were shown to change in some stages of the disease in comparison to the healthy population or Normal Appearing White Matter (NAWM) (82–86). Therefore, MRS has high potential in the diagnostic and neuro-scientific research of MS. MS lesions are usually rather small with 20 % below 3.5 mm in diameter (87). As a result, our high-resolution phase-encdoded MRSI sequence with a nominal resolution of $3.4 \times 3.4\,\mathrm{mm}^2$ for a 64×64 matrix, and $2.2 \times 2.2\,\mathrm{mm}^2$ for a 100×100 matrix size is very well suited for investigating MS. The work described in this chapter was presented at the annual meeting of the ISMRM 2015 in Singapore and won the price for the best abstract in the MRS study group session.

6.2 Methods

Fourteen MS patients were measured at our 7T Siemens MR scanner with a 32-channel array coil for signal reception, and a volume coil in the same housing for signal transmission. Due to motion artifacts, three data sets had to be excluded.

The sequence was the same as used in chapter 3, including a MUSICAL pre-scan for coil combination and ACS data acquisition, and the option for 2D-CAIPIRINHA acceleration. One slice with a thickness of 8 mm, a FoV of $220 \times 220\,\mathrm{mm}^2$, and a matrix size of 64×64 was acquired. The acquisition delay was 1.3 ms, the TR 600 ms. The measurement time was reduced from 30 min to 6 min by 2D-CAIPIRINHA with $R = 6$ and a VD-radius of 6. In six patients, another data set with a matrix size of 100×100, a TR of 200 ms, an acceleration factor of $R = 4$, a VD-radius of 1, and the same parameters otherwise was additionally acquired.
The missing k-space points were reconstructed with a GRAPPA-based PI reconstruction algorithm including a spatial Fourier transform as described in chapter 3. The data were coil combined with MUSICAL as described in chapter 2, Hamming filtered, lipid decontaminated using an L2-regularization as described in chapter 5, and finally, the resulting spectra were fitted with LCModel.
MS lesions were marked on Fluid-Attenuated Inversion Recovery (FLAIR) images with MINC tools (http://www.bic.mni.mcgill.ca/ServicesSoftware/MINC) at the slice position of the MRSI slice. Region of Interest (RoI)s of the same size were marked on the contra-lateral side in the NAWM. In some cases this was not possible because the contra-lateral side was also affected by the disease. RoIs at other positions were marked in these cases. For all eleven patients, the mean metabolic concentrations relative to tCr was calculated for the lesion RoIs and the NAWM RoIs, where the mean was taken over all voxels inside the RoIs. The relative increase in the lesion to the NAWM was then calculated for the metabolites GABA, Glx, tCho, GSH, Ins, and tNAA as follows:

$$RelMetInc = 100 \cdot \frac{C_{Met}^{Lesion}/C_{tCr}^{Lesion} - C_{Met}^{NAWM}/C_{tCr}^{NAWM}}{C_{Met}^{NAWM}/C_{tCr}^{NAWM}} \tag{6.1}$$

where C_{Met}^{Lesion} is the concentration of the metabolite "Met", and C_{tCr}^{Lesion}, the tCr concentration in the lesion RoIs, and C_{Met}^{NAWM} and C_{tCr}^{NAWM} the corresponding concentrations in the NAWM RoIs.
The mean and standard errors over all eleven relative metabolic increases was calculated, and a t-test was performed between the lesion and NAWM RoIs.

6.3 Results

In fig. 6.1, the tNAA map, and the ratio maps tCho/tNAA and Ins/tNAA are shown for one patient together with a T_1-weighted image of the same slice. The tNAA map shows a distinct drop, and the ratio maps show hot spots at the location of the MS-lesion (red

arrow in T_1-weighted image). Yet, another drop in tNAA is visible next to the lesion, marked by a blue arrow in the tNAA map. This might be a partial volume effect from the ventricles beneath, or could show a lesion in its developing process not yet visible in a T_1-weighted image.

Fig. 6.2 shows a patient with very large lesions around the ventricles, visible in the FLAIR image as bright spots and areas. tNAA, Ins, and Ins/tNAA maps are displayed of the same slice. Although the changes in the metabolic (ratio) maps seem to be correlated to the FLAIR image at the lesion locations, the drop in tNAA and increases in Ins and Ins/tNAA cover a larger volume than the lesions in the FLAIR image. This cannot be explained by the lower resolution of the MRSI sequence alone. Especially the Ins/tNAA shows much larger enhancements in the lower left and upper right regions of the brain. The green and red arrows in the FLAIR image indicates the positions of spectra shown in fig. 6.3. In these spectra, a strong increase of Ins is visible in the lesion spectrum in comparison to the healthy one.

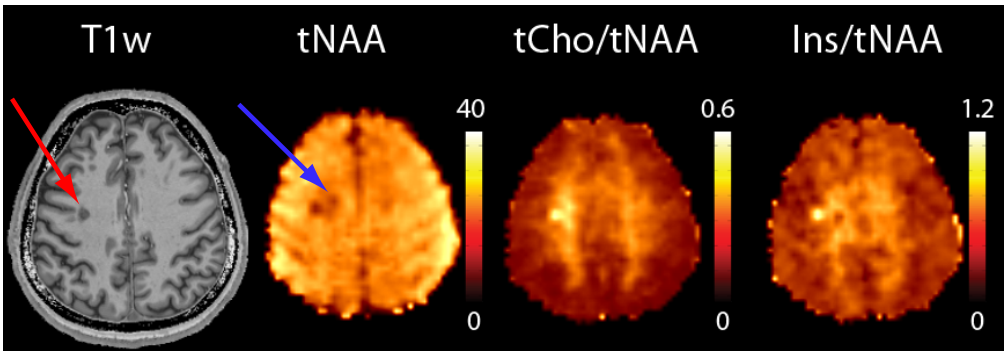

Figure 6.1: A T_1-weighted image, a tNAA map, and the ratio maps of tCho/tNAA and Ins/tNAA. The MS-lesion is shown with a red arrow in the T_1-weighted image. Drops in tNAA and hot-spots in the ratio maps are visible at the same location in the corresponding maps. Additionally, a drop in tNAA is visible close to the lesion (blue arrow), and might either stem from the underlying ventricles, or show a lesion in its development.

In figs. 6.4 and 6.5, a third patient is shown with large MS lesions in the white matter of both hemispheres. The lesions in the FLAIR image are well correlated with increases in Ins/tNAA, tCho/tNAA, and tCho, and a decrease in tNAA. The region marked by an arrow in the tCho map, which is decreased in contrast to the other regions of the lesion, is low in all metabolic maps. This indicates scar tissue.

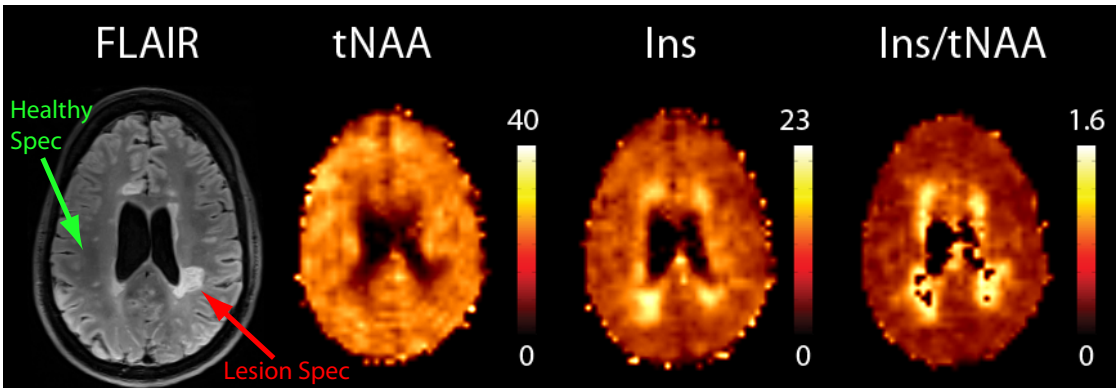

Figure 6.2: A FLAIR image of the same slice position as tNAA, Ins, and Ins/tNAA maps. Large lesions around the ventricles are visible in the FLAIR image, but regions of lower (tNAA) and increased signal (Ins, Ins/tNAA) are even larger in the metabolic (ratio) maps. Green and red arrows indicate the position of a "healthy" and a "lesion" spectrum, respectively, shown in fig. 6.3.

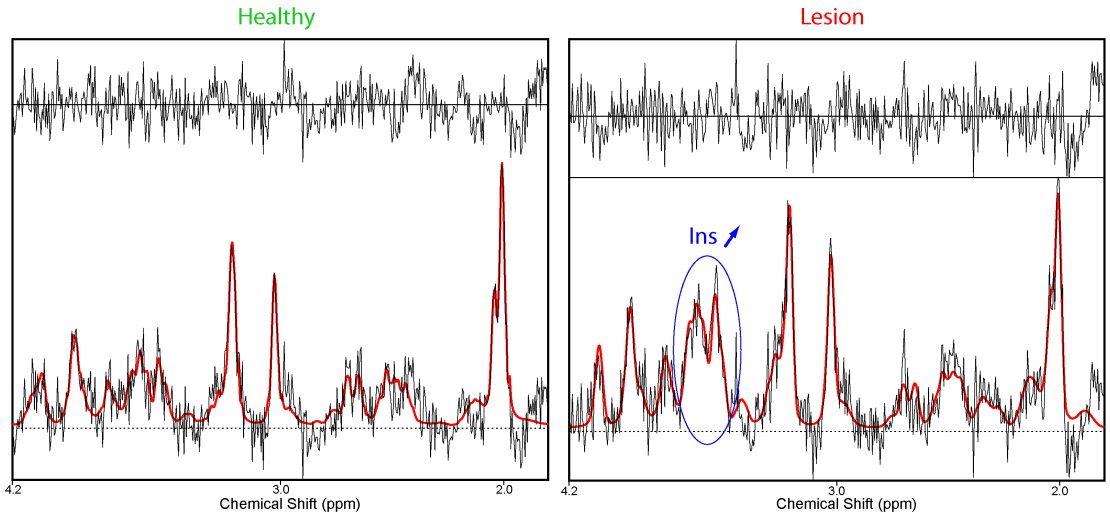

Figure 6.3: Two spectra from the locations marked in fig. 6.2. The spectrum from the lesion has a strongly increased Ins in comparison to the spectrum from NAWM.

Fig. 6.6 depicts another patient where the tCho/tNAA, and especially the Ins/tNAA have larger enhanced regions than in the FLAIR image. The arrows mark the healthy and affected regions of the spectra of fig. 6.7. In these spectra, a strong increase in Ins and tCho is visible, while tNAA is decreased in comparison to the spectrum from the healthy region.

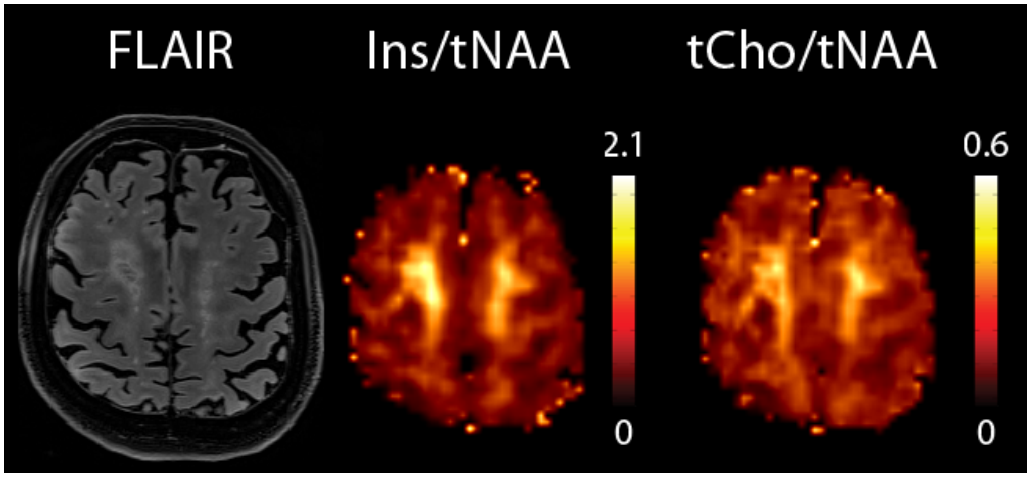

Figure 6.4: FLAIR image and Ins/tNAA, and tCho/tNAA metabolic ratio maps of the third patient. The signal increases in the ratio maps show a good correspondence with the lesions in the FLAIR image, but seem to be larger.

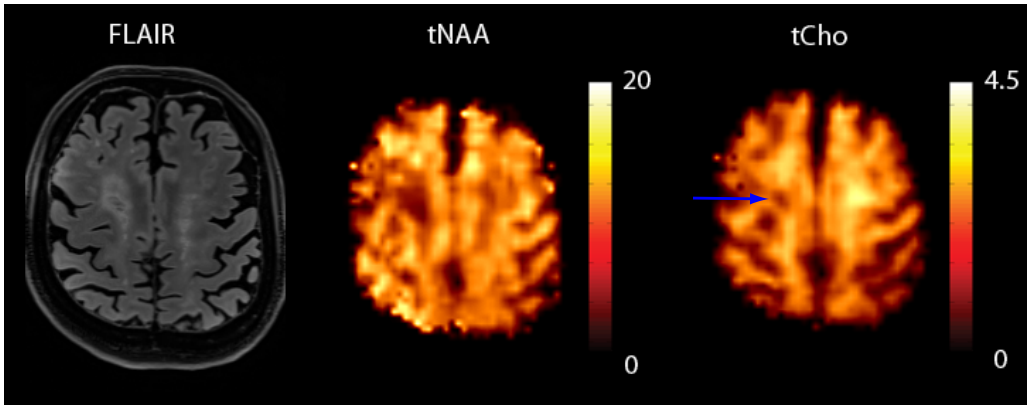

Figure 6.5: FLAIR image and tCho, and tNAA metabolic maps of the third patient. The tNAA map shows a signal drop at the lesion locations, while tCho increases, except for the region marked with an arrow. In this region, all metabolic maps show a signal drop, which thus indicates scar tissue.

Fig. 6.8 also shows an example where the alterations on the Ins/tNAA, tCho/tNAA, but especially on the Glx maps have higher volumes than in the FLAIR image. The Glx map shows a strong drop in the white matter on the left side of the map. The two ratio maps show a very strong hot-spot on the left lesion area. From this area, a lesion spectrum is shown in fig. 6.9 (red arrow) and compared to a spectrum from a NAWM region (green arrow). In the lesion spectrum, a very strong increase of Ins, tCho, and an extreme decrease in tNAA is visible.

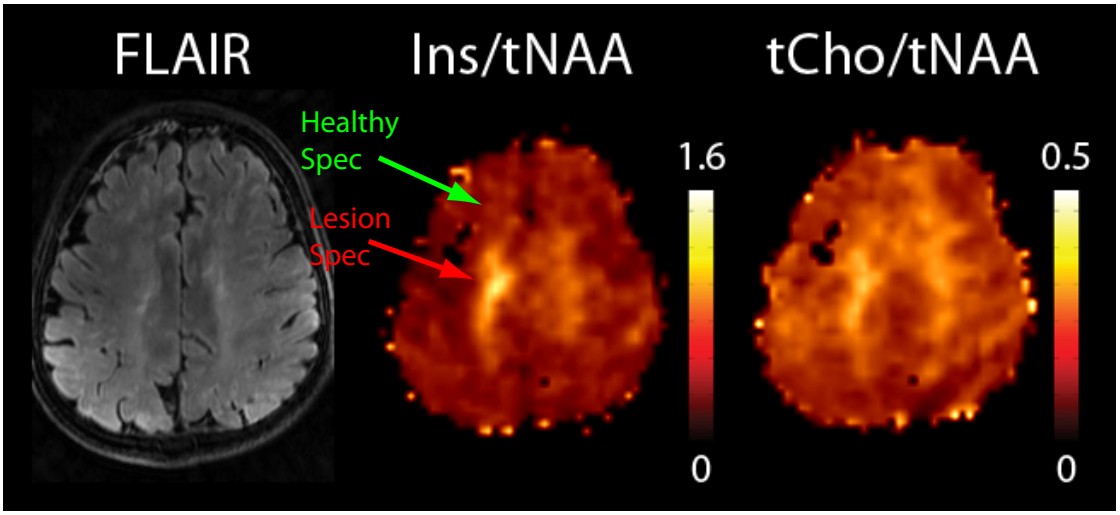

Figure 6.6: Ins/tNAA and tCho/tNAA ratio maps together with a FLAIR image of the same slice. The metabolic ratio maps show alterations of a larger volume than the lesions on the FLAIR image. The green and red arrows show the spectra locations of fig. 6.7.

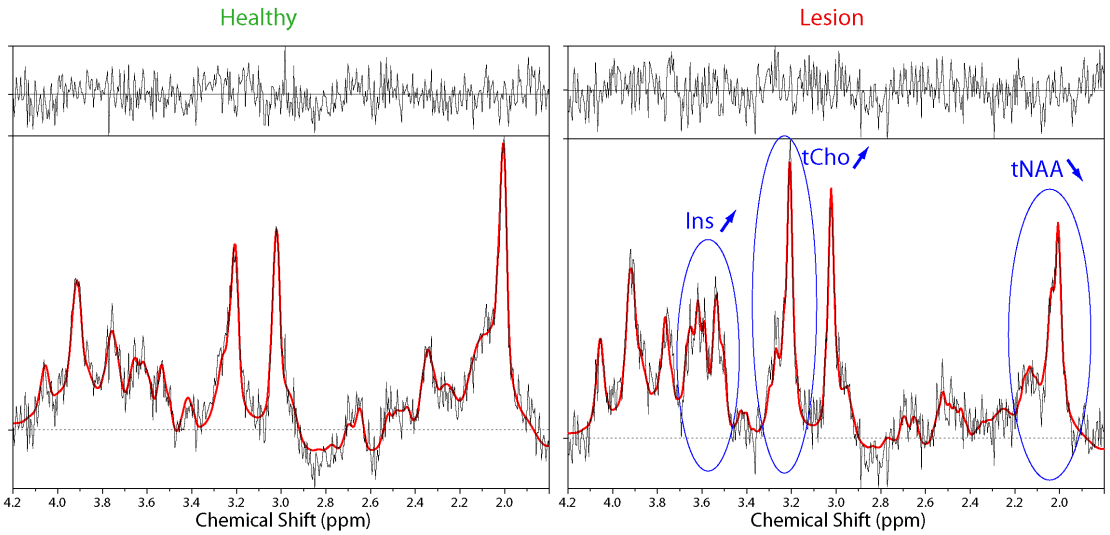

Figure 6.7: Comparison of a spectrum from a healthy region in comparison to one of a lesion as indicated by arrows in fig. 6.6. The lesion spectrum displays increased Ins and tCho, while tNAA is slightly decreased in comparison to the healthy reference spectrum.

Finally, fig. 6.10 shows the last patient example, where a tNAA map of a 64×64 matrix size, with a voxel size of $3.4 \times 3.4\,\mathrm{mm}^2$ is compared against a tNAA map of a 100×100 matrix size with a voxel size of $2.2 \times 2.2\,\mathrm{mm}^2$. Although the higher resolution map looks more noisy, the lesions marked by blue and green arrows are only visible on the higher resolution map, and on the FLAIR image, but not on the 64×64 tNAA map. Thus, this

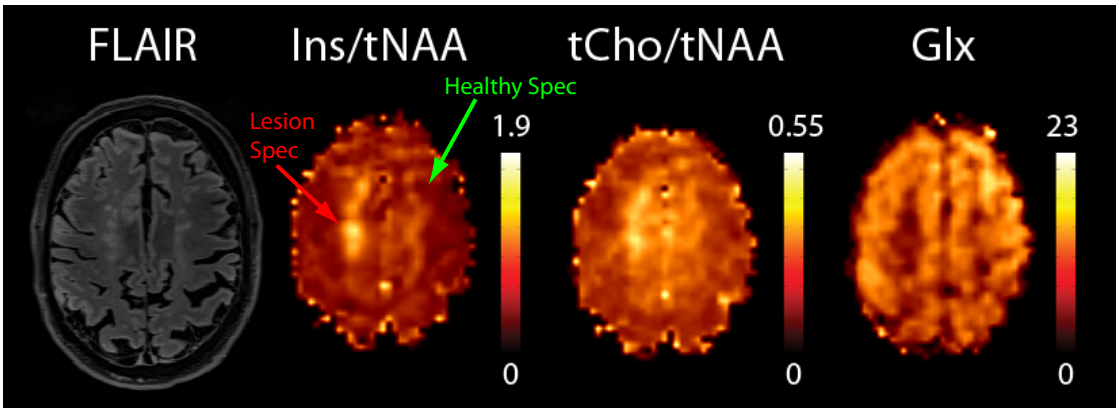

Figure 6.8: FLAIR, Ins/tNAA, tCho/tNAA, and Glx maps of patient 5. The metabolic alterations are larger than the lesion regions in the FLAIR image. Especially the Glx map has a strong decrease at the location of the left lesion region in comparison to the contra-lateral side. Arrows indicate the positions of the spectra of fig. 6.9.

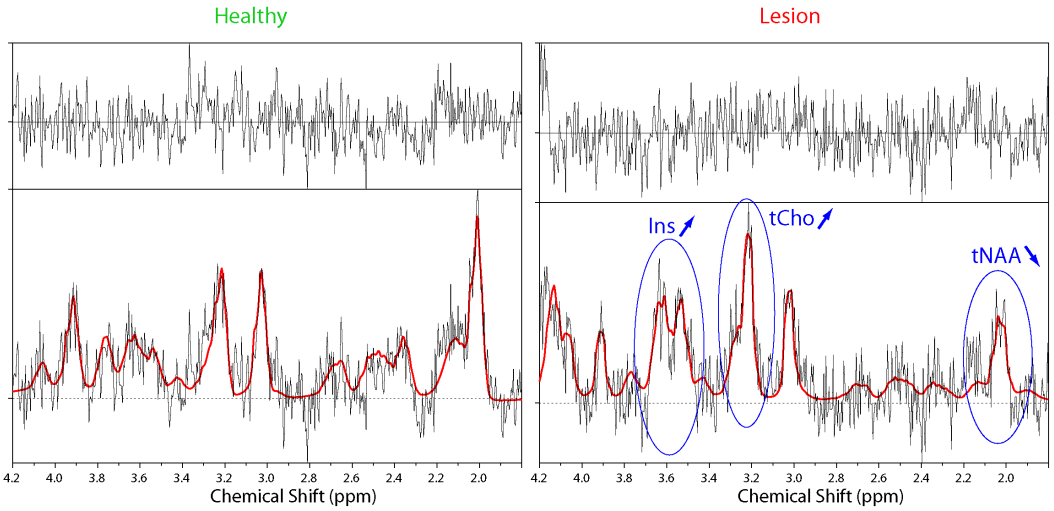

Figure 6.9: Comparison of the spectra from NAWM and a lesion of patient 5, as indicated by the arrows in fig. 6.8. The lesion spectrum shows a highly increased Ins, and tCho, and an extreme decrease of tNAA so that it is barely detectable.

is an example where even the high resolution of $3.4 \times 3.4\,\mathrm{mm}^2$ of our MRSI sequence is not enough for resolving small MS lesions.

In order to get a feeling how much variability in the metabolic maps occurs in healthy volunteers, fig. 6.11 depicts the Ins/tNAA, tCho/tNAA and the Glx (ratio) maps of a healthy volunteer.

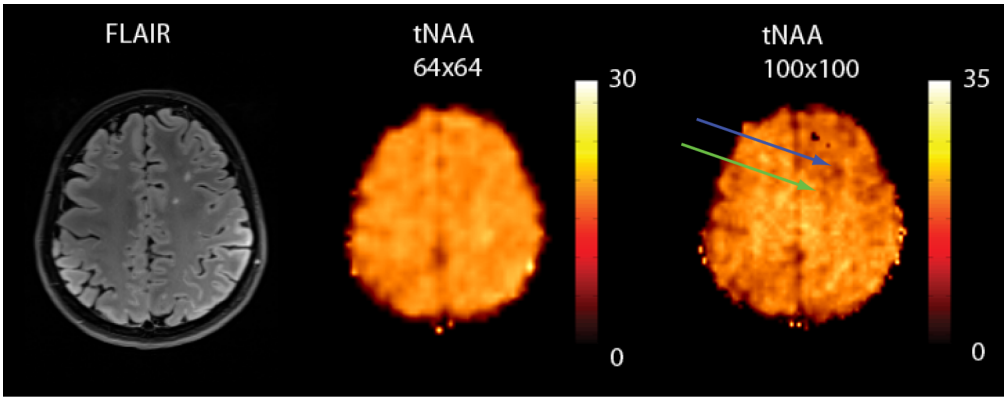

Figure 6.10: A FLAIR image and two tNAA maps, one from a high resolution ($3.4 \times 3.4\,\mathrm{mm}^2$ nominal resolution), and one from an ultra-high resolution ($2.2 \times 2.2\,\mathrm{mm}^2$ nominal resolution). The two small MS lesions are visible on the FLAIR image, as well as on the ultra-high resolution tNAA map, but not on the high resolution map.

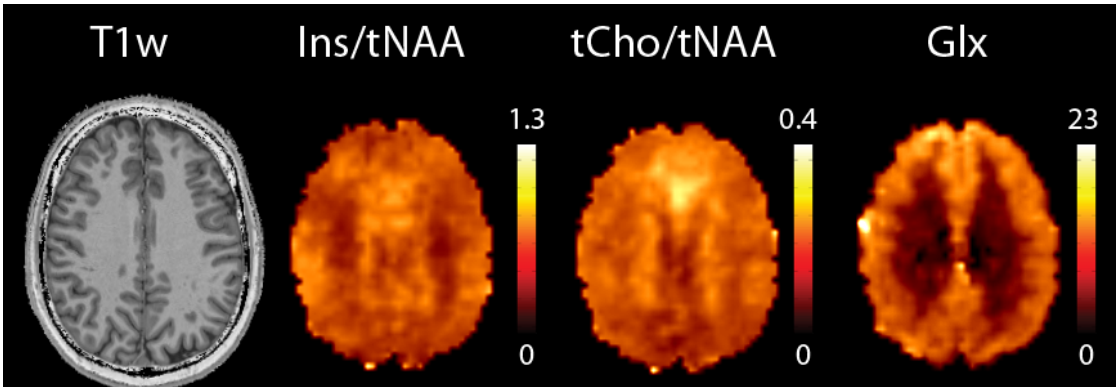

Figure 6.11: The metabolic (ratio) maps of Ins/tNAA, tCho/tNAA and Glx together with a T_1-weighted image illustrate the appearance of the maps in healthy volunteers.

The relative mean increases of the different metabolites, calculated according to eq. (6.1) are given in table 6.1. * denotes p-values below 0.05, while ** denotes highly significant differences with $p < 0.005$. tNAA/tCr, and Glx/tCr significantly decreased in lesion RoIs, while Ins/tCr significantly and strongly increased. tNAA/tCr was decreased in every single patient in the lesion RoI in comparison to the NAWM RoI, and Ins/tCr was increased in every patient, without exception. Glx/tCr was decreased in nine patients, and slightly increased in only two. The other metabolites, tCho/tCr, GABA/tCr, and GSH/tCr did not change significantly. Also tCr did not change significantly ($p > 0.6$).

Metabolite	Mean [%]	Standard Error [%]
Ins/tCr	+44.6**	6.3
tNAA/tCr	-23.3**	4.0
Glx/tCr	-24.2*	8.4
tCho/tCr	+6.0	5.4
GABA/tCr	-4	15
GSH/tCr	+39	30

Table 6.1: Relative increases of metabolic ratios to tCr between lesion and NAWM RoIs according to eq. (6.1). Ins/tCr increased strongly and highly significantly, while tNAA/tCr and Glx/tCr decreased significantly. The other metabolic ratios did not change significantly.

6.4 Discussion

A significant decrease of Glx/tCr and tNAA/tCr, and a significant increase in Ins/tCr was found in this study. Especially tNAA/tCr and Ins/tCr were changed in every patient in the lesion RoI in comparison to the NAWM RoI, but also Glx/tCr was increased in only two patients, and otherwise decreased. Therefore, these changes seem to be very reliable. Since tCr did not change significantly, its use as the reference in the metabolic ratios is justified. The other three tested metabolic ratios, tCho/tCr, GABA/tCr, and GSH/tCr did not change significantly. However, this does not mean that they are not changed between lesions and NAWM. GABA, and GSH could not be fitted reliably enough in all patients to detect small changes. Although tCho/tCr was not altered significantly, it varied a lot between patients. A possible explanation would be that tCho changes differently in different stages of the disease or that the tCho enhancements do not always coincide with the FLAIR-visible lesions. Since the patient group was not homogeneous in this study, this could explain the non-significant results of tCho.

In our study, the changes in the metabolic maps mostly covered larger areas than the FLAIR images. Partly, this can be attributed to the lower resolution of the MRSI sequence, but this can not explain the whole volume increase. Thus, the large affected volume could indicate that the inflammation in MS occurs in larger volumes than usually reported, and lesions on the FLAIR images only occur on spots where changes exceed a certain threshold. With these assumptions, the clinico-radiological paradox in MS could be explained, which says that MS lesions visible in MRI can develop without clinical dysfunction, and clinical dysfunction can develop without MS lesions visible in MRI. MS lesions could occur at hot-spots, but with most WM being unaffected, resulting in

lesions visible in MRI with a low clinical disability. On the other hand, a large volume could be affected by MS causing strong clinical disabilities, but with only a few spots exceeding the threshold to develop a lesion or may develop a T_2-visible lesion at a later time point.

6.4.1 Comparison to Literature

Our findings are partially in accordance with literature results. Bitsch et al., Srinivasan et al., and Narayana et al. found a decrease in NAA, and the latter two additionally found an increase in Ins (83, 84, 86). Glu was reported to increase by (83), in contrast to our results of decreasing Glx. Cho was reported to increase by Bitsch et al., while Srinivasan et al. and Narayana et al. reported Cho to be increased in acute lesions in comparison to chronic ones (83, 84, 86). These findings could explain our mixed results for tCho. A differentiation between lesion states in our study would clarify this matter. Finally, Srinivasan et al. and Choi et al. found a decrease of GSH in MS patients in comparison to controls (85, 88).

In contrast to other studies of MRS in MS, we used a very short acquisition delay of only 1.3 ms. This improves the detection of J-coupled metabolites, such as Glx, or Ins. Furthermore, we used a very high resolution in comparison to other studies. If only a single voxel is acquired, as in some studies, metabolic information is usually confined to MS lesions visible on conventional MRI, and contra-lateral NAWM. Detecting metabolic alterations surrounding the lesions, as detected in our study, is thus not possible. In contrast to voxel sizes of about $7 - 10\,\mathrm{mm}^2$, as usually used, our high resolution MRSI allows the detection of very small MS lesions.

6.4.2 Outlook

The MRSI methods developed by our group, as partially described in this thesis, can be used in a larger study for measuring clinically isolated syndrome patients. These patients partially have the symptoms of MS patients, but do not fulfill all the criteria of clinically definite MS, nor do their MRI images show lesions. 30 - 70 % of these patients develop MS later (89). If metabolic changes were specific to MS, and these were found before an MRI lesion is visible, the MS-specific medication could start earlier. This might improve the outcome of the treatment for those patients.
Moreover, such findings might be useful for the scientific understanding of MS by giving

hints of the sequence of metabolic changes that finally lead to lesion formation. With that, a step towards understanding the cause of MS might be done.

Bibliography

[1] R. W. Brown, Y. C. N. Cheng, E. M. Haacke, M. R. Thompson, and R. Venkatesan. *Magnetic Resonance Imaging: Principles, Physical Design, Sequence*. John Wiley & Sons Ltd, Chichester, UK, apr 2014.

[2] R. A. de Graaf. *In Vivo NMR Spectroscopy*. John Wiley & Sons, Ltd, Chichester, oct 2007.

[3] B. Strasser, M. Chmelik, S. D. Robinson, G. Hangel, S. Gruber, S. Trattnig, and W. Bogner. Coil combination of multichannel MRSI data at 7 T: MUSICAL. *NMR in biomedicine*, 26(12):1796–805, dec 2013.

[4] C. B. Ahn, J. H. Kim, and Z. H. Cho. High-speed spiral-scan echo planar NMR imaging-I. *IEEE transactions on medical imaging*, 5(1):2–7, 1986.

[5] J. K. Furuyama, N. E. Wilson, and M. A. Thomas. Spectroscopic imaging using concentrically circular echo-planar trajectories in vivo. *Magnetic resonance in medicine*, 67(6):1515–22, jun 2012.

[6] D. D. Traficante. Time averaging. Does the noise really average toward zero? *Concepts in Magnetic Resonance*, 3(2):83–87, apr 1991.

[7] R. Pohmann, M. von Kienlin, and A. Haase. Theoretical evaluation and comparison of fast chemical shift imaging methods. *Journal of magnetic resonance (San Diego, Calif. : 1997)*, 129(2):145–60, dec 1997.

[8] P. B. Roemer, W. a. Edelstein, C. E. Hayes, S. P. Souza, and O. M. Mueller. The NMR phased array. *Magnetic resonance in medicine*, 16(2):192–225, nov 1990.

[9] M. A. Brown. Time-domain combination of MR spectroscopy data acquired using phased-array coils. *Magnetic Resonance in Medicine*, 52(5):1207–1213, nov 2004.

[10] T. Prock, D. J. Collins, a. S. K. Dzik-Jurasz, and M. O. Leach. An algorithm for the optimum combination of data from arbitrary magnetic resonance phased array probes. *Physics in medicine and biology*, 47(2):N39–46, jan 2002.

[11] N. Maril and R. E. Lenkinski. An automated algorithm for combining multivoxel MRS data acquired with phased-array coils. *Journal of magnetic resonance imaging : JMRI*, 21(3):317–22, mar 2005.

[12] T. Schäffter, P. Börnert, C. Leussler, I. C. Carlsen, and D. Leibfritz. Fast 1H spectroscopic imaging using a multi-element head-coil array. *Magnetic resonance in medicine*, 40(2):185–93, aug 1998.

[13] O. Natt, V. Bezkorovaynyy, T. Michaelis, and J. Frahm. Use of phased array coils for a determination of absolute metabolite concentrations. *Magnetic Resonance in Medicine*, 53(1):3–8, jan 2005.

[14] R. J. Ogg, P. B. Kingsley, and J. S. Taylor. WET, a T1- and B1-insensitive water-suppression method for in vivo localized 1H NMR spectroscopy. *Journal of magnetic resonance. Series B*, 104(1):1–10, may 1994.

[15] A. Henning, A. Fuchs, J. B. Murdoch, and P. Boesiger. Slice-selective FID acquisition, localized by outer volume suppression (FIDLOVS) for (1)H-MRSI of the human brain at 7 T with minimal signal loss. *NMR in biomedicine*, 22(7):683–96, aug 2009.

[16] L. L. Wald, S. E. Moyher, M. R. Day, S. J. Nelson, and D. B. Vigneron. Proton Spectroscopic Imaging of the Human Brain Using Phased-Array Detectors. *Magnetic Resonance in Medicine*, 34(3):440–445, sep 1995.

[17] K. P. Pruessmann, M. Weiger, P. Börnert, and P. Boesiger. Advances in sensitivity encoding with arbitrary k-space trajectories. *Magnetic resonance in medicine*, 46(4):638–51, oct 2001.

[18] N. Martini, M. F. Santarelli, G. Giovannetti, M. Milanesi, D. De Marchi, V. Positano, and L. Landini. Noise correlations and SNR in phased-array MRS. *NMR in biomedicine*, 23(1):66–73, jan 2010.

[19] Y. Qian, T. Zhao, G. C. Wiggins, L. L. Wald, H. Zheng, J. Weimer, and F. E. Boada. Sodium imaging of human brain at 7 T with 15-channel array coil. *Magnetic Resonance in Medicine*, 68(6):1808–1814, dec 2012.

[20] S. M. Wright and L. L. Wald. Theory and application of array coils in MR spectroscopy. *NMR in biomedicine*, 10(8):394–410, dec 1997.

[21] Z. Dong and B. Peterson. The rapid and automatic combination of proton MRSI data using multi-channel coils without water suppression. *Magnetic resonance imaging*, 25(8):1148–54, oct 2007.

[22] G. L. Chadzynski and U. Klose. Chemical shift imaging without water suppression at 3 T. *Magnetic Resonance Imaging*, 28(5):669–675, 2010.

[23] N. Avdievich, J. Pan, J. Baehring, D. Spencer, and H. Hetherington. Short echo spectroscopic imaging of the human brain at 7T using transceiver arrays. *Magnetic Resonance in Medicine*, 62(1):17–25, jul 2009.

[24] W. Bogner, S. Gruber, S. Trattnig, and M. Chmelik. High-resolution mapping of human brain metabolites by free induction decay (1)H MRSI at 7 T. *NMR in biomedicine*, 25(6):873–82, jun 2012.

[25] F. H. Lin, S. Y. Tsai, R. Otazo, A. Caprihan, L. L. Wald, J. W. Belliveau, and S. Posse. Sensitivity-encoded (SENSE) proton echo-planar spectroscopic imaging (PEPSI) in the human brain. *Magnetic Resonance in Medicine*, 57(2):249–257, feb 2007.

[26] R. Otazo, S. Y. Tsai, F. H. Lin, and S. Posse. Accelerated short-TE 3D proton echo-planar spectroscopic imaging using 2D-SENSE with a 32-channel array coil. *Magnetic Resonance in Medicine*, 58(6):1107–1116, dec 2007.

[27] S. Posse, R. Otazo, S.-Y. Tsai, A. E. Yoshimoto, and F.-H. Lin. Single-shot magnetic resonance spectroscopic imaging with partial parallel imaging. *Magnetic Resonance in Medicine*, 61(3):541–547, mar 2009.

[28] U. Dydak, K. P. Pruessmann, M. Weiger, J. Tsao, D. Meier, and P. Boesiger. Parallel spectroscopic imaging with spin-echo trains. *Magnetic Resonance in Medicine*, 50(1):196–200, jul 2003.

[29] D. Mayer, D. H. Kim, D. M. Spielman, and R. Bammer. Fast parallel spiral chemical shift imaging at 3T using iterative SENSE reconstruction. *Magnetic Resonance in Medicine*, 59(4):891–897, apr 2008.

[30] U. Dydak, M. Weiger, K. P. Pruessmann, D. Meier, and P. Boesiger. Sensitivity-encoded spectroscopic imaging. *Magnetic Resonance in Medicine*, 46(4):713–722, oct 2001.

[31] E. Ozturk-Isik, A. P. Chen, J. C. Crane, W. Bian, D. Xu, E. T. Han, S. M. Chang, D. B. Vigneron, and S. J. Nelson. 3D sensitivity encoded ellipsoidal MR spectroscopic imaging of gliomas at 3T. *Magnetic resonance imaging*, 27(9):1249–57, nov 2009.

[32] X. Zhao, R. W. Frost, Z. Li, and S. J. Li. Reduction of artifacts by optimization of the sensitivity map in sensitivity-encoded spectroscopic imagine. *Magnetic Resonance in Medicine*, 53(1):30–34, jan 2005.

[33] J. Sánchez-González, J. Tsao, U. Dydak, M. Desco, P. Boesiger, and K. P. Pruessmann. Minimum-norm reconstruction for sensitivity-encoded magnetic resonance spectroscopic imaging. *Magnetic Resonance in Medicine*, 55(2):287–295, feb 2006.

[34] D. Bonekamp, M. a. Smith, H. Zhu, and P. B. Barker. Quantitative SENSE-MRSI of the human brain. *Magnetic resonance imaging*, 28(3):305–13, apr 2010.

[35] T. Kirchner, A. Fillmer, J. Tsao, K. P. Pruessmann, and A. Henning. Reduction of voxel bleeding in highly accelerated parallel 1 H MRSI by direct control of the spatial response function. *Magnetic Resonance in Medicine*, 73(2):469–480, feb 2015.

[36] S. Banerjee, E. Ozturk-Isik, S. J. Nelson, and S. Majumdar. Elliptical magnetic resonance spectroscopic imaging with GRAPPA for imaging brain tumors at 3 T. *Magnetic resonance imaging*, 27(10):1319–25, dec 2009.

[37] M. Gu, C. Liu, and D. M. Spielman. Parallel spectroscopic imaging reconstruction with arbitrary trajectories using k-space sparse matrices. *Magnetic Resonance in Medicine*, 61(2):267–272, feb 2009.

[38] M. L. Zierhut, E. Ozturk-Isik, A. P. Chen, I. Park, D. B. Vigneron, and S. J. Nelson. (1)H spectroscopic imaging of human brain at 3 Tesla: comparison of fast three-dimensional magnetic resonance spectroscopic imaging techniques. *Journal of magnetic resonance imaging : JMRI*, 30(3):473–80, sep 2009.

[39] M. Sabati, J. Zhan, V. Govind, K. L. Arheart, and A. a. Maudsley. Impact of reduced k-space acquisition on pathologic detectability for volumetric MR spectroscopic imaging. *Journal of magnetic resonance imaging : JMRI*, 39(1):224–34, jan 2014.

[40] S. Y. Tsai, R. Otazo, S. Posse, Y. R. Lin, H. W. Chung, L. L. Wald, G. C. Wiggins, and F. H. Lin. Accelerated proton echo planar spectroscopic imaging (PEPSI) using GRAPPA with a 32-channel phased-array coil. *Magnetic Resonance in Medicine*, 59(5):989–998, may 2008.

[41] X. Zhu, A. Ebel, J. X. Ji, and N. Schuff. Spectral phase-corrected GRAPPA reconstruction of three-dimensional echo-planar spectroscopic imaging (3D-EPSI). *Magnetic Resonance in Medicine*, 57(5):815–820, may 2007.

[42] B. Strasser, M. Považan, G. Hangel, L. Hingerl, M. Chmelik, S. Gruber, S. Trattnig, and W. Bogner. (2+1)D-CAIPIRINHA Accelerated MR Spectroscopic Imaging of the Brain at 7 T. *Magnetic Resonance in Medicine [details will be added in proofing]*, 00:1–12, 2016.

[43] M. A. Griswold, P. M. Jakob, R. M. Heidemann, M. Nittka, V. Jellus, J. Wang, B. Kiefer, and A. Haase. Generalized Autocalibrating Partially Parallel Acquisitions (GRAPPA). *Magnetic Resonance in Medicine*, 47(6):1202–1210, jun 2002.

[44] K. P. Pruessmann, M. Weiger, M. B. Scheidegger, and P. Boesiger. SENSE: sensitivity encoding for fast MRI. *Magnetic resonance in medicine*, 42(5):952–62, nov 1999.

[45] F. a. Breuer, M. Blaimer, M. F. Mueller, N. Seiberlich, R. M. Heidemann, M. a. Griswold, and P. M. Jakob. Controlled aliasing in volumetric parallel imaging (2D CAIPIRINHA). *Magnetic resonance in medicine*, 55(3):549–56, mar 2006.

[46] F. A. Breuer, M. Blaimer, R. M. Heidemann, M. F. Mueller, M. A. Griswold, and P. M. Jakob. Controlled aliasing in parallel imaging results in higher acceleration (CAIPIRINHA) for multi-slice imaging. *Magnetic Resonance in Medicine*, 53(3):684–691, mar 2005.

[47] J. P. Marques, T. Kober, G. Krueger, W. van der Zwaag, P.-F. Van de Moortele, and R. Gruetter. MP2RAGE, a self bias-field corrected sequence for improved segmentation and T1-mapping at high field. *NeuroImage*, 49(2):1271–81, jan 2010.

[48] U. Klose. Mapping of the radio frequency magnetic field with a MR snapshot FLASH technique. *Medical physics*, 19(4):1099–104, 1992.

[49] S. Chung, D. Kim, E. Breton, and L. Axel. Rapid B1+ mapping using a preconditioning RF pulse with turboFLASH readout. *Magnetic Resonance in Medicine*, 64(2):439–446, aug 2010.

[50] O. Cohen, A. Tal, and O. Gonen. Three-dimensional hadamard-encoded proton spectroscopic imaging in the human brain using time-cascaded pulses at 3 tesla. *Magnetic Resonance in Medicine*, 72(4):923–933, nov 2014.

[51] B. Bilgic, B. Gagoski, T. Kok, and E. Adalsteinsson. Lipid suppression in CSI with spatial priors and highly undersampled peripheral k-space. *Magnetic Resonance in Medicine*, 69(6):1501–1511, jun 2013.

[52] L. Kasper, M. Haeberlin, B. E. Dietrich, S. Gross, C. Barmet, B. J. Wilm, S. J. Vannesjo, D. O. Brunner, C. C. Ruff, K. E. Stephan, and K. P. Pruessmann. Matched-filter acquisition for BOLD fMRI. *NeuroImage*, 100:145–60, oct 2014.

[53] F. A. Breuer, H. Moriguchi, N. Seiberlich, M. Blaimer, P. M. Jakob, J. L. Duerk, and M. A. Griswold. Zigzag sampling for improved parallel imaging. *Magnetic Resonance in Medicine*, 60(2):474–478, aug 2008.

[54] B. Bilgic, B. A. Gagoski, S. F. Cauley, A. P. Fan, J. R. Polimeni, P. E. Grant, L. L. Wald, and K. Setsompop. Wave-CAIPI for highly accelerated 3D imaging. *Magnetic resonance in medicine*, 73(6):2152–62, jun 2015.

[55] D. G. Norris, P. J. Koopmans, R. Boyacioğlu, and M. Barth. Power Independent of Number of Slices (PINS) radiofrequency pulses for low-power simultaneous multislice excitation. *Magnetic resonance in medicine*, 66(5):1234–40, nov 2011.

[56] S. Posse, G. Tedeschi, R. Risinger, R. Ogg, and D. Le Bihan. High speed 1H spectroscopic imaging in human brain by echo planar spatial-spectral encoding. *Magnetic resonance in medicine*, 33(1):34–40, jan 1995.

[57] A. Maudsley, C. Domenig, V. Govind, A. Darkazanli, C. Studholme, K. Arheart, and C. Bloomer. Mapping of brain metabolite distributions by volumetric proton MR spectroscopic imaging (MRSI). *Magnetic Resonance in Medicine*, 61(3):548–559, mar 2009.

[58] R. Eslami and M. Jacob. Robust reconstruction of MRSI data using a sparse spectral model and high resolution MRI priors. *IEEE transactions on medical imaging*, 29(6):1297–309, jun 2010.

[59] Z. Iqbal, N. E. Wilson, and M. A. Thomas. 3D spatially encoded and accelerated TE-averaged echo planar spectroscopic imaging in healthy human brain. *NMR in Biomedicine*, 29(3):329–339, 2016.

[60] E. Adalsteinsson, P. Irarrazabal, S. Topp, C. Meyer, A. Macovski, and D. M. Spielman. Volumetric spectroscopic imaging with spiral-based k-space trajectories. *Magnetic Resonance in Medicine*, 39(6):889–898, jun 1998.

[61] W. Bogner, A. T. Hess, B. Gagoski, M. D. Tisdall, A. J. W. van der Kouwe, S. Trattnig, B. Rosen, and O. C. Andronesi. Real-time motion- and B0-correction for LASER-localized spiral-accelerated 3D-MRSI of the brain at 3T. *NeuroImage*, 88C:22–31, nov 2013.

[62] C. V. Schirda, T. Zhao, O. C. Andronesi, Y. Lee, J. W. Pan, J. M. Mountz, H. P. Hetherington, and F. E. Boada. In vivo brain rosette spectroscopic imaging (RSI) with LASER excitation, constant gradient strength readout, and automated LCModel quantification for all voxels. *Magnetic resonance in medicine*, 76(2):380–90, aug 2016.

[63] W. Jiang, M. Lustig, and P. E. Z. Larson. Concentric rings K-space trajectory for hyperpolarized 13C MR spectroscopic imaging. *Magnetic Resonance in Medicine*, 75(1):19–31, dec 2016.

[64] B. A. Gagoski. Magnetic Resonance Spectroscopic Imaging using Parallel Transmission at 7T. *PhD Thesis, Massachusetts Institute of Technology*, 2011.

[65] O. C. Andronesi, B. A. Gagoski, and A. G. Sorensen. Neurologic 3D MR spectroscopic imaging with low-power adiabatic pulses and fast spiral acquisition. *Radiology*, 262(2):647–61, feb 2012.

[66] K. L. Wright, J. I. Hamilton, M. a. Griswold, V. Gulani, and N. Seiberlich. Non-Cartesian parallel imaging reconstruction. *Journal of magnetic resonance imaging : JMRI*, 40(5):1022–40, nov 2014.

[67] M. E. Ravicz, J. R. Melcher, and N. Y. Kiang. Acoustic noise during functional magnetic resonance imaging. *The Journal of the Acoustical Society of America*, 108(4):1683–1696, 2000.

[68] R. Pohmann and M. Von Kienlin. Accurate phosphorus metabolite images of the human heart by 3D acquisition-weighted CSI. *Magnetic Resonance in Medicine*, 45(5):817–826, 2001.

[69] R. Otazo, B. Mueller, K. Ugurbil, L. Wald, and S. Posse. Signal-to-noise ratio and spectral linewidth improvements between 1.5 and 7 tesla in proton echo-planar spectroscopic imaging. *Magnetic Resonance in Medicine*, 56(6):1200–1210, dec 2006.

[70] K. Snoussi, J. S. Gillen, M. Schär, R. A. E. Edden, A. A. Maudsley, and P. B. Barker. Adapting volumetric 1H echo-planar spectroscopic imaging of the human brain from 3 to 7 Tesla. In *Proc. Intl. Soc. Mag. Reson. Med. 23 (2015) 0428.*, 2015.

[71] N. Wilson, H. Hariharan, A. M. Thomas, and R. Reddy. Concentrically circular echo planar spectroscopic imaging at 3T and 7T with partial temporal interleaving. In *Proc. Intl. Soc. Mag. Reson. Med. 24 (2016) 2352.*, 2016.

[72] C. Schirda, T. Zhao, H. Hetherington, V. Yushmanov, and J. Pan. Rosette Spectroscopic Imaging (RSI) of human brain at 7T. In *Proc. Intl. Soc. Mag. Reson. Med. 24 (2016) 2351.*, 2016.

[73] E. K. Bucholz, J. Song, G. A. Johnson, and I. Hancu. Multispectral imaging with three-dimensional rosette trajectories. *Magnetic Resonance in Medicine*, 59(3):581–589, mar 2008.

[74] E. Adalsteinsson, P. Irarrazabal, D. M. Spielman, and A. Macovski. Three-dimensional spectroscopic imaging with time-varying gradients. *Magnetic resonance in medicine*, 33(4):461–6, apr 1995.

[75] B. Hiba, B. Faure, L. Lamalle, M. Décorps, and A. Ziegler. Out-and-In Spiral Spectroscopic Imaging in Rat Brain at 7 T. *Magnetic Resonance in Medicine*, 50(6):1127–1133, dec 2003.

[76] P. M. Robson, A. K. Grant, A. J. Madhuranthakam, R. Lattanzi, D. K. Sodickson, and C. A. McKenzie. Comprehensive quantification of signal-to-noise ratio and g-factor for image-based and k-space-based parallel imaging reconstructions. *Magnetic Resonance in Medicine*, 60(4):895–907, oct 2008.

[77] B. Bilgic, I. Chatnuntawech, A. P. Fan, K. Setsompop, S. F. Cauley, L. L. Wald, and E. Adalsteinsson. Fast image reconstruction with L2-regularization. *Journal of magnetic resonance imaging : JMRI*, 40(1):181–91, jul 2014.

[78] G. Hagberg, A. P. Burlina, I. Mader, W. Roser, E. W. Radue, and J. Seelig. In Vivo proton MR spectroscopy of human gliomas: definition of metabolic coordinates for multi-dimensional classification. *Magnetic Resonance in Medicine*, 34(2):242–252, aug 1995.

[79] M. Wilson, G. Reynolds, R. A. Kauppinen, T. N. Arvanitis, and A. C. Peet. A Constrained Least-Squares Approach to the Automated Quantitation of In Vivo (1)H Magnetic Resonance Spectroscopy Data. *Magnetic Resonance in Medicine*, 65(1):1–12, 2011.

[80] R. Simpson, G. A. Devenyi, P. Jezzard, T. J. Hennessy, and J. Near. Advanced processing and simulation of MRS data using the FID appliance (FID-A)-An open source, MATLAB-based toolkit. *Magnetic Resonance in Medicine*, 77(1):23–33, jan 2017.

[81] A. A. Maudsley, A. Darkazanli, J. R. Alger, L. O. Hall, N. Schuff, C. Studholme, Y. Yu, A. Ebel, A. Frew, D. Goldgof, Y. Gu, R. Pagare, F. Rousseau, K. Sivasankaran, B. J. Soher, P. Weber, K. Young, and X. Zhu. Comprehensive processing, display

and analysis for in vivo MR spectroscopic imaging. *NMR in biomedicine*, 19(4):492–503, jun 2006.

[82] P. A. Narayana. Magnetic Resonance Spectroscopy in the Monitoring of Multiple Sclerosis. *Journal of Neuroimaging*, 15(4 Suppl):46S–57S, oct 2005.

[83] R. Srinivasan, N. Sailasuta, R. Hurd, S. Nelson, and D. Pelletier. Evidence of elevated glutamate in multiple sclerosis using magnetic resonance spectroscopy at 3 T. *Brain*, 128(5):1016–1025, 2005.

[84] A. Bitsch, H. Bruhn, V. Vougioukas, A. Stringaris, H. Lassmann, J. Frahm, and W. Brück. Inflammatory CNS demyelination: Histopathologic correlation with in vivo quantitative proton MR spectroscopy. *American Journal of Neuroradiology*, 20(9):1619–1627, 1999.

[85] C. Choi, S. Ghose, J. Uh, A. Patel, I. E. Dimitrov, H. Lu, D. Douglas, and S. Ganji. Measurement of N-acetylaspartylglutamate in the human frontal brain by 1H-MRS at 7 T. *Magnetic resonance in medicine*, 64(5):1247–51, nov 2010.

[86] P. A. Narayana, T. J. Doyle, D. Lai, and J. S. Wolinsky. Serial proton magnetic resonance spectroscopic imaging, contrast-enhanced magnetic resonance imaging, and quantitative lesion volumetry in multiple sclerosis. *Annals of neurology*, 43(1):56–71, jan 1998.

[87] L. Wang, H.-M. Lai, A. J. Thompson, and D. H. Miller. Survey of the distribution of lesion size in multiple sclerosis: implication for the measurement of total lesion load. *Journal of Neurology, Neurosurgery & Psychiatry*, 63(4):452–455, 1997.

[88] R. Srinivasan, H. Ratiney, K. E. Hammond-Rosenbluth, D. Pelletier, and S. J. Nelson. MR spectroscopic imaging of glutathione in the white and gray matter at 7 T with an application to multiple sclerosis. *Magnetic resonance imaging*, 28(2):163–70, feb 2010.

[89] D. Miller, F. Barkhof, X. Montalban, A. Thompson, and M. Filippi. Clinically isolated syndromes suggestive of multiple sclerosis, part I: Natural history, pathogenesis, diagnosis, and prognosis. *Lancet Neurology*, 4(5):281–288, 2005.

Bernhard Strasser

Curriculum Vitae

Personal Data

Address:	Schulgasse 12/10, 1180 Vienna
E-Mail:	Bernhard.strasser@meduniwien.ac.at
Date of Birth:	26/05/1987
Place of Birth:	Salzburg
Citizenship:	Austria

Work Experience

Samariterbund Salzburg
Civilian Service Employee
2005 – 2006

Medical University of Vienna
Scientific Associate
06.2012 – present

Education

Higher School Certificate, passed with merit
July, 2005

Diploma studies in physics at the University of Vienna
2006 – 2012

Conferment of Mag. rer. nat. (Master's Degree)
April, 2012

PhD studies "Dr.-Studium der techn. Wissenschaften Technische Physik" at Technical University of Vienna
2012 – 2017

Languages

German – Mother Tongue
English – Proficient
Italian – Basic

Interests

Biking, Music, Programming, Neuroscience, Philosophy, Maths

Publications

Strasser B, Chmelik M, Robinson SD, Hangel G, Gruber S, Trattnig S, Bogner W. Coil combination of multichannel MRSI data at 7 T: MUSICAL. NMR in biomedicine. 2013; 26(12):1796-805.

Bogner W, Gagoski B, Hess AT, Bhat H, Tisdall MD, van der Kouwe AJ, **Strasser B**, Marjańska M, Trattnig S, Grant E, Rosen B, Andronesi OC. 3D GABA imaging with real-time motion correction, shim update and reacquisition of adiabatic spiral MRSI. NeuroImage. 2014; 103:290-302.

Navarro de Lara LI, Windischberger C, Kuehne A, Woletz M, Sieg J, Bestmann S, Weiskopf N, **Strasser B**, Moser E, Laistler E. A novel coil array for combined TMS/fMRI experiments at 3 T. Magnetic resonance in medicine. 2015; 74(5):1492-501.

Považan M, Hangel G, **Strasser B**, Gruber S, Chmelik M, Trattnig S, Bogner W. Mapping of brain macromolecules and their use for spectral processing of (1)H-MRSI data with an ultra-short acquisition delay at 7 T. NeuroImage. 2015; 121:126-35.

Hangel G, **Strasser B**, Považan M, Gruber S, Chmelík M, Gajdošík M, Trattnig S, Bogner W. Lipid suppression via double inversion recovery with symmetric frequency sweep for robust 2D-GRAPPA-accelerated MRSI of the brain at 7 T. NMR in biomedicine. 2015; 28(11):1413-25.

Gruber S, Minarikova L, Pinker K, Zaric O, Chmelik M, **Strasser B**, Baltzer P, Helbich T, Trattnig S, Bogner W. Diffusion-weighted imaging of breast tumours at 3 Tesla and 7 Tesla: a comparison. European radiology. 2016; 26(5):1466-73.

Zaric O, Pinker K, Zbyn S, **Strasser B**, Robinson S, Minarikova L, Gruber S, Farr A, Singer C, Helbich TH, Trattnig S, Bogner W. Quantitative Sodium MR Imaging at 7 T: Initial Results and Comparison with Diffusion-weighted Imaging in Patients with Breast Tumors. Radiology. 2016; 280(1):39-48.

Strasser B, Považan M, Hangel G, Hingerl L, Chmelik M, Gruber S, Trattnig S, Bogner W. (2 + 1)D-CAIPIRINHA accelerated MR spectroscopic imaging of the brain at 7T. Magnetic resonance in medicine. 2016; [EPub].

Hnilicová P, Považan M, **Strasser B**, Andronesi OC, Gajdošík M, Dydak U, Ukropec J, Dobrota D, Trattnig S, Bogner W. Spatial variability and reproducibility of GABA-edited MEGA-LASER 3D-MRSI in the brain at 3 T. NMR in biomedicine. 2016; 29(11):1656-1665.

Hangel G, **Strasser B**, Považan M, Heckova E, Hingerl L, Boubela R, Gruber S, Trattnig S, Bogner W. Ultra-high resolution brain metabolite mapping at 7 T by short-TR Hadamard-encoded FID-MRSI. NeuroImage. 2016; [EPub].

Trattnig S, Springer E, Bogner W, Hangel G, **Strasser B**, Dymerska B, Cardoso PL, Robinson SD. Key clinical benefits of neuroimaging at 7T. NeuroImage. 2016; [EPub].

Conference Contributions

First Author

Strasser B, Chmelik M, Trattnig S, Gruber S, Bogner W. Prior knowledge in CSI obtained from phase images: initial results. International Workshop “Magnetic Resonance Studies”, 2011, Třešť, Oral Talk.

Strasser B, Chmelik M, Trattnig S, Gruber S, Bogner W. Improved quantification of CSI data by phase prior knowledge: Application to Multichannel coils. International Workshop "Methods in Proton MR Spectroscopy – Data Acquisition and Evaluation”, 2011, Tübingen, Oral Talk.

Strasser B, Chmelik M, Trattnig S, Gruber S, Bogner W. Prior Knowledge in CSI Obtained from Phase Images: Initial Results. ESMRMB, Leipzig, E-Poster.

Strasser B, Chmelik M, Trattnig S, Gruber S, Bogner W. Coil Combination of CSI Data Based on Reference Images at 7T. ISMRM 2012, Melbourne, Traditional Poster.

Strasser B, Chmelik M, Trattnig S, Gruber S, Bogner W. Increasing the SNR in MRSI by Combining the Channels of an Array Coil Using GRE Images for Phasing. International Workshop "Magnetic Resonance Studies" 2012, Oberschwarzenberg, Oral Talk.

Strasser B, Hangel G, Gruber S, Trattnig S, Bogner W. 2D-GRAPPA Accelerated FID Based MRSI of the Brain at 7T. ISMRM 2013,Salt Lake City, Traditional Poster.

Strasser B, Hangel G, Gruber S, Trattnig S, Bogner W. 2D-GRAPPA accelerated FID based MRSI of the brain at 7T. International Workshop "Magnetic Resonance Studies" 2013, Freudenstadt, Oral Talk.

Strasser B, Hangel G, Chmelik M, Trattnig S, Gruber S, Povazan M, Bogner W . (2+1)D-CAIPIRINHA Accelerated FID Based MRSI of the Brain at 7T. ISMRM 2014, Milan, Oral Talk.

Strasser B, Bogner W, Bär P, Hangel G, Springer E, Mlynarik V, Griswold M A, Ma D, Jiang Y, Nittka M. Comparison of accuracy and reproducibility of MR Fingerprinting with conventional T1 and T2 mapping. ISMRM 2015, Toronto, E-Poster.

Strasser B, Hangel G , Gruber S, Chmelík M, Dal-Bianco A, Považan M, Leutmezer F, Trattnig S, Bogner W. Ultra-high Resolution MRSI of Multiple Sclerosis at 7T. ISMRM 2016, Toronto, E-Poster, Award for best abstract in the MRS study group session.

Co-author

Hangel G, **Strasser B**, Povazan M, Gruber S, Chmelik M, Trattnig S, Bogner W. Spiral Chemical Shift Imaging at 7 T. International Workshop “Magnetic Resonance Studies”, 2013, Freudenstadt, Oral Talk.

Hangel G, **Strasser B**, Gruber S, Chmelik M, Trattnig S, Bogner W. 3D Metabolic Mapping of the Brain at 7T by Pulse-Cascaced Hadamard Encoding with Short Acquisition Delay. ISMRM 2014, Salt Lake City, Traditional Poster.

Hangel G, **Strasser B**, Gruber S, Chmelik M, Trattnig S, Bogner W. Pulse cascaded Hadamard Spectroscopic Imaging with short acquisition delay in the brain at 7T. ESMRMB 2014, Lisbon, Oral Talk.

Hangel G, **Strasser B**, Povazan M, Gruber S, Chmelik M, Trattnig S, Bogner W. 3D metabolic mapping in the brain by 2D-GRAPPA accelerated FID-CSI at 7T. ISMRM 2014, Milan, E-Poster.

Bogner W, Gagoski B, Hess AT, **Strasser B**, Bhat H, Tisdall D, van der Kouwe AJW, Trattnig S, Rosen B, Andronesi OC. Real-time motion and B0-corrected 3D-MRSI with selective reacquisition for MEGA editing of GABA in the brain at 3T. ISMRM 2014, Milan, Power Poster.

Považan M, **Strasser B**, Hangel G, Gruber S, Trattnig S, Bogner W. Multimodal Post-processing software for MRSI data evaluation. ISMRM 2015, Toronto, Traditional Poster.

Hangel G, **Strasser B**, Považan M, Gruber S, Chmelík M, Trattnig S, Bogner W. Lipid and macromolecule suppression by double inversion recovery in metabolic mapping of the brain at 7T. ISMRM 2015, Toronto, Traditional Poster.

Bogner W, **Strasser B**, Považan M, Hangel G, Gagoski B, Gruber S, Rosen B, Trattnig S, Andronesi O C. 3D mapping of Glutathione in the human brain via real-time motion corrected MEGA-LASER MRSI. ISMRM 2015, Toronto, Oral Talk.

Považan M, Hangel G, **Strasser B**, Chmelík M, Gruber S, Trattnig S, Bogner W. Detection of brain macromolecules using double inversion recovery ultra-short acquisition delay 1H MRSI at 7 Tesla. ISMRM 2015, Toronto, Oral Talk.

Hangel G, **Strasser B**, Považan M, Gruber S, Chmelík M, Widhalm G, Knosp E, Dal-Bianco A, Leutmezer F, Trattnig S, Bogner W. High resolution spectroscopic imaging with ultra short TE in patients with multiple sclerosis and brain tumors at 7T. ISMRM 2015, Toronto, Power Poster.

Považan M, Hangel G, **Strasser B**, Heckova E, Hingerl L, Gruber S, Trattnig S, Bogner W. Parameterization of measured macromolecular background in ultra-short acquisition delay 1H MRSI in the brain at 7T. ISMRM 2016, Singapore, Oral Talk.

Hangel G, **Strasser B**, Považan M, Lukas Hingerl, Chmelík M, Gruber S, Trattnig S, Bogner W. Metabolic mapping of the brain using ultra-high resolution MRSI at 7 T. ISMRM 2016, Singapore, Oral Talk

Hangel G, **Strasser B**, Považan M, Gajdošík M, Gruber S, Chmelík M, Trattnig S, Bogner W. A comparison of lipid suppression by double inversion recovery, L1- and L2-regularisation for high resolution MRSI in the brain at 7 T. ISMRM 2016, Singapore, Traditional Poster.

Hnilicová P, Považan M, **Strasser B**, Andronesi O C, Dobrota D, Trattnig S, Bogner W. Measurement reproducibility of the spiral encoding GABA-edited MEGA-LASER 3D-MRSI in the brain at 3T. ISMRM 2016, Singapore, Traditional Poster.

Heckova E, Gruber S, **Strasser B**, Považan M, Hangel G, Trattnig S, Bogner W. Comparison of high-resolution FID-MRSI in the brain between 3 and 7 Tesla. ISMRM 2016, Singapore, Traditional Poster.

Považan M, Hingerl L, **Strasser B**, Hangel G, Heckova E, Gruber S, Trattnig S, Bogner W. Improved semi-LASER sequence with short echo time for ultra-high field using selective GOIA refocusing pulses. ISMRM 2016, Singapore, Traditional Poster.

Hingerl L, Gajdošík M, Považan M, **Strasser B**, Hangel G, Krššák M, Trattnig S, Bogner W. In Vivo Detection of Omega-3 Fatty Acids at 7 T with MEGA-sLASER. ISMRM 2016, Singapore, Traditional Poster.